A Hybrid Molecular Dynamics Simulation/Pore Network Model of Diffusion in Nanoporous Carbons

Qiong Cai

Institute for Materials and Processes
School of Engineering and Electronics

Thesis submitted for the degree of Doctor of Philosophy

The University of Edinburgh

March 2007

Abstract

Nanoporous carbons are widely used throughout industry and beyond. Understanding the porous structure and its relationship to the performance of nanoporous carbons is a scientifically and technologically important problem as this will allow us to better design these materials and increase the range of their application. Designing nanoporous carbons involves relating their structure to the two processes that are important in their applications – adsorption and diffusion. The aim of this work is to develop a validated model for predicting the effective diffusion coefficient in nanoporous carbons and providing a way for the design of materials in which diffusion is important.

In this thesis, such a model is built based on the combination of molecular dynamics (MD) simulation and the pore network model (PNM) of nanoporous carbons, the so called hybrid MD/PNM. The PNM takes both the geometrical (a distribution of pore sizes) and topological (the connectivity) characteristics of nanoporous carbons, which are obtained based on physical adsorption. The effective diffusion coefficient is calculated by taking the transport diffusion coefficients in single slit-shaped model pores from MD simulation and computing the effective value over the PNM. Factors that influence the effective diffusivity have been investigated. It has been shown that a solid with a high porosity, a narrow PSD which has most of the pores carrying high transport diffusion coefficients, and a high mean coordination number which indicates a well connected pore network, is desirable for obtaining a high effective diffusivity. Moreover, and most importantly, the reliability of the hybrid MD/PNM is evaluated. This is done by replacing the real carbons in the lab with the computer-generated, and highly realistic, virtual porous carbons (VPC) with which the structure of the carbons and the effective diffusivity in the carbons can be exactly known. The good agreement between the diffusion coefficients for the PNM and the VPC indicates the reliability of the hybrid MD/PNM method and it can be used in industry for materials design.

Declaration

The work presented in this thesis was carried out in the School of Engineering and Electronics, The University of Edinburgh. It is the original work of the author except where acknowledged in the text. This thesis was composed by the author and was not submitted in any form at another university.

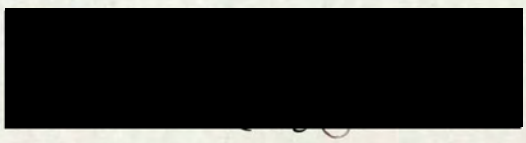

March 2007

Acknowledgements

"Trust in the Lord with all your heart and learn not on your own understanding; in all your ways acknowledge him and he will make your paths straight." Proverbs 3:5, 6

Firstly, I sincerely thank my principal supervisor, Nigel Seaton, for all his excellent advice, and for his consistent encouragement, support and generous help in not only my study, but also other aspects of my life, throughout the three years. His commitment to research based on solid fundamental principles has led my way in scientific research.

My thanks also go to my co-supervisor, Mark Biggs. His dedication and enthusiasm to scientific research, his brilliant idea and his encouragement have helped me a lot.

I owe a lot of thanks to Alex Buts for having been working hard to provide me with correct data on virtual porous carbons, for having been patient to my unexpected disturbances, and for all the helpful discussions through the three-year collaboration.

I also want to thank all my friends near and far who have shown their understanding and support, and all the friends past and present in Institute for Materials and Processes for their friendship and the happy moments we shared together. In particular, I want to thank people in the adsorption group for all the kind help and encouragement that enabled me to walk through the difficulties: Alex Vieira-Linhares, Christian Schumacher, Maria V. Navarro, Tina Düren, Claudia Prosenjak, Lev Sarkisov, Carlos Ferreiro, Jose Costa, Gaetano Festa and Patricia Lozano-Casal.

I am extremely grateful to the Universities UK for giving me an Oversea Research Scholarship, the Engineering and Physical Science Research Council (EPSRC) for the financial support. These supports have made my study at Edinburgh possible.

Finally, I want to express my deep thanks to my parents, who have always been there to support me and care about me, wherever I am and whatever I do.

Dissemination

This work has been presented in several conferences and meetings, and has been written in papers that have been published and are in the process of being published, given as follows.

Publications

Q. Cai, A. Buts, N. A. Seaton and M. J. Biggs, "Pore network modelling of diffusion in nanoporous carbons: validation by molecular dynamics simulation", *paper in preparation.*

Q. Cai, N. A. Seaton, M. J. Biggs, "Effects of surface models on self-diffusion and transport diffusion in nanoporous carbons", submitted to *Physical Chemistry Chemical Physics.*

Q. Cai, A. Buts, N. A. Seaton, M. J. Biggs, "Evaluation of the characterization methods for determining the pore size distribution and the pore-network connectivity of nanoporous carbons", *Langmuir*, in press.

Q. Cai, A. Buts, N. A. Seaton, M. J. Biggs, "Characterization of the porosity of a microporous model carbon", in *Characterization of Porous Solids VII (Studies in Surface Science and Catalysis)*, Editors : P. L. Llewellyn, F. Rodriquez-Reinoso, L. Rouquerol and N. Seaton, volume **160**, page 257-264 (2005).

M. J. Biggs, A. Buts, Q. Cai and N. A. Seaton, "Absolute assessment of adsorption-based microporous solid characterisation methods", in *Characterization of Porous Solids VII (Studies in Surface Science and Catalysis)*, Editors : P. L. Llewellyn, F. Rodriquez-Reinoso, L. Rouquerol and N. Seaton, volume **160**, page 79-86 (2005).

Presentations

Q. Cai, A. Buts, N. A. Seaton, M. J. Biggs, "A hybrid molecular simulation/pore-network model for diffusion in nanoporous carbons", *Invited talk in the Institute for Materials and Processes*, **2007**, The University of Edinburgh, UK.

Q. Cai, M. J. Biggs, A. Buts, N. A. Seaton, "A hybrid molecular simulation/pore-network model for diffusion in carbons", *The International Conference on Carbon*, **2006**, Aberdeen, UK. (Oral Presentation)

Q. Cai, A. Buts, N. A. Seaton, M. J. Biggs, "Molecular simulation of gas transport in nanoporous carbons", *Diffusion Fundamentals I*, **2005**, Leipzig, Germany. (Poster)

Q. Cai, A. Buts, N. A. Seaton, M. J. Biggs, "Characterization of the porosity of a microporous model carbon", 7th International Symposium on the Characterization of Porous Solids, **2005,** Aix-en-Provence, France. (Poster)

Q. Cai, A. Buts, N. A. Seaton, M. J. Biggs, "Molecular simulation of gas adsorption and transport in nanoporous carbons", *Collaborative Computational Project 5 Annual Conference*, **2005**, Keele, UK. (Poster)

Table of Contents

1. Introduction and Background

1.1 Nanoporous Carbons

Nanoporous carbons are a class of carbon materials characterized by a polydisperse porous structure consisting of pores of different shapes and sizes (which are defined as those in the range of micro- and meso-pore according to IUPAC[1], or more formally, "nanopore", ranging from 0.1 nm to 100 nm, according to a new classification proposed by Mays[2]). They have a microcrystalline structure. But this microcrystalline structure differs from that of graphite with respect to interlayer spacing, which is 0.335 nm in the case of graphite and ranges between 0.34 and 0.35 nm in nanoporous carbons. The orientation of the stacks of aromatic sheets is also different, being less ordered in nanoporous carbons. The structure of nanoporous carbons is related to their production process. Nanoporous carbons are produced commercially from a wide variety of carbon-based raw materials including coal, wood, peat, fruit stones, coconut shell, lignite, and certain petroleum byproducts such as pitch.[3] These raw materials are converted to porous carbon through a two-stage process: the *carbonization* of the carbonaceous raw materials in an inert atmosphere and the *activation* of the carbonized product.[4] During the carbonization process, most of the non-carbon elements such as oxygen, hydrogen, and nitrogen are eliminated as volatile gaseous species by the pyrolytic decomposition of the starting material, leaving a preliminary framework of mostly carbon. The residual elementary carbon atoms group themselves into stacks of flat, aromatic sheets cross-linked in a random manner. These aromatic sheets are irregularly arranged, which leaves free interstices that give rise to pores. During carbonization these pores are filled with the tarry matter or at least blocked partially by disorganized carbon atoms. This pore structure is further developed and enhanced during the activation process, whereby the tarry matter and disorganized carbon atoms are burned away through pyrolisis in a strongly oxidizing environment. (The oxidizing agents are normally air, CO_2, steam, O_2 and supercritical water.[5]) The activation process additionally widens existing pores by pyrolizing existing aromatic carbon - in effect burning away smaller carbon sheets and creating holes and defects in larger sheets. Finally, the raw material is converted into a form that contains a large number of randomly distributed pores of

various sizes and shapes, giving rise to an extremely high internal surface area which in some cases may be as high as 2500 m^2/g.

Due to their highly developed porosity, their relative inertness, and also the fact that carbonaceous materials are relatively cheap to produce, nanoporous carbons have received widespread interest and applicability. They are widely used throughout industry and beyond. Just a few example applications include gas separation, water treatment, catalysis, membrane reactors, rechargeable battery anodes, hydrogen and methane storage, controlled drug delivery and chemical defence.[3, 4]

1.2 Design of Nanoporous Carbons

Understanding the porous structure and its relationship to the performance of nanoporous carbon materials is a scientifically and technologically important problem as this will allow us to better design these materials and increase the range of their application. It has been recognized that both the geometrical (the pore shape and the pore size distribution) and topological (the way in which the pores are connected together) characteristics of the porous structure play important roles in the applications of nanoporous carbons.

When designing nanoporous carbons or processes and technologies for their applications it is important to have a handle on two key aspects of the carbons – the equilibrium properties of the guest species within them (typically adsorption isotherms and heats of adsorption) and their transport properties in the form of diffusion coefficients. Whilst experimental determination of equilibrium properties, especially the adsorption isotherms, is relatively routine, the measurement of transport properties is far more difficult for a variety of reasons.[6] Given that measurement of transport properties is very important (for example, the design of modern industrial catalysts with intermediate pore size requires that the diffusion coefficient of the reacting species within the pores of the catalyst support be accurately known), it is highly desired to have reliable measuring tools for the diffusivity within nanoporous carbons. If the diffusion coefficients in the materials

are known, they can be related to the structure of the material (as mentioned before, both geometrical and topological characteristics of the porous structure), whereby the relationship between the structure of the material and its performance can be established. With this information we can come to the design of the materials.

1.2.1 Design from the experimental side

Diffusion coefficients through porous carbons can be measured using experimental techniques. There are actually several experimental techniques to measure self- and transport diffusivities of the fluid confined in porous materials. For example, the transport diffusion coefficient D_t can be measured using macroscopic methods such as the chromatography method,[7] the frequency response (FR) method,[8] the differential adsorption bed (DAB) method,[9] the constant molar flow (CMF) method,[10] the gravimetric uptake method,[11] and the single-crystal membrane (SCM) technique.[12] The self-diffusion coefficient D_s can be obtained using the microscopic methods including the pulsed-field-gradient nuclear magnetic resonance (PFG-NMR) method[13, 14] and the quasi elastic neutron scattering (QENS) method.[14, 15] The transport diffusivities can also be determined by using the coherent QENS method to measure the collective motion of the confined molecules in porous materials at equilibrium.[16] Note that the diffusion coefficients governing self-diffusion and transport in porous materials are fundamentally different quantities.[17] Self-diffusion of the confined fluid is the measurement of the net motion of tagged particles in an equilibrium system. Transport, however, arises in the presence of a chemical potential gradient. It is the transport diffusivity that is of greatest interest in physical applications involving net mass transfer, such as storage of methane (the main component of natural gas) into nanoporous carbons.[18] In this work we are especially interested in transport diffusion.

Each of these methods has advantages and disadvantages or limitations. One of the limitations, for example, is that the response time of measurement devices restricts the fastest diffusivity that can be measured; most macroscopic techniques are limited to diffusivities below 10^{-5} – 10^{-7} cm^2/s, while the microscopic techniques can only measure diffusivities above 10^{-5} – 10^{-7} cm^2/s. Moreover, in contrast to adsorption

equilibrium data, diffusivities reported in the literature exhibit vast differences, reaching several orders of magnitude for some systems, as shown in Table 1.1. Although discrepancies between experimental diffusivity values obtained by different techniques can sometimes be explained for some systems, vast unexplained differences exist for many systems. And the lack of systematic data (For example, only a few data can be found of experimental measurement of diffusion coefficient of methane in carbons.) hinders the development of plausible explanations for the differences in the diffusivity values reported in the literature.

Table 1.1 Diffusivity data reported in the literature for methane

Materials	Temperature (K)	Method	Diffusion coefficient (m^2/s)	Reference
Silicalite	250	QENS	5.0×10^{-9}	Jobic *et al.*[15]
Silicaite	323	SCM	8.9×10^{-10}	Sun *et al.*[12]
Silicalite	323	SCM	4.1×10^{-9}	Talu *et al.*[6]
Sydney Basin coals	298	Gravimetric	$(1.23\text{-}4.88)\times10^{-10}$	Saghafi *et al.*[19]
Meso-Carbon Microbeads	298	Gravimetric	1.0×10^{-13}	Wang *et al.*[20]

The fact that the experimental measurements can not give consistent data prevents materials design. Moreover, as experimental measurement is based on real materials, it can not be used to investigate hypothetical changes in material properties, and so it can not be used for design. It is why a predictive modelling method is needed.

1.2.2 Design from the modelling side

An alternative to measuring diffusion coefficients in porous materials is to use a *predictive* model. The use of the predictive model to obtain diffusion coefficients solves the problem of inconsistent data using the experimental techniques. Most importantly, the predictive model can be used to investigate hypothetical changes in material properties, and so can provide useful information for materials design. There are several different approaches using models to predict diffusion coefficients in porous materials.

Approaches at the single-pore level

The first approach is to use analytical models that describe the possible transport mechanisms at the single-pore level. There is considerable theoretical work devoted to giving analytical models for various transport mechanisms within porous materials, including Knudsen diffusion, surface diffusion, viscous flow, and the systematic approach of Stefan-Maxwell in solving multi-component problems.[21] However, these analytical models always describe limiting cases which usually do not correspond to a real physical situation. Researchers have shown that transport in one single pore can be the combination of Knudsen diffusion, surface diffusion and even viscous flow.[11, 22, 23]

Instead of analytical models, molecular simulations provide a vital tool in gaining a detailed understanding of the transport properties of the fluid confined in nanoporous materials and in making predictions for the design purpose. Molecular simulation in this work refers to computational techniques that use atomistic level description of the molecular systems to mimic the behaviour of the systems at certain conditions. The model that describes the molecular system includes representations of the solid structure and the structure of the guest molecules in addition to formulations of all pertinent interactions for solid-gas and gas-gas pairs. The main power of molecular simulations is the clearly linked cause-effect relationships that can be conveniently exploited to study systems that exist or do not exist in reality. Many studies have applied Molecular Dynamics (MD) (e.g. refs. [24], [25]) and Monte Carlo (MC)[26, 27] simulations to understand transport and separation of gases in single pores. MD simulation is a better choice as it provides an absolute measure of real time and gives the diffusion coefficients themselves, while MC simulation can only give the ratio of diffusion coefficients. A lot of studies have been contributed to understand aspects that influence diffusion of confined fluid in molecular level pores. Materials concerned include zeolites,[28-31] silicalite,[16, 32, 33] carbon nanotubes,[34-41] nanoporous carbons,[23, 24, 42-45] and metal organic framework (MOF) materials.[46] Most of the MD simulations calculated the diffusivity for a given single-pore-level model. (The details of the single-pore-level model for nanoporous carbon are given later in Section 1.3.1.) MD simulations could also be used for simulating transport through

nanoporous carbons whilst taking into account the complex structure of the solid.[47] However, such modelling in which both the pore system *geometry* and *topology* are captured is extremely time-demanding because of the computationally intensive nature of MD simulations. So it can not be used *routinely* for the purpose of materials design.

Approaches taking into more complex structural information

When we deal with transport through a porous medium, we need to describe the medium. The simplest picture of accounting for the solid structure, above the level of a single pore, is to take all structural properties into constants of proportionality, such as the tortuosity factor. A long standing approach to modelling fluid transport in porous solids thus makes use of this simple picture. Such an approach involves averaging a pore-level transport model over the pore size distribution (PSD) and then using the so-called tortuosity to account for pore system topology and other features omitted from the averaging.[48] Diffusion experiments are the predominant method for determining the tortuosity. This approach has several disadvantages. The experiments are non-trivial. As this tortuosity changes with temperature and fluid, experiments may also be required for a range of fluids and temperatures. The solid must also physically exist. This approach is actually similar to the experimental approach as discussed earlier, rather than a modelling approach. It can not be used to investigate hypothetical changes in material properties and thus prevents routine and reliable design.

A more satisfactory approach is to model more realistically the solid structure and then incorporate it into the diffusion model. Such an approach would permit routine and reliable design by allowing identification of the required characteristics of a carbon. A pore network model (PNM) provides a means of linking topological and geometrical characteristics of a porous solid with its transport behaviour. This model assumes that the pore space of a carbon can be described by a network of pores of distributed size – quantified in terms of the PSD – with an average connectivity, $\overline{Z}$, which is defined as the average number of pores meeting at a junction. There are various well established methods for determining the PSD,[49-51] whilst Seaton and co-

workers have developed methods to determine the average connectivity for micro and mesoporous solids.[52-54] Whilst PNMs allow capture of both geometry and topology with reasonable resources, they are dependent on the single-pore diffusion coefficients. In this work, we use a hybrid model, in which a PNM is coupled with MD at the single-pore level, as shown in Figure 1.1. Once the single-pore diffusion data has been determined using MD and stored in a database for future use, an effective diffusion coefficient, D_e, can be predicted for a solid given only an isotherm (*i.e.* equilibrium data) for the solid, which is used to characterize the solid. Note that the terminology "effective diffusion coefficient" is used to differentiate the diffusion coefficient through the complex solid from that in the single pores. So, the hybrid MD/PNM would allow the modelling of transport in carbons on the basis of characterisation experiments only.

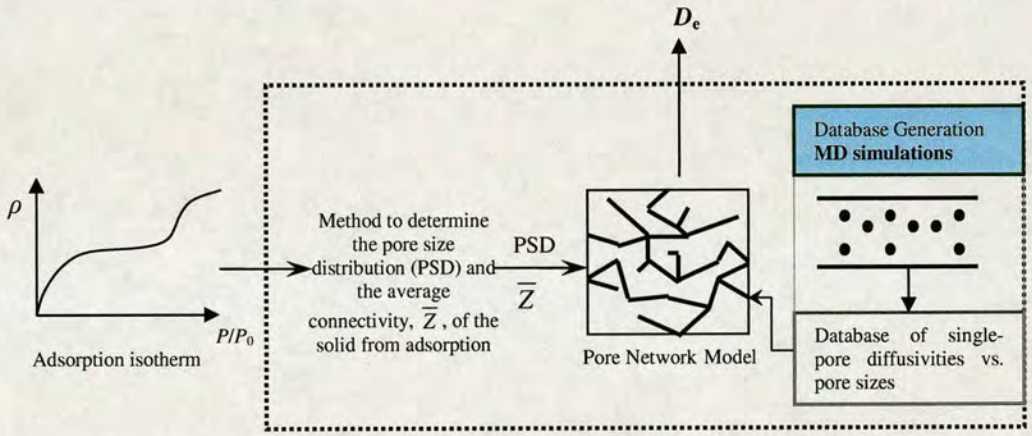

Figure 1.1 Hybrid MD/PNM for determining the effective diffusion coefficient of a solid that only requires equilibrium experimental data (e.g. an adsorption isotherm) as input.

Validation of the hybrid MD/PNM approach

Clearly, if predictions from the hybrid MD/PNM are to be correct, the pore network and single-pore models must capture the essentials of the pore structure of the solid of interest and the physics of the diffusion process. It has been shown[55] that different plausible PNMs can yield very different effective diffusion coefficients, because the PSD and the pore network connectivity that characterize the PNM have a significant influence on the effective diffusion coefficient. Other studies have also shown that omission or inappropriate treatment of features at the single-pore level can also have

a profound effect.[56] It is clear that before wide take-up of the hybrid MD/PNM occurs, it must be validated. The aim of the work is, therefore, to develop a validated hybrid MD/PNM for transport in nanoporous carbon materials.

One of two strategies may be used to validate the MD/PNM approach. The first is purely experimental – compare predicted effective diffusion coefficients with experimental values. The problem with this is the limited capacity for resolving any observed differences between the predicted and the experimental values, as it is difficult to discern what makes the values different. This is especially acute given that even experimental values for the same solid can vary widely depending on the experimental method used, as discussed in Section 1.2.1. The alternative is a model-based approach such as that illustrated in Figure 1.2, where a real porous carbon in the laboratory is replaced by a computer generated "virtual porous carbon" (VPC), and molecular simulation is used to obtain the adsorption isotherm and the effective diffusion coefficient, D_e, for the VPC. What makes this approach so attractive is the certainty we can have in the effective diffusion coefficient of the VPC, and the ability we have to directly probe the diffusion process at the molecular level, which

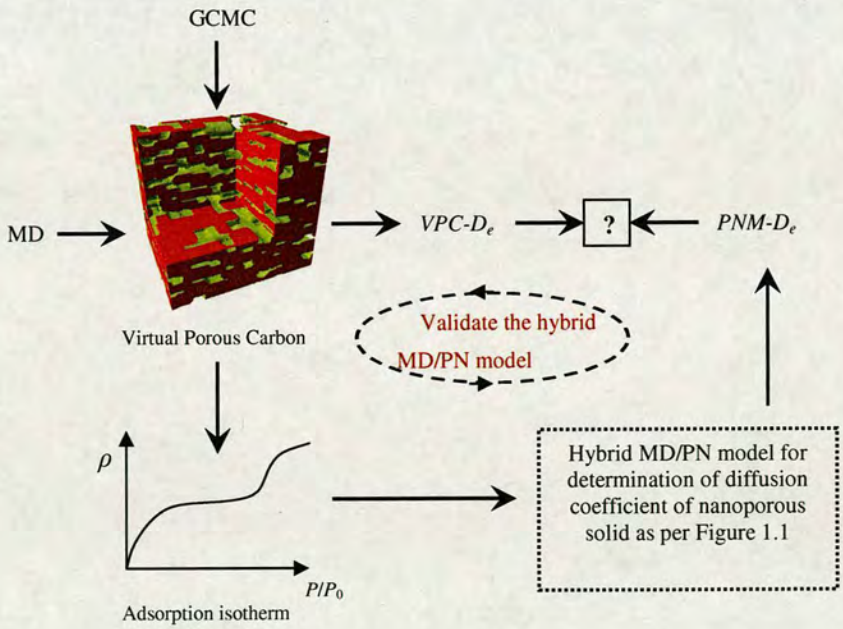

Figure 1.2 Model-based strategy for validating the hybrid MD/PN model for determining the effective diffusion coefficient of a nanoporous carbon.

should greatly aid resolving any differences between the actual diffusion coefficients and those obtained from the hybrid MD/PNM. Moreover, the certainty we have in the structure of the VPC and its effective diffusion coefficient will allow us to evaluate the reliability of the hybrid MD/PNM approach.

1.3 Models for Nanoporous Carbons

1.3.1 The slit pore model

The slit pore model has been widely used and confirmed quantitatively as an appropriate model for nanoporous carbons, since it was proposed by Emmett[57] in 1948. In its most basic form, this model is defined by two parallel semi-infinite blocks of graphite whose separation is the pore width. Figure 1.3 gives an example of the slit pore model, with methane molecules adsorbed in the pore. Note that only the first graphite layer of the semi-infinite block is shown. A nanoporous carbon is typically described in terms of a collection of such pores of varying width while ignoring the intersections of pores.

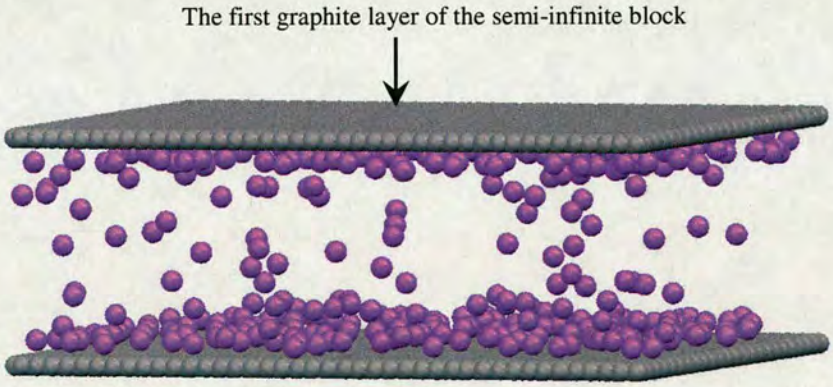

Figure 1.3 An example of the slit pore model, with methane molecules (purple particles) adsorbed in the pore.

Whilst the usefulness of the slit pore model has been recognized for predicting adsorption and determining the porous structure based on the adsorption (see, for example, refs.[58, 59] for recent reviews), its limitations are also widely recognised. For example, experimental evidence suggests that the walls of carbon micropores are just a few graphene layers thick,[60, 61] such pore walls have been shown to yield different adsorption behaviour compared to pores with infinitely thick walls.[61, 62] Experimental

evidence also suggests that the length and breadth of the pores are of the same order as the pore width, leading to significant additional accessible surface area and energetic heterogeneity from graphene edge sites.[63, 64] These sites additionally play an important role in diffusion processes,[65, 66] as does pore system topology (*i.e.* pore connectivity, loops and dead-end pores).[67] Nooks and crannies arising from surface defects can trap molecules;[68] moreover, heteroatoms such as nitrogen, sulphur and oxygen are all likely to cause disruption of pore surfaces[69] and are active sites for polar molecules such as water.[70-72] These are the source of experimentally observed irreversible adsorption.[69] Finally, Harris *et al.*[73] have observed under high resolution electron microscopy (HREM) that certain porous carbons may contain significant levels of five- and seven membered rings and, therefore, take on a fullerene-like structure; the existence of such rings and, therefore, local curvature certainly seems feasible, given the ease with which some fullerenes and other curved carbonaceous structures can be formed.

However, the shortcomings of the slit pore model do not undermine its usefulness. The slit pore model is here to stay because of its relative simplicity, comparatively low computational cost, and its indispensable role in the characterisation of carbons where substantially more complex models are unlikely to play a significant part for the foreseeable future. It is for this reason that many workers have endeavoured to address the shortcomings of the model whilst still retaining the same basic framework. Some have recently incorporated pore wall thickness distributions within the context of pore size distribution determination.[61] Several workers have included chemical heterogeneity by adding active sites of various types to the pore surfaces.[70-72] Others have used nonrectangular cross-sections.[74] Single pore junctions formed by the intersection of slit pores have been used to investigate what effect these may have on adsorption and transport behaviour.[75, 76] Etched pore surfaces also have been investigated.[76, 77] In this work, we continue using the basic slit pore model to characterize nanoporous carbons.

1.3.2 The pore network model

In order to develop a predictive theory for calculating the effective transport in disordered porous media, one has to have a realistic model of the disordered medium. Clearly, the slit pore model ignores the pore system topology of nanoporous carbons, whilst the topology of a solid has been seen playing an important role in determining the transport properties.[55] Seaton and co-workers[76] have attempted to include the effect of pore system topology by combining the slit pore model with networks, the so called the pore network model (PNM). The PNM is used to represent the pore space of nanoporous carbons, as shown in Figure 1.4, in which each individual pore is a slit model pore and the pores are distributed and connected in some way. (The place where the pores are connected is termed the junction.) The connectivity of the PNM is usually quantified as the mean coordination number, i.e. the average number of pores at each junction over the whole network. The PNM is a topologically-disordered network that represents a considerable simplification of the structure of real carbons.

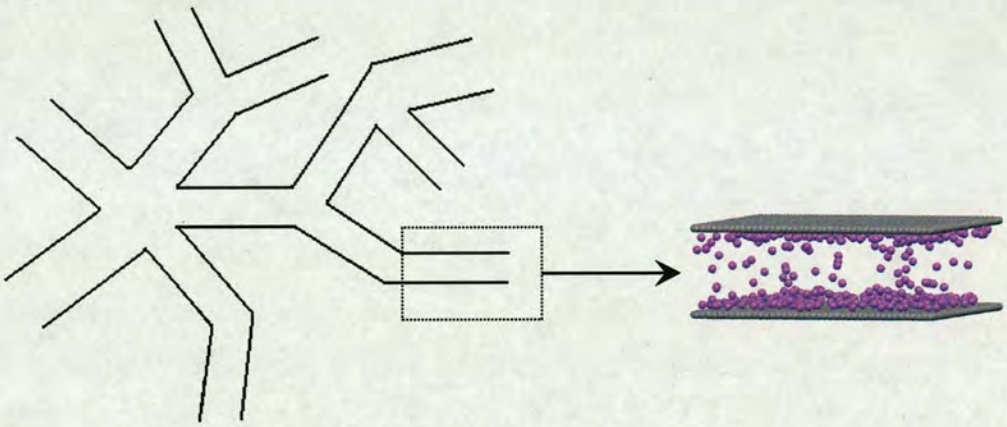

Figure 1.4 An illustration of the pore network model.

For studying the properties of porous media, it is very helpful to map the porous structure of a porous medium to a regular network (e.g. cubic lattice), whereby the well established methods and theories based on the regular network can be applied. In principle, any porous medium can be mapped onto an equivalent network of bonds and nodes, where the pore bodies are represented by network bonds and the pore junctions are represented by network nodes. The geometric characteristics of the medium can be incorporated into the structure of the network by assigning random

pore widths and lengths to the network bonds. (Each bond in this case is a slit pore.) These are selected from pore size distributions that can, in principle, be obtained from adsorption-based characterization of the solid, which will be discussed in Section 1.5. The details of such a mapping are given by Lin and Cohen.[78] Usually, the resulting equivalent network has a random topology, i.e. its coordination number Z, which is the number of bonds (pores) connected to the same site, is a stochastic variable. Some of the bonds in the network can be absent so that the mean coordination number of the network may be reduced from the original value of the original regular network. In the real solid, the junctions would be distributed stochastically in space, whereas, in the model they are fixed at lattice sites. Although it would be desirable to place the junctions stochastically within the pore network model, this would pose two difficulties. Firstly, networks with stochastically distributed nodes are less tractable than regular networks. Secondly, the distribution of junctions in space might introduce the wrong type of randomness. Fortunately, it is known that, as long as the average coordination number of the topologically-disordered network is equal to the coordination number of a regular network, the effective properties of the two systems are, for all practical purposes, identical.[79] And the transport properties of pore networks are strongly dependent on the mean coordination number of the network and the distribution of single-pore diffusion coefficients, but relatively insensitive to other respects of the morphology of the network.[79-81] Therefore, a regular network for this study may be employed which, in the present work, is a simple-cubic network in 3 dimensions. Such a mapping will be discussed again in Chapter 3.

1.3.3 Virtual porous carbons

The pore network model, though capturing both the geometry and topology of nanoporous carbons, is still a simplified model. More complex models, termed virtual porous carbons (VPC) here, have been constructed using the so-called *reconstruction* methods, to build structures that match experimental characteristics of existing carbons. The first model that could be reasonably termed a VPC was that of Biggs and Agarwal,[82] which was motivated by insights arising from transmission electron microscopy (TEM) studies.[83] These studies suggest that carbons are

hierarchical in nature, where polyaromatic molecules combine to form *basic structural units* (BSUs) that in turn aggregate to form regions of local molecular orientation (LMO) which finally assemble to create the mesoporous structure typical of nanoporous carbons.[3] The dimensions of the BSUs and regions of LMO, the average inter-layer distance within the BSUs and the mis-orientation of the BSUs with the regions of LMO can all be determined experimentally. Another early VPC model was that of Segarra and Glandt,[84] which was once again motivated by insights from TEM studies. The basic building element for this model is a circular platelet consisting of a finite number of circular graphene layers with polar edges. These platelets are akin to the BSU while the atomic detail of the platelets was smeared out. Foley and co-workers[85] constructed through a stochastic process candidate structures with a specific number of carbon and hydrogen atoms by joining together fragments drawn from a library of polyaromatic molecules. The candidate structures yielded often contained unsaturated carbon atoms. Bonds between unsaturated atom pairs from different fragments were, therefore, systematically formed – it is through this process that five and seven membered rings were formed, and hence local curvature in the structure was brought about. The approach of Foley and co-workers was not able to produce any model when the H/C ratio fell below ~20%, which are typical of many nanoporous carbons. Gubbins *et al.*[86, 87] used Reverse Monte Carlo (RMC) simulation to reconstruct the carbon structure by fitting the radial distribution function of the carbon atoms determined by experiment. A solid of the required density is built by randomly placing polyaromatic plates of variable shape and distributed size into the volume, roughly aligned in the same direction but with random tilts about their in-plane axes. Each polyaromatic plate is formed from an initial hexagonal ring by adding/deleting hexagonal rings to/from the edge so as to achieve the target solid density and plate size distribution. The major problem associated with building models by forcing them to match specific experimental data is their lack of uniqueness – there are potentially many models that will satisfy the experimental data.[88] Zetterström *et al.*[89] have used Raman spectra data to establish a better starting structure for the RMC process compared to the completely random structures used by others.

The VPC can be used in a variety of very useful ways that inform fundamental understanding and potentially advance practice, although it is difficult to tune the properties of the VPC so that they match those of a particular real carbon. In this work, we take the VPC as the real carbon, as a tool to validate the PNM-based approach. This will be discussed more in later sections. The VPCs are constructed using the algorithm of Biggs *et al.*,[47, 90, 91] which builds carbons from small polyaromatic elements to match a desired porosity. Their work has shown that these VPCs yield adsorption behaviour seen experimentally. As Figure 1.5 shows, the pore space of the VPCs is typically complex with a wide variety of pore shapes (roughly parallel slit pores, more tapered slit pores and mesoscale cavities), sizes (length and breadth, as well as width) and surface textures (basal, armchair, surface irregularity over longer lengthscales). The VPCs are related in that their mean pore sizes are similar. They primarily differ in the width of their PSD, porosity and connectivity.

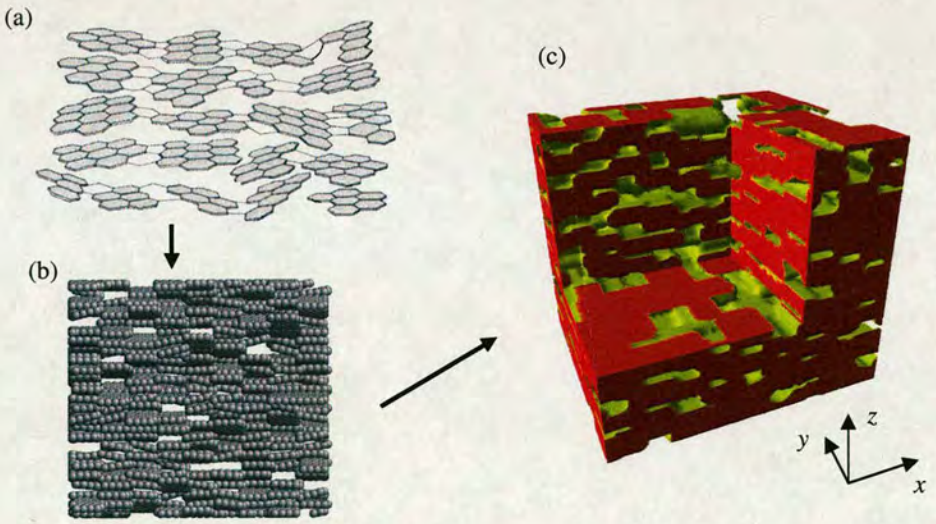

Figure 1.3 Schematic show of (a) small polyaromatic elements that build up nanoporous carbons, (b) side view of one of the VPCs considered – note the tilting of the polyaromatic crystallites, which lead to complex pore shapes and surface textures, where the white areas indicate pore space that can be looked through from the side view, the small grey spheres indicate carbon atoms, and the darker areas indicate the space that is blocked so that can not be looked through from the side view, and (c) potential energy iso-surface of the VPC with a corner cut out showing the solid (red) and the porosity (yellow). The dimensions of the VPC shown here are 88.42 Å, 76.57 Å, and 80.50 Å respectively in the *x*, *y* and *z* directions.

1.4 Determination of the PSD and the Pore Network Connectivity

As discussed earlier, the PNM is used to represent the structure of nanoporous carbons. The geometrical (i.e. the PSD) and the topological (i.e. the pore network connectivity) characteristics of nanoporous carbons are used to construct the PNM. Despite its simple account of the geometry and topology of porous materials, the PNM has been used successfully to characterize carbon adsorbents. Determination of the PSD and the pore network connectivity is based on physical adsorption which is widely used for characterizing porous materials because of its simplicity and reliability.

1.4.1 Determination of the PSD

Several methods [49-51, 92-96] based on physical adsorption have been used to determine the PSD of nanoporous carbons, by relating adsorption in model slit pores to the experimental measurements of adsorption on the real carbons. Each method embodies a degree of uncertainty, and conclusive evidence of the accuracy of the resulting PSD is often not available.[97-99] Nevertheless, from a fundamental point of view, the statistical-mechanical methods (including density functional theory[49, 50] and Monte Carlo simulation[51]), now widely used, should be more realistic than classical approaches because these methods are based on a molecular description of adsorption. In addition, they can describe both subcritical and supercritical adsorption, and so can reliably determine the PSD throughout the micro- and mesopore size range. In the statistical-mechanical methods, the pore size distribution, $f(w)$, is obtained by solving the adsorption integral equation:

$$N(T,P) = \int_0^\infty \rho(w,T,P) f(w) dw \tag{1.1}$$

where $N(T,P)$ is the experimentally determined adsorption at temperature, T, and bulk pressure, P, and $\rho(w,T,P)$ is the adsorption of the same fluid in a single, model pore of width w (the "single-pore isotherm").

Seaton *et al.*[49] first used local density functional theory (L-DFT) to obtain the PSD from nitrogen adsorption in slit model pores. Lastoskie *et al.*[50] later improved this method to use non-local density functional theory (NL-DFT) to interpret the PSDs from the adsorption of nitrogen and methane. However, both L-DFT and NL-DFT methods are based on a mean-field approximation of fluid-fluid attractions, which become inaccurate for fluids confined within very small pores. [100, 101] Gusev *et al.*[51, 102] were the first to derive the PSDs of nanoporous carbons with Monte Carlo simulation. They simulated methane adsorption in slit-shaped pores using Grand Canonical Monte Carlo (GCMC) simulation, and extracted a PSD for the carbon by analyzing experimental methane adsorption at 308 K. This PSD was then used to predict methane and ethane adsorption on the same adsorbent at higher temperatures. The predicted isotherms showed excellent agreement with experiment.[102] Seaton and co-workers[103, 104] further developed and validated this method. They also extended this method to determine PSDs from methane and ethane binary adsorption and further predict this binary adsorption behavior with the PSDs obtained. Recently, Ravikovitch *et al.*[105] demonstrated the consistency of the density functional theory and Monte Carlo simulation based methods for characterization of carbons. They observed good agreement between NL-DFT and GCMC based pore size distributions from different gases (N_2 and Ar at 77 K, and CO_2 at 273 K). However, Sweatman and Quirke[106, 107] showed that the use of GCMC simulation method, instead of density functional theory, to generate databases of adsorption isotherms in model slit pores, led to more reliable pore size distributions for N_2 at 77 K and CO_2 at 298 K. Because of its consistency and the advantage of allowing realistic, atomistic descriptions of the adsorbent and the adsorptive, the GCMC simulation method has become widely used. [51, 59, 75, 102-115] Although this method is generally found to give self-consistent results, until now there has been little independent evidence that the structural information obtained is correct, i.e. the extent to which it captures the real structure of the material.

Consistency and correctness of a PSD

The *consistency* of a PSD refers to its ability to predict adsorption on the same material. For example, we obtain a PSD for a carbon based on the adsorption of some

species at some temperature; we say this PSD is consistent if it can give reasonable prediction of the adsorption of the same species at other temperatures or the adsorption of other species. In this case, the PSDs for the same carbon using different species as probes can be quite different. They are not necessarily the same as long as they show the same adsorption behaviour for the species of interest.

The *correctness* of a PSD, on the other hand, indicates that the PSD is an accurate representation of the pore structure of this material. The correctness of a PSD may be not so important in the case of adsorption, as discussed above. However, it is very important for using the PSD obtained using adsorption for other purposes: for example, the accurate prediction of the transport coefficient from the pore network depends on the correctness of the PSD. The evaluation of the correctness requires a comparison with the "true" structure. However, the complexity of the porous structure of carbons, and the difficulty of obtaining direct, independent measurements of their porous structure, makes this problematical. Recently, microscopy techniques such as high resolution transmission electron microscopy (HRTEM)[116] and scanning tunneling microscopy (STM)[111] have been used to provide "exact" independent measures for comparison. As far as we know, only Stoeckli and co-workers[111] assessed the PSD from GCMC simulation method by comparing it with the PSD determined from STM. They attained generally good agreement between the two PSDs, though there were some discrepancies. Unfortunately, HRTEM and STM micrographs are projections of complex three-dimensional structures onto a plane and therefore their interpretation is uncertain.

This work is intended to test the correctness of the PSDs from the GCMC simulation method, using the "absolute assessment methodology",[91] in which the GCMC simulation method is used to characterize the VPCs with known structure. The absolute assessment methodology works in such a way that the adsorption isotherms from the VPCs are the "experimental" input to the characterization method to be assessed (GCMC method in our case) and estimates of the PSDs of the VPCs are obtained. Comparing such estimates against the corresponding exactly known

structure will enable us to draw conclusions regarding the correctness of the method for the particular model system.

Molecular probes of the pore structure

Before we come to determine the PSD, an essential question should be answered: which adsorptive should be used to probe the pore structure? Previous studies have shown that different molecular probes give different estimates of the pore structure, mainly due to the influence of different molecular sizes and strength of interaction with the adsorbent. It is thus natural to ask: how reliable is the PSD, and how can we most effectively use different adsorptives? Nitrogen adsorption at 77 K is the current standard means for pore size determination of adsorbent materials. Carbon dioxide at ambient temperature is found to be a more accurate probe of microporosity than nitrogen at 77 K,[59, 105-107, 111, 112, 117-119], the higher temperature giving the advantage that the temperature is high enough to avoid diffusion problems, and its physical properties allow one to reach very low relative pressures without complex equipment. López-Ramón *et al.*[54] provided another approach to obtain a better PSD by combining the different ranges of pore size probed by different molecules. They obtained three different PSDs from three different gases - CH_4, CF_4 and SF_6 - and then combined the partial PSDs, to get a more complete PSD. However, they did not check how this overall PSD would perform when used to predict the adsorption for all these gases, and so its consistency was not fully investigated. In this work, we use the approach of López-Ramón *et al.*[54] Three adsorptives of increasing size – CH_4, CF_4 and SF_6 – are used at the three temperatures of 258, 275 and 296 K. The overall PSD is obtained by combining the partial information obtained using the different adsorptives. The overall PSD is then used to predict the adsorption of the three species at the three temperatures to check the consistency of the overall PSD obtained.

1.4.2 Determination of the pore network connectivity

The feature that different molecules probe different ranges of pore sizes arises because (1) the molecular size of the probe and the strength of its interaction with the adsorbent influences the adsorption strength; and (2) the real nanoporous carbons

contain pores of different sizes which are connected together in a pore network and the presence of constrictions in the pore network inhibits the passage of one or more adsorbed species. Several methods have been developed for determining the network connectivity, based on a percolation-theory interpretation of adsorption data. These approaches generally utilize the property that in randomly connected pore networks, the accessibility of the network to a probe of a certain size depends on the mean coordination number of the network, $\overline{Z}$. Seaton and co-workers[52, 53] have developed such a method to determine network connectivity for mesoporous solids. Since this method is not applicable for microporous solids, they then developed another approach to measure the pore network connectivity of these materials, based on the PSDs obtained using adsorptives of increasing size – CH_4, CF_4 and SF_6.[54] By comparing the PSD derived from the adsorption isotherm of an adsorptive with the overall PSD built from the PSDs of that and smaller adsorptives, an estimate of the connectivity of the pore network can be extracted using percolation theory. A related approach was used by Ismadji and Bhatia,[120] who investigated the connectivity of porous carbons by comparing the PSD from the adsorption of esters with the more complete PSD from the adsorption of argon, and Navarro *et al.*[121] who studied the evolution of the connectivity of a porous carbon during activation by analyzing ethane and phenanthrene adsorption against nitrogen adsorption at 77 K. Their studies demonstrated the usefulness of the percolation theory to analyze the PSDs for obtaining the pore network connectivity in terms of the mean coordination number $\overline{Z}$.

The pore network model thus can be built based on the PSD and the mean coordination number, as described in Section 1.3.2.

1.5 Single-pore Diffusivities from Molecular Dynamics Simulation

As discussed earlier, MD simulation takes a significant role in the hybrid MD/PNM approach as it gives the single-pore diffusivities whereby the effective diffusivity through the PNM can be calculated. At the pore level, a wide variety of complex factors influence the transport properties, such as the sizes and the shape of the pores,

the density of the adsorptive molecules (both single species and mixtures), the interactions between the molecules and the pore surface. Previous studies have shown that diffusion coefficients depend considerably on how the pores are constructed, and especially the assumed surface of the pore model. The slit pore model is used for studying nanoporous carbons. Unlike crystalline materials such as zeolites, silicalite and MOFs, for which the pores are necessarily constructed as atomistic, the slit pore model is often assumed to have smooth walls, for greater computational speed. This work here is intended to investigate the influence of the assumed pore wall surface on diffusion, and furthermore choose the "right" surface model for calculating single-pore diffusivities.

Three wall conditions have been considered so far, namely a smooth wall, an atomic wall and a diffuse wall. A smooth wall is composed of structureless planes with all the solid atoms smeared out; the fluid molecules interact with the planes as a whole. In contrast, an atomic wall consists of corrugated planes (at least the plane in contact with the pore fluid, if not all the planes) with the solid atoms on the planes rigidly fixed; the fluid molecules interact with the solid atoms separately. A diffuse wall reflects the fluid molecules by giving the molecules new velocities according to cosine law of diffuse scattering while simultaneously satisfying conditions corresponding to thermal equilibration with the wall. For a diffuse wall, the surface of the wall can be corrugated [122] or smooth.[123] The smooth surface, combined with diffuse scattering, is intended to represent the effect of the atomic structure on the trajectories of the molecules. When a structured wall is used with diffuse scattering, the argument is (presumably) that the diffuse scattering reflects the vibrational motion of the solid atoms.

The influence of different wall conditions on self-diffusion has been partly investigated by other workers. A number of molecular dynamics (MD) simulations used the smooth wall condition to examine self-diffusion in slit pores assuming either rare-gas walls or carbon walls.[43-45, 122-128] Schoen *et al.*[125] and Somers *et al.*[126] calculated self-diffusion coefficients in pores with atomic walls, but constructed the wall as face-centered cubic (100) planes of rigidly fixed rare-gas atoms. So far, no

work has been carried out for self-diffusion in carbon pores with atomic walls. The diffuse wall was first applied by Diestler *et al.*[122] in a rare-gas wall system and later by Cracknell *et al.*[123] in a carbon wall system to study its influence on self-diffusion. In both cases, they found that compared to the smooth wall, the diffuse wall gives smaller diffusivity. In recent papers,[23, 42] the so-called fluid-solid thermal diffuse scattering (TDS) algorithm, introduced by MacElroy and Boyle,[23] has been used to simulate the diffuse wall condition in slit carbon pores. This TDS algorithm works with rigidly-fixed corrugated walls. Whenever a molecule comes closer to a wall atom, it is reflected from a scattering plane defined at a specific position, according to the cosine law of diffuse scattering. Jakobtorweihen *et al.*[40, 129] investigated the influence of this diffuse wall on self-diffusion in carbon nanotubes. They noted that the diffuse wall gives too many diffuse collisions (thermalizations), thus leads to an underprediction of self-diffusion. Although self-diffusion has been studied in carbon smooth walls and diffuse walls, there is no work done with carbon atomic walls – the more realistic surface model for nanoporous carbons. It is thus unclear whether the atomic wall should give "better" self-diffusion coefficients compared with the smooth wall and the diffuse wall.

The above discussions are all based on self-diffusion. As discussed in Section 1.2.1, self-diffusion and transport diffusion are fundamentally different properties, and so the observation for self-diffusion should not be taken for granted for transport diffusion. Moreover, it is transport diffusion related to mass transfer that happens in real applications that we are interested in. There are several papers that studied transport of the confined fluid in slit carbon pores. The smooth wall,[25, 130, 131] the atomic wall,[131, 132] and the diffuse wall[23, 42, 123] have been used. However, most of these studies gave their attention to the separation of mixture gases in terms of permeability.[23, 25, 42, 131, 132] Only a few paid attention to the influence of different wall conditions on the transport diffusivities. Xu *et al.*[131] compared the flux of CO_2/CH_4 obtained with structured walls (corresponding to the atomic wall) and smooth walls in one pore. They found that while the flux of CO_2 with the structured wall is smaller than that with the smooth walls, the flux of CH_4 is essentially the same in both cases. This can be explained as follows. As CO_2 is the preferably

adsorbed species, CO_2 molecules stay close to the wall surface, while the CH_4 molecules mainly stay in the middle of the pore. So the flux of CO_2 is influenced by the surface of the wall, while the flux of CH_4 stays unchanged with the changed wall surfaces. This indicates that transport diffusivities are influenced by the wall conditions.

Cracknell *et al.*[123] proposed in their paper that the smooth wall and the diffuse wall may be viewed as extreme cases; the former behaves as a purely specular condition where there is no fluid-wall momentum transfer, while the latter is a purely diffuse condition where there is a complete fluid-wall momentum transfer. Sokhan *et al.*[24] and Arya *et al.*[133] have shown that both diffuse and specular reflections should be considered when fluid-solid collisions occur. Each collision involves a different incident angle and strikes the surface at a different position. Insofar as the surface is not smooth (the surface of the pore wall is indeed not smooth in reality), the incident and reflected angles are different simply because the molecule strikes the surface atom at a point with an oblique plane. This mechanism implies that each collision is never purely diffuse or specular. Instead, collisions of gas molecules with the wall are partly diffuse and partly specular, the relative magnitude of each depending on the magnitude of the tangential momentum accommodation coefficient α. Such theories, involving finding the accommodation coefficient α as a function of the roughness, can be theory dependent. We suppose that in the case of the atomic wall, where the corrugation of the wall surface is present and the details of the collision dynamics are ignored, might give partly diffuse and partly specular reflection for fluid-solid collisions. It thus gives us great interests in investigating the transport diffusivities using an atomic wall condition, in comparison with the smooth wall and the diffuse wall conditions.

We are trying to determine which models are appropriate for simulating self-diffusion and transport diffusion in carbons, by systematically studying the influence of the smooth wall, the atomic wall and the diffuse wall on self-diffusion and transport in carbon nanopores. As different pore models can give very different diffusion coefficients, it is very important to use the "right" model. Insights into the

influence of the assumed pore wall surface on transport will help to choose the right pore model for further studies. In this work, the single-pore transport diffusivities will be incorporated into the PNM to predict the effective diffusivities of the solid. The correct prediction relies on that the correct single-pore diffusivities are used.

1.6 The Hybrid MD/PNM Approach for Transport in Nanoporous Carbons

Some earlier work has been seen using the PNM to study transport in disordered porous media, for example, those of Sahimi and coworkers,[67, 80, 81, 134-136] Burganos and coworkers,[137, 138] and Seaton and corwokers.[76, 139-142] However, none of these work dealt with realistic nanoporous carbons, and none of these work showed the reliability of such an approach.

As we discussed in Section 1.3.2, the PNM is described by a network of pores of distributed size – quantified in terms of the PSD – with an average connectivity, $\overline{Z}$, which are obtained for nanoporous carbons using the characterization method described in Section 1.4. The network model is then mapped to a regular simple cubic lattice, where each bond is associated with a particular pore size, chosen from the appropriate PSD, and each node is associated with the intersection between pores. By deleting some of the bonds on the lattice, the desired connectivity $\overline{Z}$ of the network can be achieved. The effective diffusion coefficient of the network can be obtained by incorporating the single-pore diffusion coefficients to the corresponding pores and averaging over the network.

Several methods exist for solving the PNM to obtain the effective diffusivity. One is to directly solve a set of mass balance equations at the nodes of the network, which is called the direct solution (DS) method. This method has been found computationally demanding as, to obtain an accurate result, the calculation must be repeated over many realizations of the lattice (with pore sizes distributed randomly in each case) and the lattice must be big enough to eliminate the finite-size effect. The computer time required for such calculations is large; for example, it typically requires many

hours on a Sun Station to obtain an accurate result. Approximate solution methods, therefore, have their advantages here. One of the early approximate methods is the effective medium approximation (EMA) approach,[137] which was derived by Kirkpatrick by solving the analogous problem of calculating the effective conductivity of a network of conductors.[143] EMA has been shown to be accurate except near the percolation threshold. (The percolation threshold of a network indicates the bond occupation probability from where the disconnected network becomes connected, for example, the percolation threshold of a simple cubic lattice network is 0.2493.[144]) However, it is sometimes necessary and important to study transport in a network near to the percolation threshold. For example, in the case that the diffusing species are of a comparable size to the pores, some species can experience a network that is close to its percolation threshold because some pores become inaccessible to the species. A more powerful approach was thus proposed by Sahimi *et al.*,[134] in which the renormalization group theory is combined with EMA, to give the so called renormalized effective medium approximation (REMA), to enable calculating the effective conductivity that is more accurate near the percolation threshold than the original EMA. Zhang and Seaton[139] then adapted the basic approach of Sahimi *et al.*[134] to predict the effective diffusivity of solids with continuous pore-size distributions particularly close to the percolation threshold where the original EMA is inaccurate. They also demonstrated the accuracy of the REMA approach, showing that the effective diffusivities predicted from REMA were very close to the results from the direct numerical solution of the mass-balance equations describing diffusion on the simple cubic lattice. The advantage of the REMA method is that it is very fast, only taking several minutes, compared with that the DS method requires many hours for an accurate calculation. Another method, called the critical path analysis (CPA),[145] has also been used for studying transport in the pore network.[76, 142] In the language of transport, the CPA suggests that transport in the pore network is dominated by pores of the critical pore size and that pores much smaller or larger than this value play little role. Rather than the effective diffusivity of the pore network that we are interested in, the CPA determines the critical pore size of the pore network for transport and the ratio of diffusion coefficients of mixtures.[141] In this work, we will use the REMA method to predict

the effective diffusivity in the network of nanoporous carbons, because it is fast, accurate and more rigorous.

Previous researchers who applied REMA to predict effective diffusivity in porous media did not relate their work to real nanoporous carbons. First, most of previous work calculated the single-pore diffusivities using analytical models which are not correct models for studying transport in pores of nanoporous carbons, as discussed in Section 1.2.2. Second, though Seaton and coworkers did calculate single-pore diffusivities using MD simulation which is a better means for calculating single-pore diffusivities,[76, 141, 142] they built their pore networks using an assumed PSD and assumed connectivity for the solid, as the other researchers did. The PSD in their work was usually taken as a binary PSD,[134, 137] or a lognormal PSD.[76, 139, 141, 142] So the pore networks they studied were not the representative of real nanoporous carbons. And so the applicability of the pore network model to the real nanoporous carbons has not yet been investigated. Previous work has shown that different PNMs could give very different effective diffusivities.[55] Our work here is thus very important as it is the first time that transport in the PNM based on real nanoporous carbons is studied. Moreover, although it has been shown that the predicted effective diffusivities from REMA were consistent with the more rigorous DS method; the correctness of the effective diffusivities, compared with that in real solids, has never been checked

1.7 Objectives of this Work

The objective of this work is to develop a validated approach – the so called hybrid MD/PNM approach for predicting effective diffusion coefficients in nanoporous carbons. This approach provides a routine for predicting the effective diffusion coefficients by incorporating the diffusion coefficients in single pores onto the PNM which grasps the geometrical and topological structure of real carbons. Most importantly, the main goal of this work is to validate the hybrid MD/PNM approach. Such an attempt is briefly described as follows. The VPCs, with known structure and the ability of generating the adsorption isotherms and effective diffusion coefficients,

are used to replace real nanoporous carbons in the laboratory. Firstly, the conventional adsorption-based characterization method, which has been used widely for characterizing real carbons, as discussed in Section 1.4, will be used to characterize the studied VPC to obtain the PSD and the value of $\overline{Z}$ of the corresponding PNM. Secondly, MD simulation will be used to examine transport in single pores and the database of single-pore diffusivities will be built using the "right" pore model. The effective diffusion coefficient, D_e, will then be predicted for a solid in a matter of minutes. Finally, the hybrid MD/PNM will be evaluated, given that the porous structure of the VPC is known, and the predicted effective diffusivity from the hybrid MD/PNM can be compared directly with that of the VPC. This will give us how reliable the hybrid MD/PNM approach is in predicting effective diffusion coefficients in carbons.

1.8 Outline of the Thesis

This thesis is organised as follows. Chapter 2 deals with the adsorption-based characterization of the virtual porous carbons (VPC) to obtain the pore size distribution (PSD). Details of the grand canonical Monte Carlo (GCMC) simulation of adsorption are given. The consistency of the PSD is checked by comparing the predicted adsorption based on the PSD with that from the VPC, whilst the correctness of the PSD is evaluated by comparing it with the known structure of the VPC. This part of the work shows the applicability and also the limitations of the characterization method. Chapter 3 continues the study in Chapter 2, to obtain the average connectivity $\overline{Z}$ of the VPC. This is done by using percolation theory to analyze the PSD obtained in Chapter 2. So far, the pore network model (PNM) of the VPC is built up using the PSD and the average connectivity $\overline{Z}$. Chapter 4 presents the single-pore diffusivities using molecular dynamics (MD) simulation. The MD simulation techniques, together with the fundamentals of diffusion, are presented. The effect of the assumed pore wall surface (smooth, atomic and diffusive) on both self-diffusion and transport diffusion is investigated. The conclusions drawn from this part of the work help us to choose the right pore surface model for calculating the single-pore diffusivities. The prediction of the effective diffusivity based on the

PNM and the single-pore diffusivities is finally given in Chapter 5. The details of the REMA method that is used to solve transport over the pore network are also given. This hybrid MD/PNM approach is also evaluated by comparing its predicted effective diffusivity with the one from the VPC. Moreover, the detailed investigation on the factors that influence the predicted effective diffusivity reveals how the materials should be designed to meet the requirement of their applications. Finally, overall conclusions drawn from this work are given in Chapter 6, showing the potential use of the hybrid MD/PNM in an industrial context.

2. Determination of the Pore Size Distribution of Nanoporous Carbons

In this chapter, the PSDs of VPCs are determined. As we discussed in chapter 1, this is the first step to build the PNM. The pore size distribution, $f(w)$, is obtained by solving the adsorption integral equation:

$$N(T,P) = \int_0^\infty \rho(w,T,P) f(w) dw \tag{2.1}$$

where $N(T,P)$ is the experimentally determined adsorption (in this work, we term the computation determined adsorption in the VPC as "experimental" adsorption) at temperature, T, and bulk pressure, P, and $\rho(w,T,P)$ is the adsorption of the same fluid in an individual model pore of width w (the "single-pore isotherm").

There are three stages to obtain the PSD of a real carbon or – in this case – a VPC: (1) generate a database of single-pore isotherms using GCMC simulation, (2) obtain the experimental isotherms for the carbon of interest, and (3) invert the adsorption integral Eq. 2.1 to obtain the PSD. Once the PSD of the carbon is obtained, the experimental adsorption on the same material, $N(T,P)$, can be predicted using Eq. 2.1, given the database of single-pore isotherms, $\rho(w,T,P)$, at the desired temperature and pressure. The consistency of the obtained PSD can be examined by comparing the predicted adsorption with the real experimental measurement of adsorption on the material.

As discussed in Chapter 1, three species of increasing molecular size with spherical molecular structure – CH_4, CF_4, and SF_6 are used to probe the porous structure. The idea of using three species as adsorptive is to obtain a more complete picture of the PSD (the so called overall PSD) by combining the partial PSDs from the three species, as species with different molecular sizes probe different ranges of pore size. This overall PSD will be used to predict the experimental adsorption for these three

species at different temperatures – 258 K, 275 K and 296 K (The temperatures are chosen to be around the room temperature, so that the three species are gases at the super- or sub-critical state. It is also related to the practical application of CH_4 storage which is taken at room temperature.) to check the consistency of this overall PSD. Thus, a database of single-pore adsorption isotherms for three species at three temperatures needs to be built using GCMC simulations.

The correctness of the PSD obtained by solving Eq. 2.1, which we call the PNM-PSD, is also examined using the absolute assessment methodology. As we are characterizing the VPC whose structure is exactly known, PNM-PSD can be compared against the corresponding exactly known structure of the VPC (termed as VPC-PSD). This will enable us to draw conclusions regarding the correctness of the characterization method.

This chapter is organized as follows. Section 2.1 gives a detailed description of the GCMC simulation method to generate the database of the single-pore isotherms. Section 2.2 gives the description of the VPC and shows the "experimental" adsorption isotherms on two different VPCs. Section 2.3 then brings the single-pore isotherms and the experimental isotherms together, to obtain the PSDs by solving Eq. 2.1. The consistency of the PNM-PSDs is examined in this section. Section 2.4 compares the PNM-PSD with the VPC-PSD, to examine the correctness of the PNM-PSDs. Conclusions of this chapter are given in Section 2.5.

2.1 Grand Canonical Monte Carlo (GCMC) Simulation of Adsorption in Slit Model Pores

2.1.1 From microscopic to macroscopic

Statistical mechanics enables us to relate the macroscopic properties of a system that can be measured in experiments to molecular scale properties that can be calculated with computer simulation. Monte Carlo is a computer simulation method of calculating macroscopic properties of a system, by randomly sampling from an ensemble of microstates. An ensemble is defined as a collection of a large number of microstates, each constructed to be a replica at the microscopic level of the actual

system.[146] If the system is observed for an infinite time it will go through all possible microstates. A basic postulate of statistical mechanics says that the time average of one macroscopic property is equal to the ensemble average of that property as the number of microstates approaches infinity.[147] Thus, it is possible to calculate a macroscopic property of interest, $M_{observed}$, by averaging over a large enough ensemble, according to:

$$M_{observed} = \langle M \rangle_{Ensemble} = \sum_{i}^{microstates} M_i \alpha_i \tag{2.2}$$

where M_i is the value of the property of interest in microstate i, α_i is the probability of observing that microstate in the ensemble, and the angular bracket denotes an ensemble average. α_i can be calculated making use of the second postulate of statistical mechanics[147] which essentially states that microstates with the same energy occur with equal probability.

To calculate the ensemble average of a certain property according to Eq. 2.2, one would have to compute a sum over all possible microstates (or, in the classical sense, an integral over the positions of all molecules). However, this is impossible because there are sufficiently numerous microstates in most systems. This problem is overcome by using the theory of Monte Carlo integration and the concept of "importance sampling".[148] The theory of Monte Carlo integration is used to estimate Eq. 2.2 using

$$M_{observed} = \left\langle \frac{M_i \alpha_i}{\chi_i} \right\rangle \tag{2.3}$$

where χ_i is the probability of choosing a particular microstate to evaluate the property and the angular bracket denotes taking an average over a number of trial microstates. If all the trial microstates are chosen completely at random, which implies that they all have the same probability of being chosen, Eq. 2.3 becomes

$$M_{observed} = \Omega_{Microstates} \langle M_i \alpha_i \rangle \tag{2.4}$$

where $\Omega_{Microstates}$ is the total number of microstates in the ensemble.

The concept of importance sampling, concentrating on the "important" microstates that occur with a much higher probability than others, can substantially reduce the number of microstates included in the calculation. If the probability of choosing the microstate, χ_i, is set equal to the probability of observing the microstate, α_i, Eq. 2.3 simplifies to

$$M_{observed} = \langle M_i \rangle \tag{2.5}$$

Eq. 2.5 states that microstates must be chosen proportionally to their probability of occurrence. Metropolis *et al.*[148] achieve this by generating a Markov chain of microstates. The Markov chain mainly implies that any new state should depend only on the previous one and must be microscopically reversible – the probability for the microstate to evolve forward must be the same as if it goes backwards.

Different ensembles are obtained by keeping different thermodynamic variables fixed. The most widely used ensembles are (see *e.g.*, Frenkel & Smit, 1996[149]):

i) the microcanonical ensemble, in which the number of molecules N, the energy E and the volume V are kept constant;
ii) the canonical ensemble, in which the number of molecules N, the temperature T and the volume V are kept constant;
iii) the grand canonical ensemble, in which the chemical potential μ, the volume V and the temperature T are kept constant;
iv) the isobaric-isothermal ensemble, in which the number of molecules N, the pressure P and the temperature T are kept constant.

The choice of the ensemble depends thus on the thermodynamic properties of interest and also on the system studied. As will be shown next, the grand canonical ensemble is the most suitable to describe adsorption problems.

2.1.2 Grand canonical Monte Carlo (GCMC) simulation and adsorption

For adsorption studies, a natural ensemble to use is the grand-canonical ensemble. In this ensemble, the temperature T, volume V, and chemical potential μ, are fixed. In the experimental setup, the adsorbed gas is in equilibrium with the adsorptive gas in

the reservoir. The equilibrium conditions are that the temperature and chemical potential of the adsorptive inside and outside the adsorbent must be equal. The adsorptive that is in contact with the adsorbent can be considered as a reservoir that imposes a temperature and chemical potential on the adsorbed gas. We therefore have to know only the temperature and the chemical potential of this reservoir to determine the equilibrium concentration inside the adsorbent. This is exactly what is reproduced in the grand-canonical ensemble: the temperature T and chemical potential μ are imposed and the number of molecules N is allowed to fluctuate during the simulation.

As the number of molecules fluctuates during the simulation, the system experiences different microstates. The criteria for accepting a generated microstate are based on the probability of observing the microstate in the given ensemble. The classical equivalent of a microstate probability is referred to as the density probability, ρ_i. For a grand canonical ensemble of microstates of a system that contains a single adsorptive, the density probability of observing a microstate is given by:[150]

$$\rho_i = \frac{1}{\Xi} \cdot \frac{V_i^{N_i}}{\Lambda_i^{3N_i} N_i!} e^{\beta \mu_i N_i} e^{-\beta U_i(r)} \tag{2.6}$$

where N_i is the number of molecules, μ_i is the chemical potential of the microstate i, $U_i(\boldsymbol{r})$ is the potential energy which only depends on the positions of the molecules $\boldsymbol{r}$, Ξ is the classical grand canonical partition function (i.e. the integral of all possible microstates), $\beta = \frac{1}{k_B T}$ and k_B is the Boltzmann constant, Λ_i is the de Broglie thermal wavelength. The de Broglie wavelength can be related to the fugacity, f_i, by the equation (*e.g.* Allen & Tildesley, 1989[151]):

$$\Lambda_i^{-3} = \frac{\beta f_i}{e^{-\beta \mu_i}} \tag{2.7}$$

In the GCMC method, adsorbed molecules are in equilibrium with the bulk phase (*i.e.* the chemical potential of each species inside the pore is the same as outside).

The chemical potential is related to the temperature and the pressure of the bulk gas phase:

$$\mu_i = \mu_i^0 + RT \ln\left(\frac{P_i}{P_i^0}\right) \tag{2.8}$$

where the superscript, 0, in the above equation, denotes the standard state.

In this work, the fugacity, f_i, is related to the pressure, P, by the Peng-Robinson equation of state:[152]

$$P = \frac{RT}{\underline{V} - b} - \frac{a}{\underline{V}(\underline{V} + b) + b(\underline{V} - b)} \tag{2.9}$$

where $\underline{V}$ is the molar volume, a and b are the equation of state parameters, calculated as follows by using the thermodynamic parameters of gases (e.g. critical pressure P_C, critical temperature T_C and acentric factor ω).

$$a = 0.45724 \frac{R^2 T_C^2}{P_C} \alpha \tag{2.10}$$

$$b = 0.07780 \frac{RT_C}{P_C} \tag{2.11}$$

$$\sqrt{\alpha} = 1 + \kappa\left(1 - \sqrt{\frac{T}{T_C}}\right) \tag{2.12}$$

$$\kappa = 0.37464 + 1.54226\omega - 0.26992\omega^2 \tag{2.13}$$

Parameters associated with using the Peng-Robinson equation are summarized in Table 2.1.

Table 2.1 Thermodynamic parameters of gases[153] for Peng-Robinson equation

	Critical Pressure T_C (MPa)	Critical Temperature P_C (K)	Acentric Factor ω
CH_4	4.599	190.6	0.008
CF_4	3.745	227.5	0.1777
SF_6	3.71	318.7	0.286

In our GCMC simulations, three possible changes, i.e. displacement of molecules, creation of molecules or removal of molecules, are made to generate the new microstate. The acceptance criteria for each of the three possible changes are obtained by evaluating the ratio of the probability of observing the new microstate, $\rho(n)$, over the probability of observing the old microstate, $\rho(o)$. These changes are made using the condition of microscopic reversibility, i.e. the probability of a change occurring from state o to state n must be the same as the probability of a change occurring from state n to state o. The criteria for accepting each trial are deduced from the density probabilities defined by Eq. 2.6, given as follows.

i) Displacement of molecules. A molecule is selected at random and given a new conformation (for example, in the case of moving the molecule to a new position). This move is accepted with probability:

$$\left(\frac{\rho(n)}{\rho(o)}\right)_{Move} = e^{-\beta \Delta U_i} \tag{2.14}$$

ii) Creation of molecules. A molecule is inserted at a random position (for example, in the case of a new molecule adsorbed). The creation of a molecule is accepted with probability:

$$\left(\frac{\rho(n)}{\rho(o)}\right)_{Creation} = \frac{f_i \beta V}{\mathrm{N}_i + 1} \cdot e^{-\beta \Delta U_i} \tag{2.15}$$

iii) Removal of molecules. A randomly selected molecule is removed (for example, in the case of a molecule desorbed). The removal of a molecule is accepted with probability:

$$\left(\frac{\rho(n)}{\rho(o)}\right)_{\mathrm{Re}\,moval} = \frac{\mathrm{N}_i}{f_i \beta V} \cdot e^{-\beta \Delta U_i} \tag{2.16}$$

In the above expressions, i represents the species, and ΔU_i is the change of the potential when the system goes from state o to state n. The calculation of ΔU_i is to

be addressed in Section 2.1.4. If $\frac{\rho(n)}{\rho(o)} \geq 1$ then the new configuration is accepted unconditionally. If the ratio is less than one then the new configuration is accepted stochastically, *i.e.*, the new configuration is accepted, or rejected, in accordance with a random number chosen from a uniform distribution in the interval [0, 1].

In summary, we are able to generate a succession of molecular configurations by attempting to move, create, or remove a molecule in the previous microstate. The new microstate is accepted, and thus forms the next microstate in the succession of microstates based on the criteria given in Eq. 2.10-2.12. Such a succession of molecular configurations forms an appropriate Markov chain of microstates that can be used to evaluate the properties of a system in the grand canonical ensemble. The primary property that we are interested in is the number of molecules of each species adsorbed.

2.1.3 The pore model

GCMC simulations of adsorption are carried out in slit carbon pores, to obtain adsorption isotherms in a series of single pores. The database of single-pore isotherms, together with the experimental measurement of adsorption on the carbon of interest, are then input to Eq. 2.1, to obtain the PSD of the carbon. The slit carbon pores are defined by the basal surfaces of two opposing semi-infinite blocks of graphite – and are hence termed here basal-plane slit pores – and the width, w, is defined as the distance between the centre of the surface carbon atoms of the opposing pore walls.

Periodic boundary conditions are applied. The slit-shaped model pore is replicated along the graphite plane (i.e. in the x and y directions), to form a semi-infinite slit-shaped model pore. A semi-infinite slit-shaped model pore only has a well-defined pore width (in the z direction). Although the simulation cell will have well-defined x and y dimensions (for example, each graphite plane has a size of 100Å×100Å in the x and y directions), the periodic boundary conditions imply that the actual slit shaped pore is infinite in these directions. Figure 2.1 shows a slit carbon pore and how the

periodic boundary conditions are applied. Thus, in this case, a small infinitely periodic system is used to represent the macroscopic system. It is important to ask if the properties of a small, infinitely periodic system, and the macroscopic system which it represents, are the same. In general, periodic boundary conditions work well for the equilibrium thermodynamic properties and structures of fluids away from phase transitions.[151]

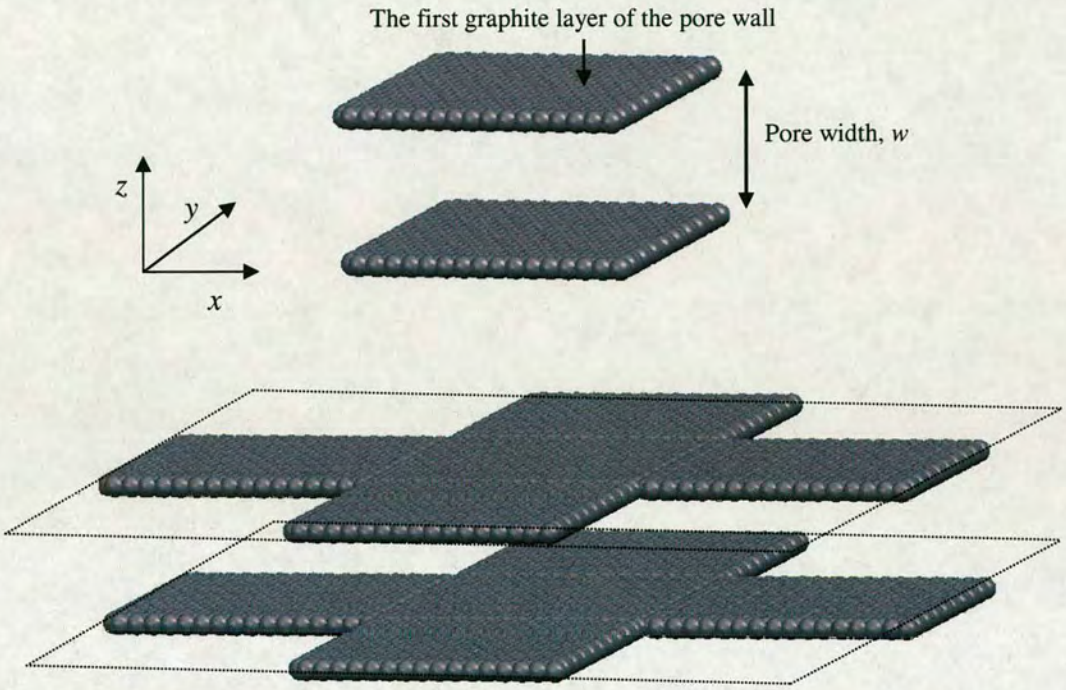

Figure 2.1 Top: schematic illustration of the slit carbon pore. Bottom: schematic illustration of how the periodic boundary conditions are applied to the slit pore.

2.1.4 Calculation of the potential

Three different gases - CH_4, CF_4 and SF_6 - are used as adsorptives to probe the pore size distributions of the VPCs. As CH_4, CF_4 and SF_6 are all approximately spherical, we describe their interactions by the Lennard-Jones 12-6 potential:[151]

$$U_{ff}(r) = 4\varepsilon_{ff}[(\frac{\sigma_{ff}}{r})^{12} - (\frac{\sigma_{ff}}{r})^{6}] \qquad (2.17)$$

where σ and ε are the molecular size and energy parameters respectively. The Lennard-Jones parameters of these three gases used in GCMC simulations are given

in Table 2.2. In the simulations, the potential is truncated at 15 Å, beyond which the fluid-fluid interactions are ignored.

Table 2.2. Lennard-Jones parameters[54] used in GCMC simulations.

Molecule	ε/κ_B, K	σ, Å
CH_4	149.92	3.7327
CF_4	152.5	4.70
SF_6	200.9	5.51
C	28.0	3.4

The graphite planes are considered to be smooth and their interaction with an adsorbate molecule is represented by Steele's 10-4-3 potential[154]

$$U_{sf}(z) = 2\pi\rho_s\varepsilon_{sf}\sigma_{sf}^{\ 2}\Delta[\frac{2}{5}(\frac{\sigma_{sf}}{z})^{10} - (\frac{\sigma_{sf}}{z})^4 - \frac{\sigma_{sf}^{\ 4}}{3\Delta(0.61+z)^3}] \qquad (2.18)$$

Here, $\Delta = 0.335\,\text{nm}$ is the distance between the two graphite planes, $\rho_{sf} = 114\,\text{nm}^{-3}$ is the number of carbon atoms per unit volume in perfect graphite (which is related to the number of carbon atoms per unit surface area in the basal plane $\rho_A = \rho_{sf}\Delta = 114\times0.335 = 38.19\,\text{nm}^{-2}$) and z is the perpendicular distance between the site in an adsorbate molecule and the adsorbent surface. σ_{sf} and ε_{sf} are the solid-fluid LJ parameters which are determined using the standard Lorentz-Berthelot combination rules:

$$\sigma_{ij} = \frac{\sigma_{ii} + \sigma_{jj}}{2} \qquad (2.19)$$

$$\varepsilon_{ij} = \sqrt{\varepsilon_{ii} \times \varepsilon_{jj}} \qquad (2.20)$$

The overall adsorbate-adsorbent interaction is given by summing up the interaction of an adsorbate molecule with the two walls:

$$U_{overallsf}(z) = U_{sf}(z) + U_{sf}(w-z) \qquad (2.21)$$

2.1.5 The GCMC program and the properties that it delivers

A GCMC simulation follows the basic steps shown in Figure 2.2. At the start, the system needs to be set up. This includes specifying (1) temperature and pressure, (The adsorption is measured with the temperature fixed and increasing pressure to obtain an isotherm, so a series of pressure points should be supplied and the code

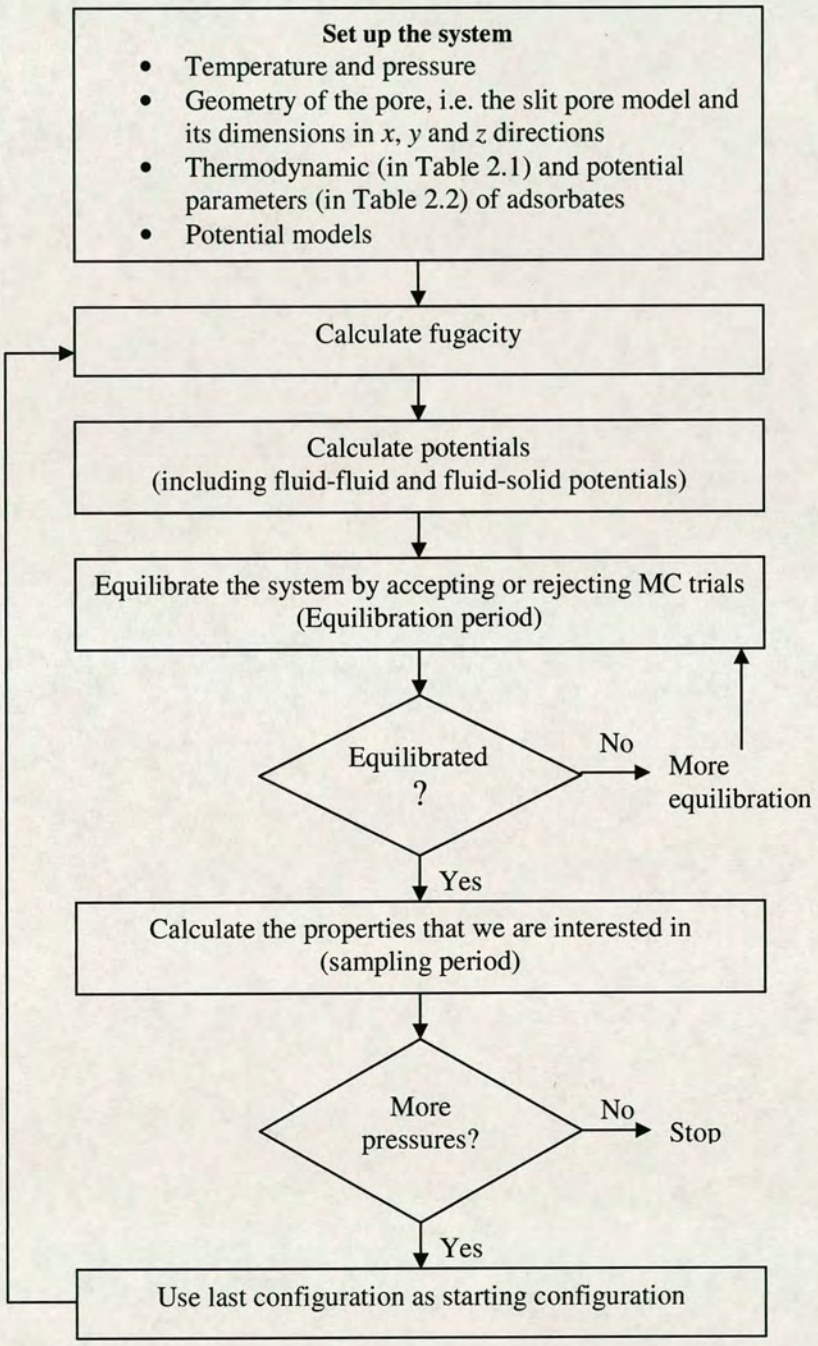

Figure 2.2 Schematic diagram showing the basic structure of a GCMC program

performs a loop over all pressures, enabling the calculation of a complete isotherm in a single run.) (2) the geometry of the pore which is described in Section 2.1.3, (3) thermodynamic parameters of the adsorbates shown in Table 2.1 and (4) the potential models given in Section 2.1.4. Once the system is set up, the simulation begins. We start with an empty pore. In this case, the simulation mimics the adsorption process on a fresh adsorbent, and does not need any initial configuration of molecules. Alternatively, an initial configuration can be generated. This can be done either by reading from an existing file or by replacing a predetermined number of molecules at random in the simulation cell.[155] If the number of molecules used to generate the initial configuration is close to the number of molecules to be actually adsorbed in the pore, the program performs faster than starting from an empty pore to reach equilibrium and gives more accurate results. From the initial configuration, the system is allowed to move toward the equilibrium state and then kept at equilibrium for sampling data. Thus, the simulation is divided into two periods: the equilibration period and the sampling period. Each period goes for a number of MC steps; in each step molecules are moved, created or removed according to the acceptance criteria in Eq. 2.9-2.11, in which the fugacity of the adsorbate (which is calculated using Peng-Robinson equation, i.e. Eq. 2.8.) and the potential of the system (including fluid-fluid potential and fluid-solid potential which are calculated using equations given in Section 2.1.4) are needed. After equilibrium, the properties that we are interested in can then be calculated by averaging the properties over a sampling period.

It is very important that the data are collected when the system is in equilibrium. This means that the equilibration period should be long enough to allow the system to reach equilibrium. This can be checked by examining the evolution of the adsorbed amount with the number of MC steps as the simulation progressed, as show in Figure 2.3. The necessary length of the equilibration period depends on numerous factors, such as temperature and pressure, the pore width, and the adsorptive. For example, the development of the CH4 molecules with the number of MC steps is more chaotic than that of the relatively stronger adsorbed SF6, as shown in Figure 2.3. After equilibration, data is collected over a sampling period. The sampling period must also be long enough to reduce the statistical error to an acceptable value. For all the

GCMC simulations carried out in this chapter, at each pressure point, the system is allowed to equilibrate over 10^6 steps, where a Monte Carlo step involves one random creation/destruction attempt and a move. After equilibration data are collected over a further 10^6 steps.

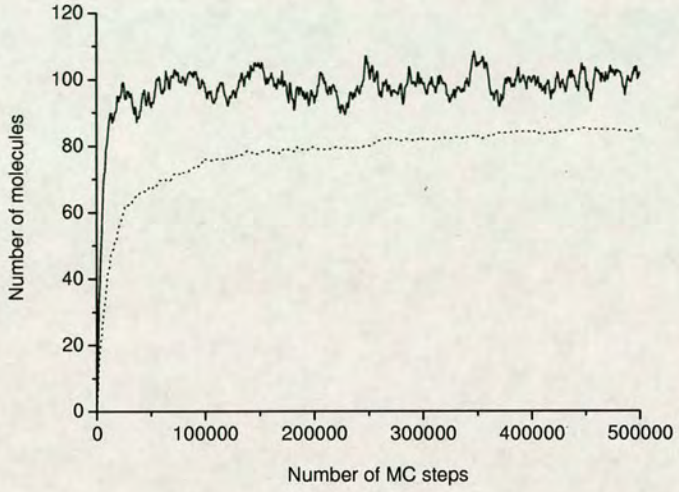

Figure 2.3 Plot of the number of adsorbed CH_4 (solid line) and SF_6 (dotted line) molecules in a pore of 8 Å at 296 K and 1 bar, as a function of the number of Monte Carlo steps during the course of a simulation run.

Adsorption Isotherm

The primary property that we are interested in from a GCMC program is the adsorption isotherm, which shows how at a given temperature, as the pressure changes, the number of molecules adsorbed changes. The isotherm can be presented either using the number of molecules or the density in the pore. The density of each species is calculated by averaging the number of molecules in each individual pore, $<N_i>$.

$$\rho_i = \frac{\langle N_i \rangle}{N_A V} \tag{2.22}$$

where N_A is Avogadro's number and V represents the volume of the simulation cell.

Figure 2.4 shows the adsorption isotherms of CH_4 and SF_6 in a pore of 8 Å at 296 K and 1 bar, in terms of number of molecules. Error bars here are calculated using the

t-test at the confident limit of 95%. Data are collected from the simulations using the equilibration and sampling periods that are long enough as specified.

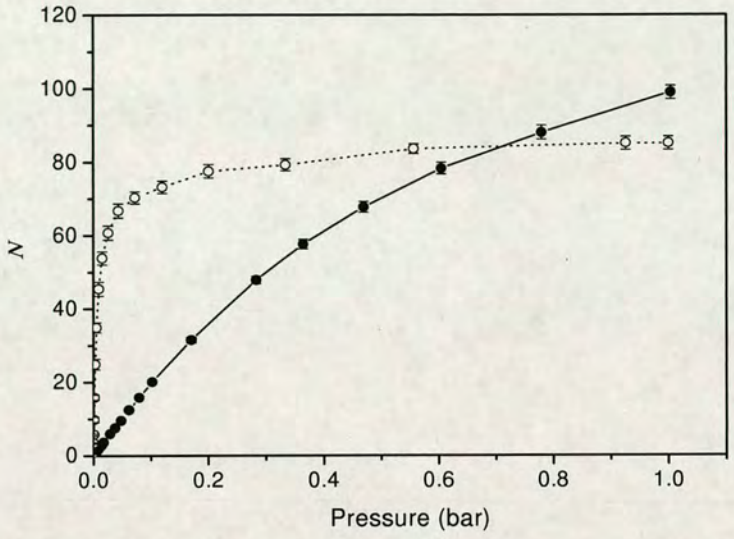

Figure 2.4 Adsorption isotherms of CH_4 (filled circles) and SF_6 (empty circles) in a pore of 8 Å at 296 K.

Density Distribution Function

As we discussed above, the density of the adsorbed species in the pore is calculated as the average density over the whole pore. However, this density varies across the pore width (for example, in some pores, the molecules can form layers along the pore walls while few molecules can be found in the centre of the pore). This variation can be captured during the simulation by calculating density profiles. This is done by dividing the simulation cell along the z coordinate into several slices and counting the number of molecules that are present in each slice, at any instant during the simulation run. 100 slices are used to ensure that statistically meaningful results are obtained. A density distribution function along the z direction thus can be constructed. The ensemble average of this function, at the end of the sampling period, gives us the density profile of the adsorbate in the pore. Figure 2.5 shows an example of the density distribution of methane in a pore of 19.0 Å at 296 K and 1 bar.

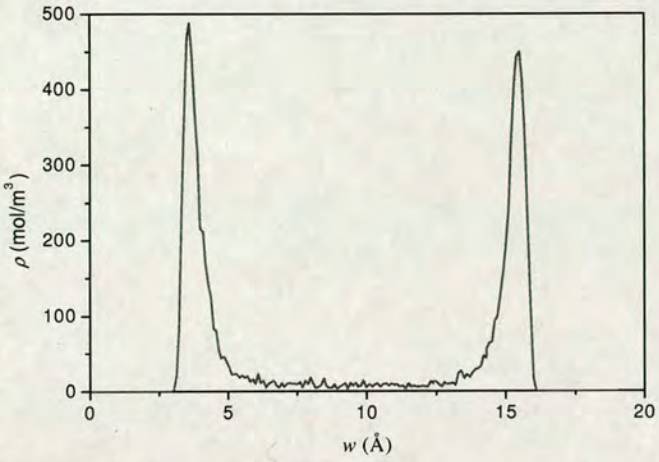

Figure 2.5 Density distribution of CH_4 in a pore of 19.0 Å at 296 K and 1 bar.

2.1.6 Adsorption isotherms of CH_4, CF_4 and SF_6 in slit model pores

The adsorption isotherms in a series of selected pores are given in Figure 2.6 for CH_4, Figure 2.7 for CF_4 and Figure 2.8 for SF_6. As very little adsorption occurs in pores smaller than $w = 7$ Å for CH_4, and in pores smaller than $w = 8$ Å for CF_4 and SF_6, the adsorption isotherms in these pores are not shown here. These figures all exhibit the well known characteristics of adsorption in small pores. For example, at lower pressures the greatest adsorption occurs in the smallest pores. This is due to smaller pores having higher adsorbate-adsorbent interaction potentials. At higher pressures, the ability to physically accommodate more adsobate molecules as the pore size increases affects the shape of the isotherm. In this case, despite the decrease in the adsorbate–adsorbent interaction potential, the adsorption increases. Such increases in the adsorption capacity can be associated with an adsorbate packing transition. This shows that the adsorption is the interplay of many factors such as the pore size, the pressure and the strength of the adsorbate-adsorbent interaction. It is worth noting here that the gas bulk density is much lower than the density of the gas adsorbed in the pores at the same temperature and pressure. For example, the bulk density of CH_4 at 258 K and at 1.0 bar is 0.046 mmol/cm^3, which is nearly negligible compared to the values of CH_4 density in all the pores shown in Figure 2.6. This shows the strong attraction of nanopores to gases and so the adsorption of gases in these pores is favoured.

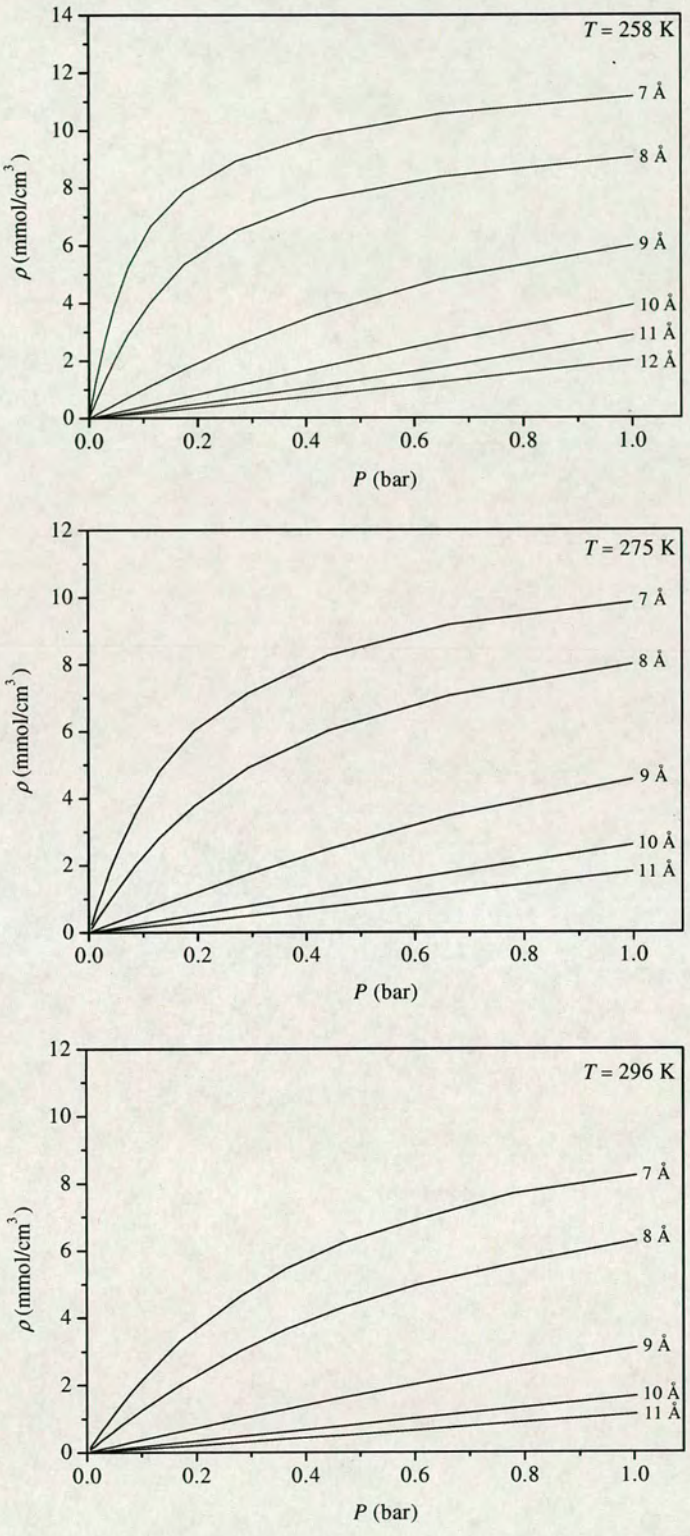

Figure 2.6 Isotherms for adsorption of CH_4 in slit-shaped pores of various widths at the three temperatures considered.

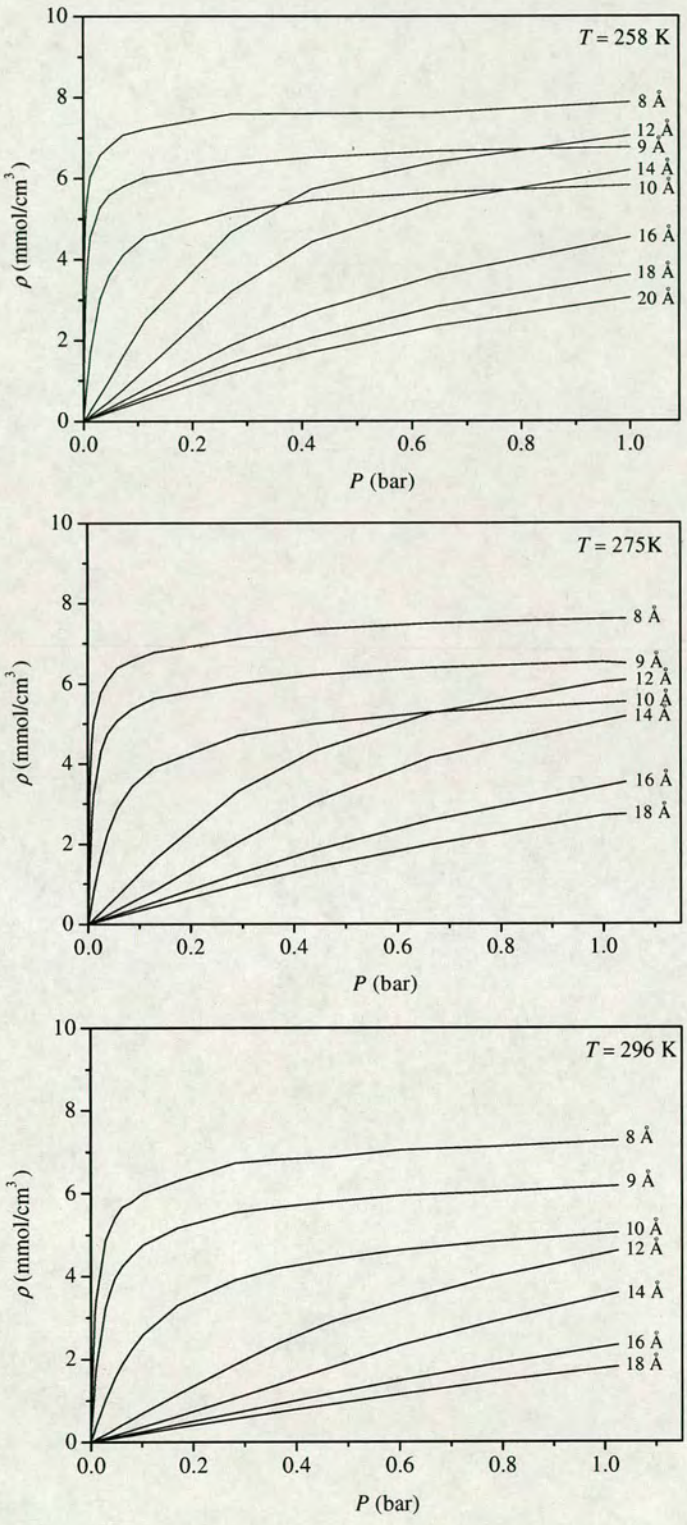

Figure 2.7 Isotherms for adsorption of CF_4 in slit-shaped pores of various widths at the three temperatures considered.

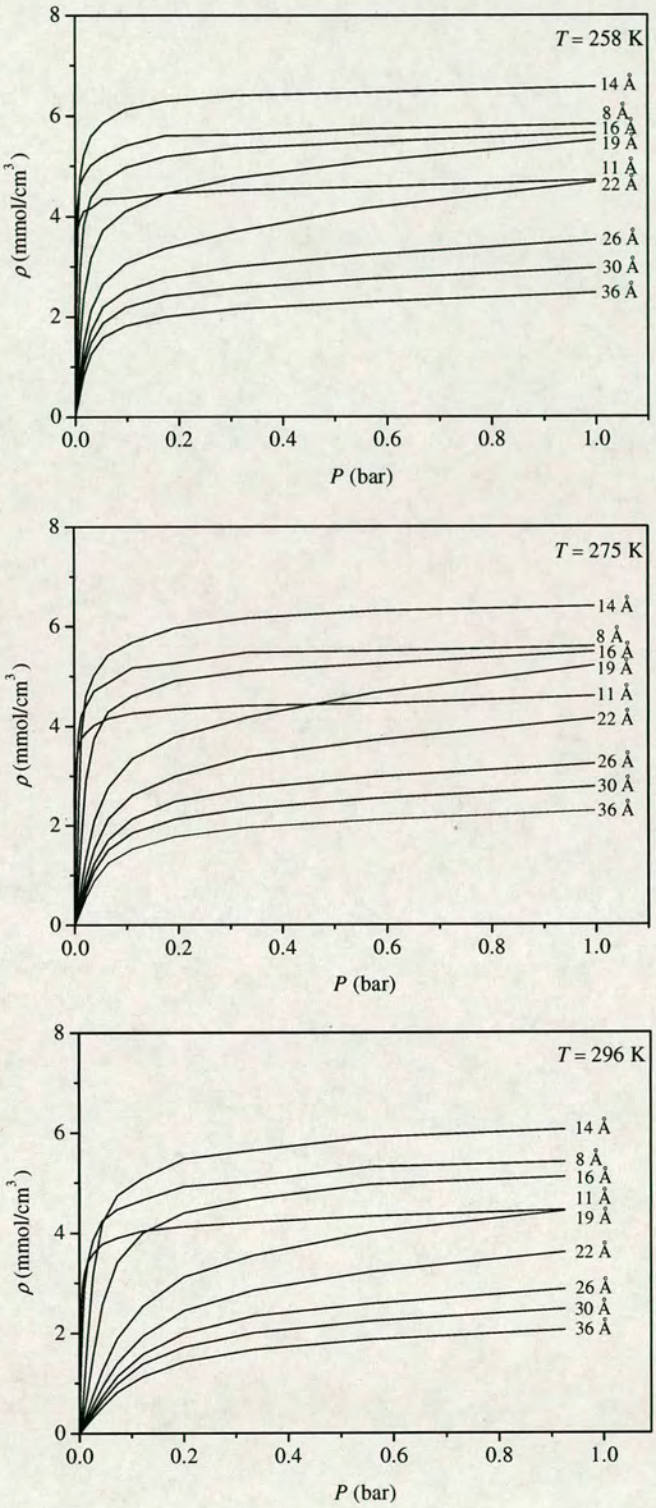

Figure 2.8 Isotherms for adsorption of SF_6 in slit-shaped pores of various widths at the three temperatures considered.

For all the three gases, a decrease in adsorption as the temperature increases can be seen. Figure 2.6 shows that the adsorption of CH_4 decreases as the pore width increases, and that the isotherms follow Henry's law when the pore width is greater than $w = 9$ Å. Figure 2.7 shows simulated isotherms for CF_4. Since the adsorption of CF_4 is stronger than CH_4, its isotherms reflect a more rapid pore filling. The adsorption of CF_4 also decreases as the pore width increases. SF_6 shows the strongest adsorption, compared with CH_4 and CF_4, as shown in Figure 2.8. The adsorption decreases from $w = 8$ Å to $w = 11$ Å, and then increases to $w = 14$ Å. The adsorption capacity is given by the high-pressure plateau of the isotherm. The capacity is the highest at $w = 14$ Å, from where the adsorption begins to decrease with increasing the pore width. This behaviour is the result of the correlation between the pore size and the molecule size. In pores wider than $w = 11$ Å, a second layer of molecules begins to form and is complete when the pore width reaches $w = 14$ Å. Pores wider than $w = 20$ Å become able to accommodate a third layer of SF_6. Some of the isotherms for CF_4 and SF_6 cross. This is due to the competition between strength of adsorption and packing effect in pores of different sizes.

2.2 Adsorption in Virtual Porous Carbons

2.2.1 Overview of the VPC

There is a vast array of experimental evidence[156] to suggest that nanoporous carbons are built up from domains of two-dimensional (2D) short-range order that may be reasonably represented by small polyaromatic molecules or similar structures. These domains assemble in a roughly aligned manner with out-of-plane spacing somewhat greater than that of graphite to form nanoscale regions of *local molecular orientation* (LMO). The size of these regions of LMO may be as small as that of the 2D short-range order in the case of highly microporous non-graphitic carbons, through to micrometers for graphitic carbons. The regions of LMO combine to form mesoscopic structures.

Biggs and coworkers have used this conceptual view of carbons as a basis for virtual porous carbons that match various experimental data.[47] Two VPCs, termed Carbon 1

and Carbon 2, generated by this approach, have been used in the work reported here – the essential differences between these two carbons, as will be seen below, is that the first has a substantially smaller porosity and contains porosity that becomes inaccessible to SF_6, the largest adsorptive, as the temperature is decreased from 296 K to 258 K. The porosities of the two carbons are 0.36 for Carbon 1 and 0.49 for Carbon 2.

The nature of the porosity in the carbons is illustrated in Figure 2.9. This figure shows that the pore space is complex in character with a wide variety of pore shapes, sizes (length and breadth, as well as width) and surface textures. This mixture of different surfaces and geometries decouples the rigid link between pore size and energy that exists in simpler models (such as the pore network model) and, therefore, provides a good basis for testing characterization methods based on such simpler models. Previous work[90] has shown that simulation of adsorption on these VPCs can yield a wide range of isotherm shapes that are seen experimentally, as well as the experimentally observed decrease of heat of adsorption with increasing loading.

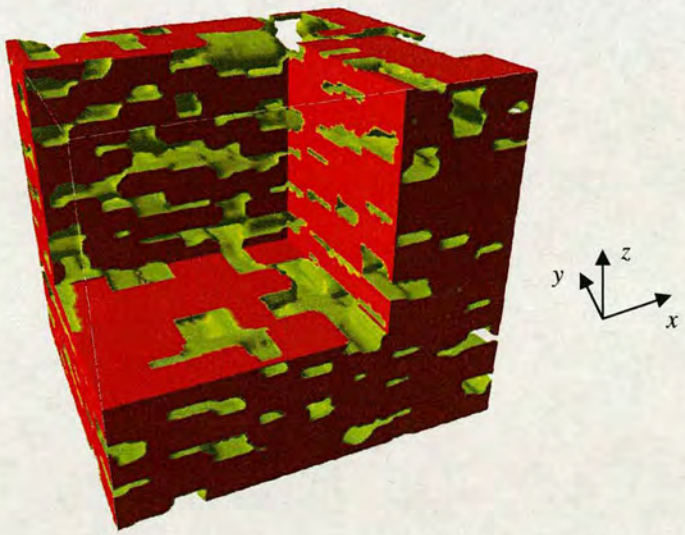

Figure 2.9 Isoenergy map of a microporous region of Carbon 2. Red and yellow indicate regions of solid and pore respectively.[157] The dimensions of the VPC shown here are 88.42 Å, 76.57 Å, and 80.50 Å respectively in the x, y and z directions.

2.2.2 Geometrical analysis of porosity of VPCs

The pore space of the VPCs is analyzed directly to determine the porosity, pore size distribution and connectivity.[157] The pore space is first subdivided into individual pores using an algorithm similar to that of Thovert *et al.*[158] A cubic lattice is superimposed on the virtual solid and the energy of fluid-solid interaction is calculated at each node of the lattice; the lattice cell size is chosen to be substantially less than the characteristic size of the interaction. Nodes of the lattice where the interaction energy is positive and higher than some limit are designated as lying in the solid phase. All other nodes are considered to be part of the pore volume. Nodes that belong to the pore volume are subject to cluster analysis[159] to identify those nodes that belong to the percolating clusters and, if they exist, isolated clusters. The pore volume is then split into separate pores by removing the outer layer of the clusters until only convex hulls remain; this may very well lead to an original cluster breaking up into multiple convex hulls. Each convex hull is considered to be the kernel of a pore. The exact extent of each pore is then determined by re-expanding all the kernels layer by layer until they can expand no further due to their coming into contact with other, adjacent, re-expanding kernels.

The size of a pore identified using the above algorithm is equal to the size of the largest sphere that may be inserted into the pore. The pore size distribution functions of the two VPCs (i.e. VPC-PSD), determined in this way, are given in Section 2.4, for comparison with the PSDs to be obtained in Section 2.3 based on the pore network model (i.e. PNM-PSD).

2.2.3 Adsorption on VPCs

The isotherms for the VPCs, taking the role of "experimental isotherms", are simulated by GCMC simulation on the percolating clusters only; full details of the simulation protocol may be found in ref. [90]. The isotherms, which are shown in Figure 2.10 for both carbons, are reported for three temperatures – 258 K, 275 K and 296 K – for each adsorptive. These isotherms show "experimentally" the development of adsorption with increasing temperature and the difference between

different adsorptives. When comparing the isotherms from the two carbons, it shows clearly that the adsorption on Carbon 1 is less than that on Carbon 2, consistent with its lower porosity. On Carbon 2, the adsorption of the three species decreases with the increase of temperature, while on Carbon 1, the adsorption of SF_6 shows a slightly different behaviour, giving the least adsorption at the lowest temperature of 258 K. This different behaviour of Carbon 1 arises from part of the pore space becoming inaccessible to SF_6 at 258 K because the molecules do not have sufficient energy to overcome the activation energy barrier at the entrance to that part of the pore space.

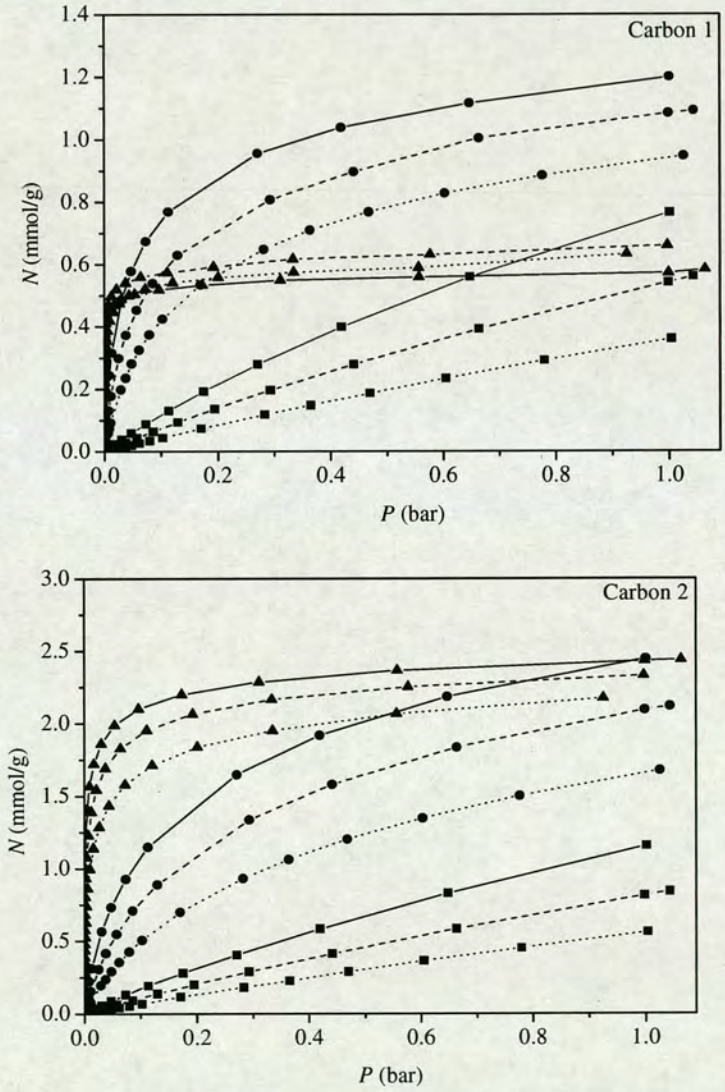

Figure 2.10 Isotherms for adsorption of CH_4 (square), CF_4 (circle) and SF_6 (triangle) on the two carbons at 258 K (solid line), 275 K (dashed line) and 296 K (dotted line).

2.3 Determination of the PNM-PSD

This section shows the determination of PSDs by solving the adsorption integral equation (Eq. 2.1) based on the pore network model. These PSDs are the PNM-PSDs. The single-pore isotherms obtained in Section 2.1 and the experimental isotherms shown in Section 2.2 will be used. The inversion procedure of the adsorption integral Eq. 2.1 to get PSDs has been described in detail by Davies and Seaton.[103] Here we just give a brief description of the procedure. The inversion of Eq. 2.1 will generate single PSDs from the three species (CH_4, CF_4 and SF_6) at different temperatures (258, 275 and 296 K). The overall PSDs are obtained by combining the single PSDs, each of which gives a partial description of the pore structure. The consistency of the overall PSDs is then examined by testing its predictive ability. As indicated in Section 2.2, two VPCs, termed Carbon 1 and Carbon 2, are to be characterized.

2.3.1 Inverting the adsorption integral equation

Inversion of the integral adsorption Eq. 2.1 for PSD calculations is known to be an ill-posed problem. That means that for the same solid, there may be several dissimiliar PSDs that are consistent, to within a small margin of error, with the experimental adsorption on the solid. Inversion methods in previous studies include best-fit methods and matrix methods. The best-fit methods need to assume some distribution functions and vary the parameters to get a satisfactory fit to the experimental data, using a trial-and-error procedure. The matrix methods are free of function assumption. They amount to solving a system of linear equations by matrix inversion, using a regularization procedure to get a fairly good fit to the experimental isotherm.

In this work, a numerical solution strategy, developed by Davies *et al.*[104] is used to obtain the PSD from Eq. 2.1. When written as a matrix equation, Eq. 2.1 becomes the form $\boldsymbol{AX=B}$, where $\boldsymbol{A}$ is a $m \times n$ matrix of single-pore isotherms, $\boldsymbol{B}$ is a vector of the interpolated experimental data points, and $\boldsymbol{X}$ is a pore size distribution vector. A regularisation method is employed to minimize the affect of the ill-posed properties of this equation. This is to incorporate a measure of the smoothness of the PSD into the analysis. The PSD is thus calculated by minimizing the residual R_{Reg}:

$$R_{Reg} = \|AX - B\|^2 + \alpha S \tag{2.23}$$

where α is a strictly nonnegative smoothing parameter, and S is related to the second derivative of the PSD evaluated at some pore width.

Two minimization routines are combined to estimate the optimal value of the smoothing parameter. The L-curve is a plot of a measure of error of fit R_{Reg} against the smoothing factor. Usually, the error remains constant or increases only slightly with α below a threshold value, after which it increases rapidly (the curve thus exhibits a typical L shape). The optimal value of α corresponds to that threshold. The generalized cross-validation (GCV) determines the value of the smoothing factor that results in pore size distributions using N-1 points to predict the Nth point the most successfully. The optimum smoothing factor is the one that allows for the most

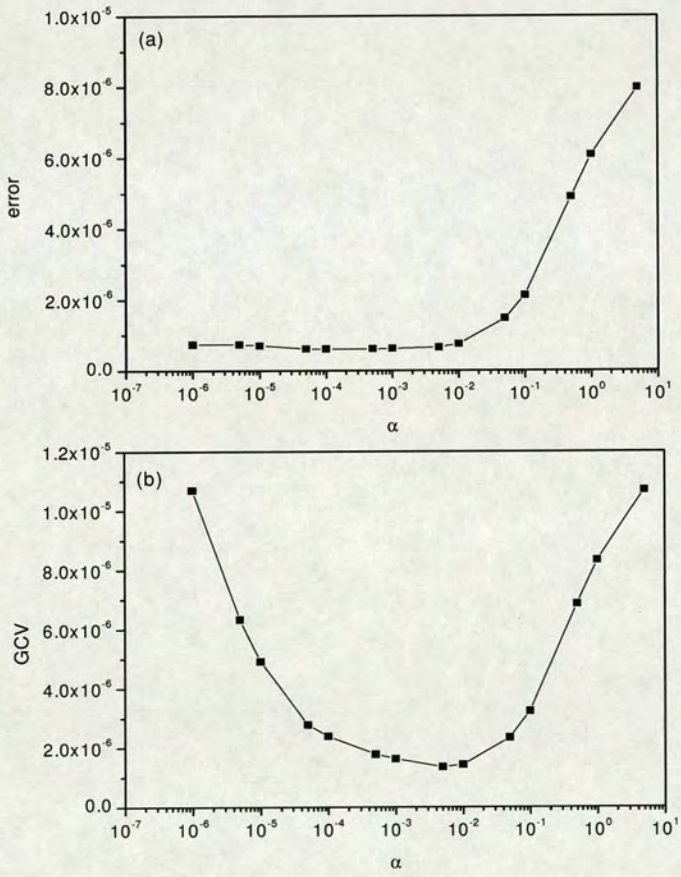

Figure 2.11 L-curve and GCV score for the fit to methane adsorption at 275 K.

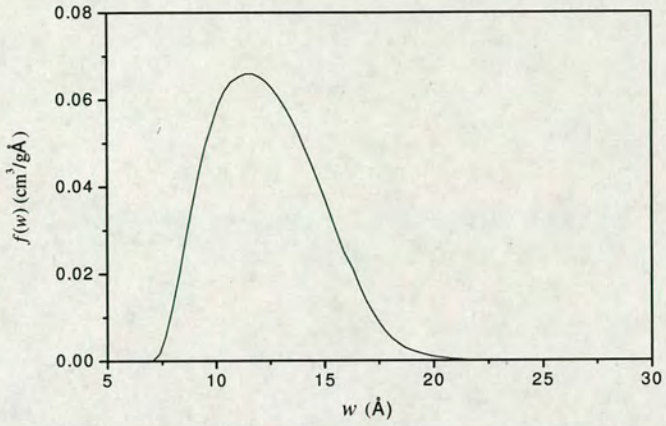

Figure 2.12 The PSD that corresponds to the smoothing factor of 0.01.

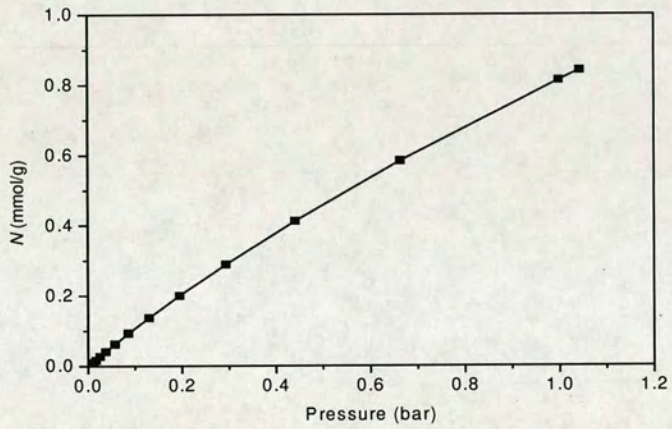

Figure 2.13 Fit of predicted adsorption (line) to the experimental adsorption (symbol) for methane at 275 K.

accurate prediction of all the experimental data points, and thus minimizes the GCV score. Figure 2.11 shows an example of the L-curve and the GCV score for the fit to methane adsorption at 275 K on Carbon 2. From the figure, an optimal smoothing factor of 0.01 is determined. So the PSD that corresponds to this smoothing factor is chosen, which is given in Figure 2.12. The predicted adsorption based on this PSD gives excellent fit to the experimental adsorption, as shown in Figure 2.13. This shows that the choice of the PSD that corresponds to the smoothing factor of 0.01 can give very good prediction of adsorption on the material.

2.3.2 The PNM-PSDs and their consistency for Carbon 1

Nine PNM-PSDs are obtained for Carbon 1. These PSDs are obtained from three species of increasing molecular size – CH_4, CF_4 and SF_6 and at three temperatures – 258 K, 275 K and 296 K. As shown in Figure 2.14, there are differences in the PSDs using the various adsorptives at different temperatures. This may be mainly attributed to the difference in the size and the adsorption energy of the molecules involved. An observation which is worth noting is that SF_6 seems to detect smaller pores (smaller than $w = 8$ Å) than CF_4. This is surprising because from the theoretical point of view, the smaller molecular size of CF_4 should have facilitated its entry into smaller pores. However, since the significant adsorption is from pores wider than $w = 8$ Å for both CF_4 and SF_6, as shown in Figure 2.7 and 2.8, the fitting of the PSD is insensitive to the volume of pores smaller than this size, so this apparent discrepancy is not significant.

Only parts of the PSDs shown in Figure 2.14 are reliable. The reason for this is as follows. Figure 2.6 shows that, in the pressure range studied, the CH_4 single-pore isotherms become linear above about $w = 10$ Å at 258 K and $w = 9$ Å at the two higher temperatures. As the single-pore isotherms become more linear functions of pressure, the contributions of the various isotherms to the amount adsorbed become linearly dependent and these isotherms carry essentially no additional information about adsorption within the pores.[51] As a result, the calculated PSD from Eq. 2.1 in this pore size range is not reliable and so should be discarded. The reliable pore size range defines the "window of reliability" which is bounded on the left by the smallest accessible pore size and on the right by the pore size at which adsorption becomes substantially linear. The reliability of the PSD is improved when a more strongly adsorbing species is used. For example, the CF_4 PSDs are reliable up to $w = 18$ Å at 258 K, $w = 16$ Å at 275 K and $w = 14$ Å at 296 K, given that the adsorption isotherms in bigger pores are linear, as shown in Figure 2.7. Whilst the SF_6 PSDs include pores up to at least $w = 36$ Å, given that the adsorption isotherms in these big pores are not linear, as shown in Figure 2.8. The window of reliability can also be extended to include a bigger pore size range by measuring the isotherm at lower temperatures (so that, in this work, the most reliable information about larger

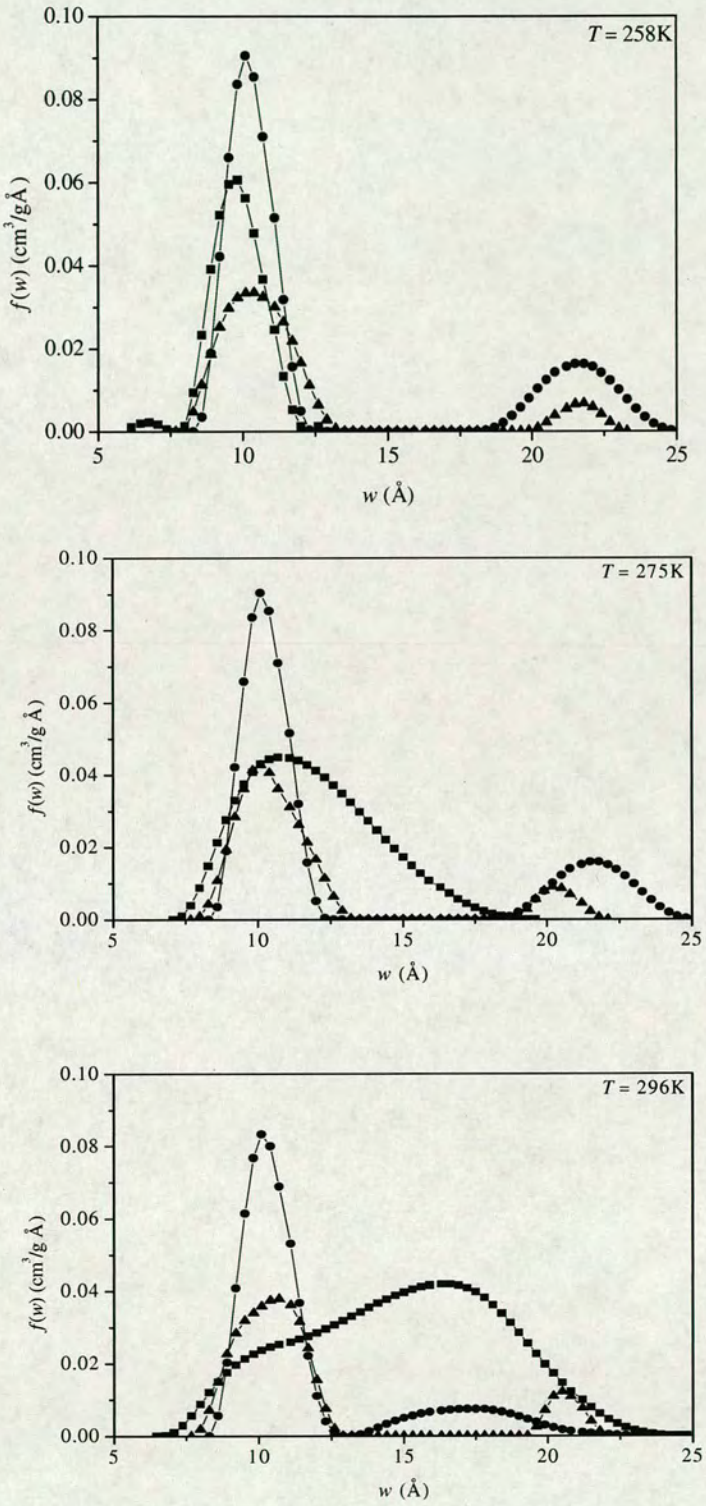

Figure 2.14 Pore size distributions of Carbon 1 obtained using the CH_4 (squares), CF_4 (circles) and SF_6 (triangles) adsorption isotherms.

pores is obtained at 258 K) or extending the measurements to include adsorption at higher pressures.

The window of reliability effect is taken into account in obtaining the overall PSD; *i.e.* only the reliable pore size ranges are used. It is obvious that the small pore size ranges of CH_4 PSDs (up to $w = 10$ Å at 258 K, $w = 9$ Å at 275 and 296 K, as shown in Figure 2.14) should be included. When considering the pore size ranges probed by CF_4 and SF_6, we notice that CF_4 PSDs and SF_6 PSDs substantially overlap; i.e. they have peaks centred at almost the same pore size. The difference between CF_4 PSDs and SF_6 PSDs is that SF_6 PSDs have much smaller peaks, which indicates that SF_6 PSDs capture less pore volume compared with CF_4 PSDs. This arises because some pores that are accessible to CF_4 are not accessible to SF_6 because of the connectivity effect. There are some pores in the network that are not big enough to accommodate SF_6 molecules, and also some pores that are big enough to accommodate SF_6 molecules but shielded by other smaller pores that SF_6 can not go through.

The above observation about CF_4 PSDs and SF_6 PSDs raises the question how to utilize the CF_4 and SF_6 PSDs, together with the CH_4 PSDs, to obtain overall PSDs. The first method proposed is to combine the reliable range of CH_4 PSDs with the "corrected" SF_6 PSDs, where the corrected SF_6 PSDs are obtained by increasing the original SF_6 PSDs in Figure 2.14 by a factor that describes the fraction of pores accessible to CF_4 that are actually accessible to SF_6. The overall PSDs so obtained are called overall PSD-A, for convenience. The second method proposed is to combine the reliable range of CH_4 PSDs with the first peaks of the CF_4 PSDs and the second peaks of the corrected SF_6 PSDs, called overall PSD-B. Figure 2.15 shows the two sets of estimates of the overall PSD, calculated at the three temperatures.

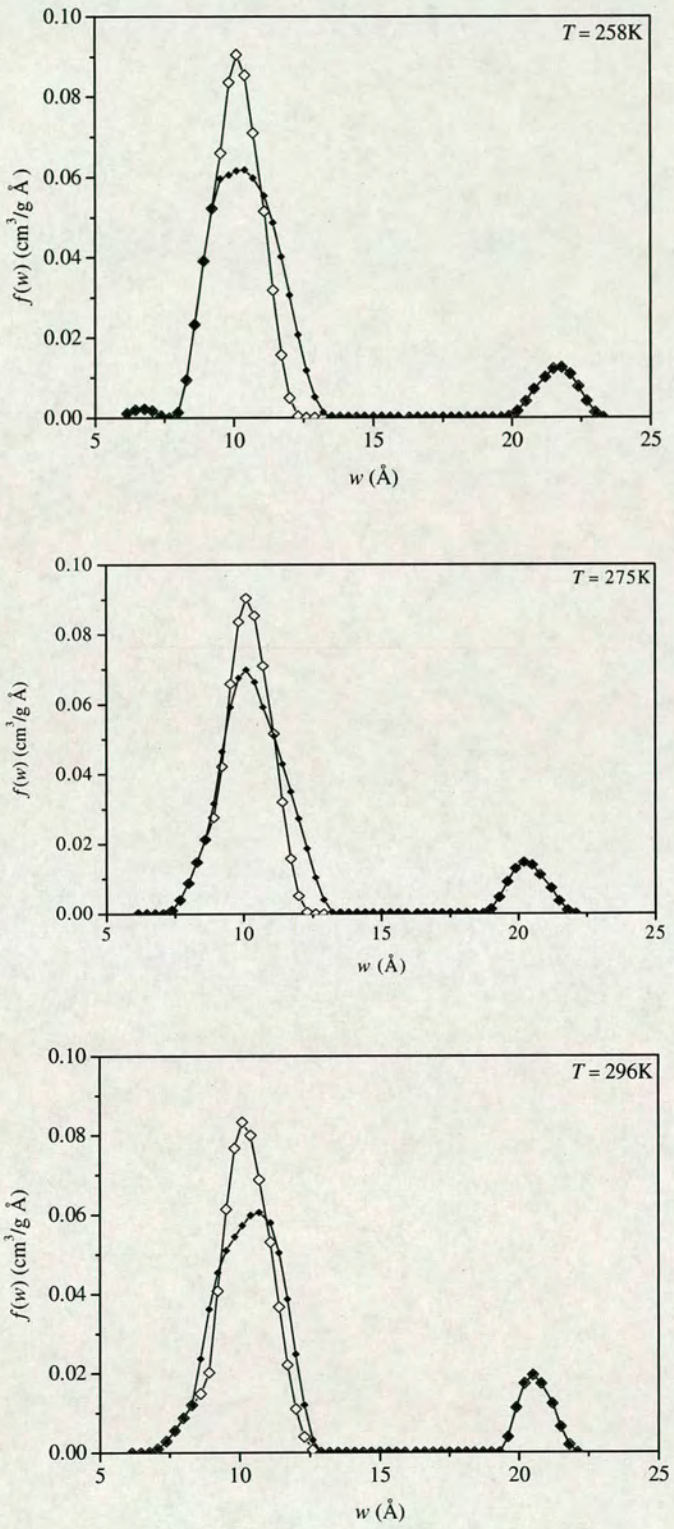

Figure 2.15 Overall pore size distributions of Carbon 1. Closed diamonds indicate PSD-A and open diamonds indicate PSD-B.

So as to assess which of the overall PSDs is best, both overall PSD-A and overall PSD-B have been used to predict the adsorption of the three adsorptive species. It is interesting that although overall PSD-A and overall PSD-B are different in shape, they give similar predictions (lines) that are in good agreement with the "experimental" isotherms (symbols). Figure 2.16 (a) shows an example of such behaviour at 258 K. The similarity between the predicted adsorption by overall PSD-A and overall PSD-B indicates that the two approaches to obtaining an overall PSD are viable. Moreover, it suggests that several "good" PSDs, in terms of their predictive ability, can exist to represent the porous structure of a carbon.

As the two overall PSDs have similar predictive ability, only the predictions from overall PSD-A are fully shown here in Figure 2.16. It is clear that at all the three temperatures the agreement between experimental (symbols) and predicted isotherms (solid lines) for the three adsorptives is very good. Note that solid lines indicate the prediction using the overall PSD at the corresponding temperature. To test the predictive ability of an overall PSD at other temperatures, the overall PSD-A obtained at 258 K is used to predict adsorption at the two higher temperatures – 275 K and 296 K. Again, the predicted isotherms, indicated by dotted lines, are in good agreement with the experimental isotherms for CH_4 and CF_4, while SF_6 is underestimated by about 15%. This under-estimation can be explained, as follows. As shown in Figure 2.10, the "experimental" adsorption of SF_6 at 258 K is less than that at 275 and 296 K, because one more cluster is not accessible to SF_6 at 258 K. This results in missing of some pores when using this isotherm to extract the SF_6 PSD, which leads to under-prediction when using this pore structure information to predict the adsorption of SF_6 at 275 and 296 K. However, the missing of some pores by the SF_6 PSD obtained at 258 K does not lessen the accuracy of the prediction of the adsorption of CH_4 and CF_4 at 275 and 296 K, mainly because these pores have no significant adsorption of CH_4 and CF_4 at these two temperatures and in this pressure range. The above observation suggests that if all the species used to probe the pore structure give more adsorption at lower temperature, as happened on Carbon 2 shown in Figure 2.10, the overall PSD obtained at the lowest temperature would give good predictions for all three species at higher temperatures.

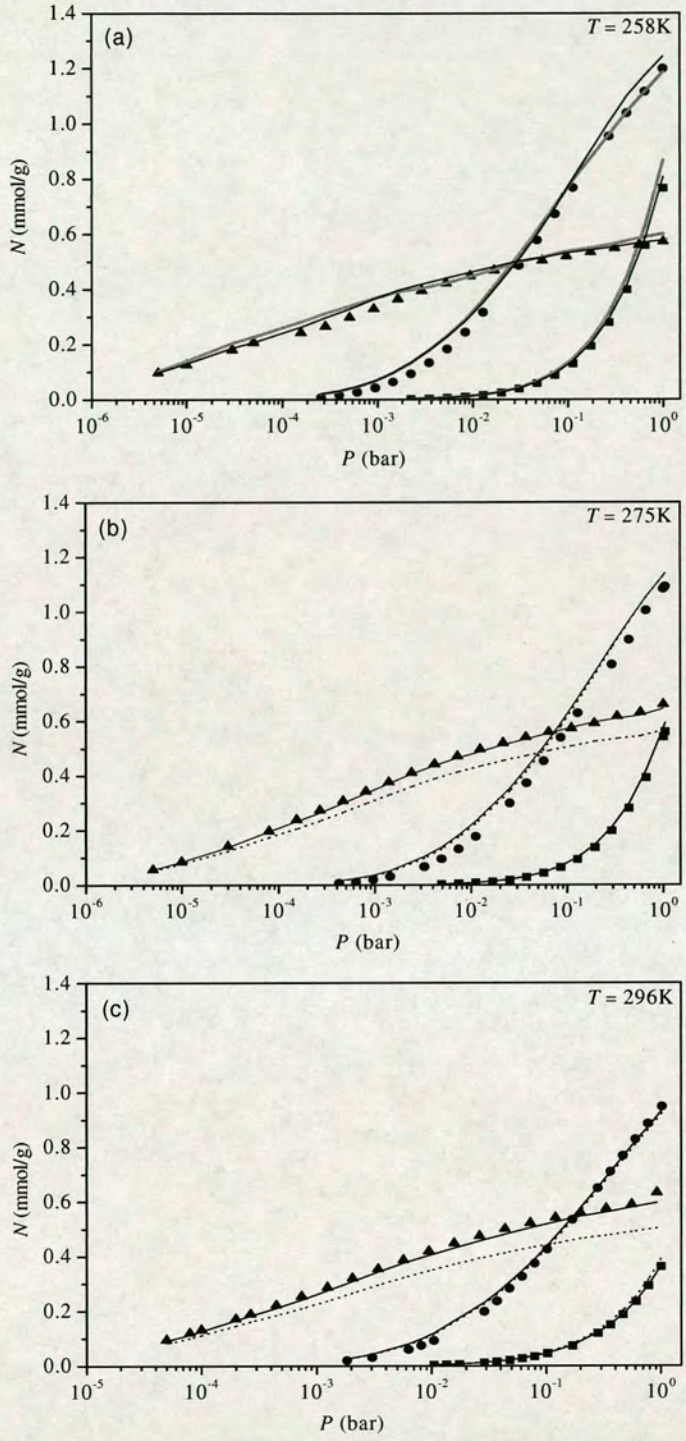

Figure 2.16 Comparison of predicted isotherms (lines) with the "experimental" isotherms for CH_4 (squares), CF_4 (circles) and SF_6 (triangles) on Carbon 1. The solid lines are derived using the overall PSD-A at the corresponding temperatures. The grey lines in (a) are derived using the overall PSD-B at 258K. The dotted lines in (b) and (c) are derived using the overall PSD-A at 258 K.

2.3.3 The PNM-PSDs and their consistency for Carbon 2

The PSDs for Carbon 2, extracted from adsorption of the three species at 258 K, are given in Figure 2.17. Clearly, more pores are accessible to SF_6, compared to Carbon 1 (see Figure 2.14), indicating that the pore network of Carbon 2 presents fewer constrictions narrow enough to limit penetration of this species. The overall PSD (shown in Figure 2.18) is obtained by picking the reliable pore size range of CH_4 PSD (up to 10 Å) and the pore size range of 10.0 – 35.5 Å of the "corrected" SF_6 PSD.

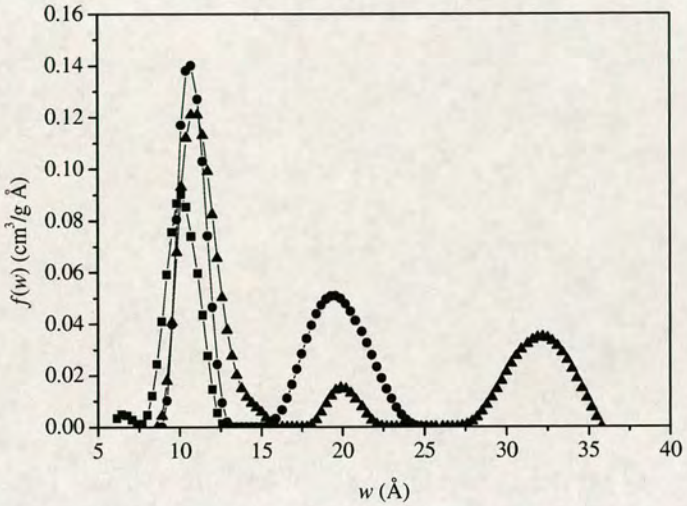

Figure 2.17 Pore size distributions of Carbon 2 obtained using the CH_4 (square), CF_4 (circle) and SF_6 (triangle) adsorption isotherms at 258K.

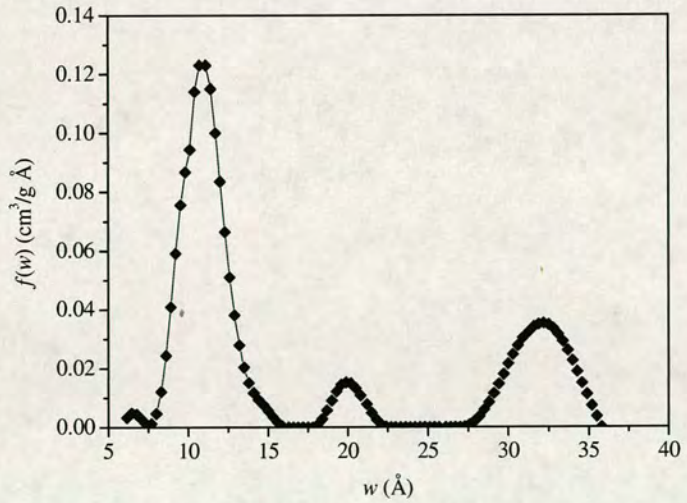

Figure 2.18 The overall PSD of carbon 2 obtained from combining the CH_4 and corrected SF_6 PSDs at 258K.

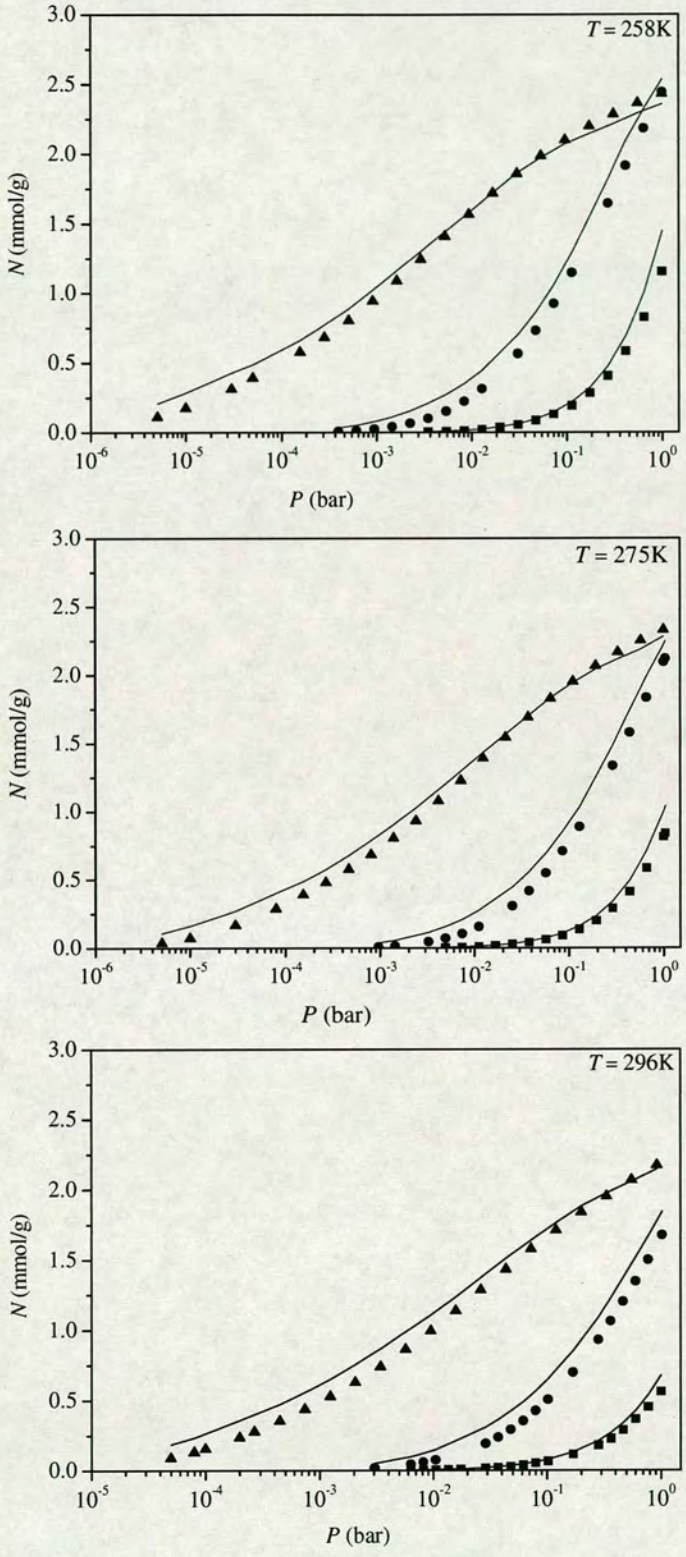

Figure 2.19 Comparison of predicted isotherms (lines) with the "experimental" isotherms for CH_4 (square), CF_4 (circle) and SF_6 (triangle) on Carbon 2.

(The "corrected" SF_6 PSD is almost the same as the original one, as the ratio of pores accessible to CF_4 to the pores accessible to SF_6 is nearly unity.) When this overall PSD is used to predict the adsorption of all the three species at all the three temperatures, excellent agreement between the predicted and the "experimental" isotherms can be seen in Figure 2.19.

The results based on both Carbon 1 and Carbon 2, as discussed above, are very strong evidence that the overall PSDs obtained by combining the partial PSDs from adsorptives of increasing size, are consistent.

2.4 Evaluation of the correctness of the PNM-PSDs

In the previous section (i.e. Section 2.3), PSDs have been obtained based on the pore network model (PNM). Such PSDs, shown in Figure 2.15 for Carbon 1 and Figure 2.18 for Carbon 2, are hereafter denoted by PNM-PSD. To differentiate for the sake of comparison, the PSD obtained from the geometric analysis described in Section 2.2 is denoted by G-PSD. Note that two sets of PNM-PSDs (i.e. overall PSD-A and overall PSD-B, as discussed before) at three temperatures were given in Figure 2.15 for Carbon 1. The one chosen for comparison with G-PSD here is the overall PSD-A at 258 K, as the PSD obtained at lower temperature grasps more accurate information of the porous structure.

Figure 2.20 shows the comparison between PNM-PSD and G-PSD for both Carbon 1 and Carbon 2. It should be noted that the PNM-PSDs shown here are those of Figure 2.15 and 2.18 re-expressed in terms of the "accessible pore size", $w_a = w - 3.4$ Å, as the distance between the surface of the pore surface carbons forms the basis for defining the pore sizes in the geometric analysis; the PSDs have also been normalized using their total pore volumes. This figure shows that the PNM-based analysis positions much of the pore volume at approximately the correct pore sizes for both carbons. There are also, however, some significant discrepancies between the PNM-PSD and G-PSD for both carbons – the PNM-based analysis under-predicts the volume associated with pores whose size falls below $w_a = 5$ Å, especially for

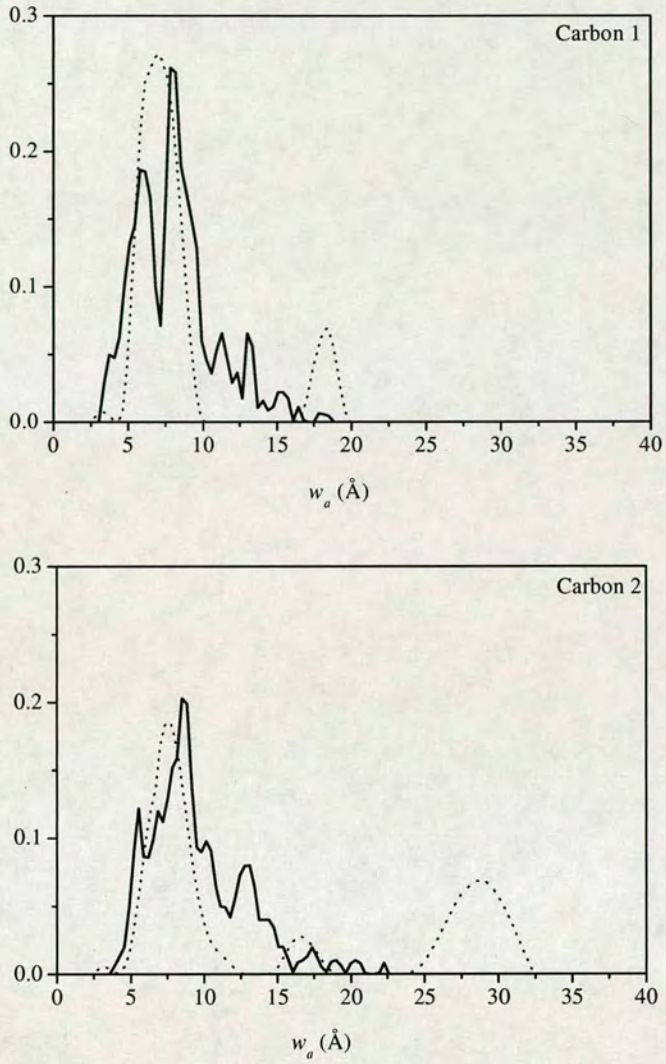

Figure 2.20 Comparison of the overall pore size distribution derived from the PNM-based analysis at 258 K (dashed lines) with that derived from the geometric analysis of the model carbons (solid lines).

Carbon 1, whilst it does not predict at all well the nature of the porosity beyond $w_a \sim 10$ Å, including the inclusion of pore sizes that do not exist and *vice versa*. The appearance of a second, spurious, peak at high pore sizes in the PNM-PSDs is consistent with earlier work on the analysis of adsorption in individual pores using slit-shaped model pores. Davies and Seaton[75] simulated adsorption in pores of rectangular cross-section – simpler than the complex pore network of the model

porous carbons, but nevertheless reflecting the basic rectangular geometry of the individual pores in the model porous carbons. They calculated the PSD of pores with rectangular cross-section, using single-pore isotherms obtained using slit-shaped pores as the kernal of the adsorption integral equation (Eq. 2.1), and found that individual pores of rectangular cross-section generated separate peaks in the PSD, reflecting the fact that the slit-pore-derived PSD interprets adsorption in different regions of a rectangular pore (the corners versus the sides, for example) in terms of slit-shaped pores of different sizes. More generally, the differences between the PNM-PSD and the G-PSD may be understood in terms of local convexity and concavity in the pore space of the VPCs and, by extension, in real carbons. This is illustrated in Figure 2.21. In regions of local convexity, an adsorbate molecule interacts less strongly than it would in a slit pore, so that a narrow, convex element of the pore space is registered as a larger slit pore in the PNM. Similarly, regions of locally concave porosity appear as smaller pores. As a separate effect, thinner, or less dense regions of carbon in the VPC – reducing the strength of the adsorbate-solid interaction relative to Steele's model – will also appear in the PNM-PSD as slightly larger pores. We expect these conclusions to apply to real carbons, so that the PNM is likely to calculate a PSD that is broader than the true PSD of the material.

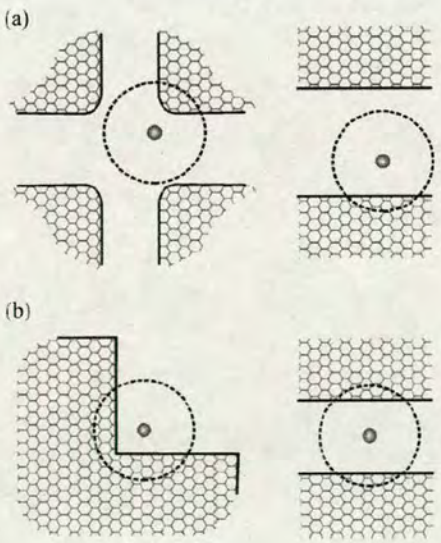

Figure 2.21 Examples of (a) local convexity, represented by a large slit pore; (b) local concavity, represented by a small slit pore. The molecule is shown with its field of substantial interaction with the solid.

2.5 Summary

We have investigated the applicability of the combined GCMC/pore network model, for the characterization of nanoporous carbons. This approach was applied to characterize two virtual porous carbons whose adsorption behavior resembles that of real carbons.

A database of adsorption isotherms of three different gases – CH_4, CF_4, and SF_6 – at three temperatures – 258, 275 and 296K –was obtained by GCMC simulation for a series of slit-shaped pores. PSDs were obtained by comparing these adsorption isotherms with the "experimental" isotherms from the virtual porous carbons, using the adsorption integral equation. A more complete picture of the PSDs (the so called overall PSD) was obtained by combining the partial PSDs probed by the three gases. The predicted adsorption isotherms for the three gases, at the three temperatures, from the overall PSDs, are in good agreement with those generated from the virtual porous carbons. This indicates the predictive power of these overall PSDs when used in a consistent manner, and supports the use of the pore network model (PNM) as a tool for modeling adsorption in real carbons.

Comparison of the overall PSD derived from the adsorption-based analysis using the PNM with those obtained from the geometric analysis of the virtual porous carbons shows that whilst the distribution of the volume associated with pores of accessible width below $w_a = 10$ Å is reasonably well predicted, there are significant discrepancies for larger pores, including omission of pore sizes that are known to exist and *vice versa*. These discrepancies are caused by differences in the pore walls (*e.g.* low density, thinner), or what we have termed locally convex or locally concave porosity. The comparison between the PSD using the PNM with the true structure of the model carbon demonstrates the fundamental limitations of using the PNM, with its assumptions of pores of constant cross section, and pore intersections of negligible volume, to describe a real carbon.

3. Determination of the Pore Network Connectivity of Nanoporous Carbons

As discussed in Chapter 1, the mean coordination number $\overline{Z}$ is used to characterize the pore network connectivity of a porous medium. For a regular pore structure, such as cubic arrays of spheres, it is easy to determine $\overline{Z}$ ($\overline{Z}$ = 6), as the coordination number is the same at all the junctions, whereas estimating $\overline{Z}$ for an irregular pore space (for example, in the case of nanoporous carbons) is usually difficult and often ambiguous as the coordination number varies from junction to junction. Fortunately, percolation theory has given a big hand to enable us to estimate the average coordination number $\overline{Z}$, by analyzing physical adsorption (and desorption) data. Jerauld *et al.*[79] showed that, as long as the mean coordination number of the topologically-disordered network is equal to that of a regular network, the effective properties (for example, the effective diffusivity to be determined in Chapter 5) of the two systems are, for all practical purposes, identical. Therefore, if we map the disordered network of a real material (or a realistic model of a real material) to a regular network with the same mean coordination number $\overline{Z}$, the effective properties of the disordered network can be more easily studied.

In principle, any porous medium can be mapped onto an equivalent network of bonds connected to each other at nodes of the network; the pore bodies are represented by network bonds and the pore junctions are represented by network nodes. Figure 3.1 gives an example how an irregular network of a real carbon is mapped to a regular network of simple-cubic lattice, in a two-dimensional picture. The sizes of the pores are assigned to the bonds so that the real structure and the lattice model have the same pore size distribution, and the mean coordination number of the lattice model is set to the mean coordination number of the real solid by eliminating bonds from a regular lattice (i.e. a simple cubic lattice) of higher connectivity until the right mean coordination number is obtained. The use of regular lattices to represent irregular networks enables us to study the properties of nanoporous carbons by applying percolation theory that is based on the regular networks.

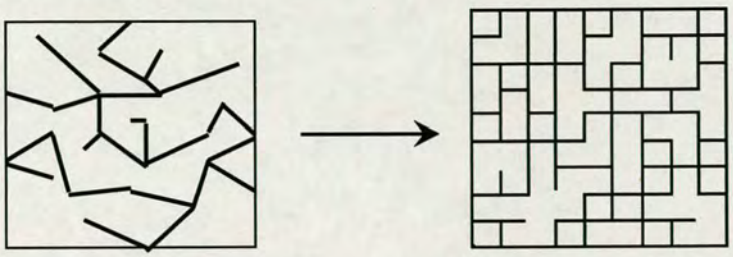

Network of real solids Network of lattice

Figure 3.1 Mapping of the pore network of a real carbon to a lattice

In this chapter, the pore network connectivity of the two virtual porous carbons – Carbon 1 and Carbon 2, in terms of the mean coordination number, $\overline{Z}$, is determined using percolation theory. An introduction to percolation theory is given in Section 3.1. The application of percolation theory for obtaining the mean coordination number of porous media is given in Section 3.2. The results are presented in Section 3.3.

3.1 Introduction to Percolation Theory

Percolation tells us when a system is macroscopically open to a given phenomenon. For example, it can tell us when one can have current flow from one side of an electric network to the opposite side, how much oil one can extract from an oil reservoir, and how long a forest fire takes to either penetrate the forest or to be extinguished (an interesting example given in Stauffer's book[160]). The point at which the percolation transition between a connected system and a disconnected one takes place for the first time is the percolation threshold, p_c, of the system. The behaviour of the system close to p_c is of prime interest and importance, because the properties of the system change dramatically near p_c. As we will see later, the connectivity of the two carbons studied in this work is close to the percolation threshold.

Percolation theory, which describes the physical model of percolation, has been used in many research areas, from geology, chemistry, physics, and materials science to engineering. Some examples of how percolation theory is applied in research areas

such as (1) characterizing porous media, (2) studying flow and transport in porous media and fractured rocks, (3) studying hydrodynamic dispersion and groundwater flow in rock, (4) predicting mechanical, rheological, and structural properties of branched polymers and gels, and (5) predicting the effective properties of composite materials can be found in Sahimi's book.[161] Here we just concentrate on how percolation theory is used to obtain the mean coordination number of porous media.

Percolation was first studied on regular networks such as the two-dimensional honeycomb lattice and square lattice, and the three-dimensional simple cubic lattice, body-centred cubic lattice and face-centred cubic lattice.[160] Two kinds of percolation problems, i.e., the bond percolation problem and the site percolation problem (in this thesis refers to sites as "nodes" where pores meet) are defined according to whether we assign the property of interest to the bonds or the nodes of the network. In the simple cubic lattice which the disordered pore network of nanoporous carbons is mapped to, the bonds represent pores and the nodes represent junctions. We are interested in the bond percolation problem as pores are of the primary interest in studying properties of nanoporous carbons. In the bond percolation problem, the bonds of the network are either occupied (i.e. they are open to flow, diffusion and reaction) randomly and independently of each other with probability p, or are vacant (i.e. they are closed to flow or current) with probability $1-p$. For a large network, this assignment is equivalent to removing a fraction $1-p$ of all bonds at random. Two nodes are called connected if there exists at least one path between them consisting solely of occupied bonds. A set of connected nodes bounded by vacant bonds is called a cluster. If the network is of very large extent and if p is sufficiently small, the size of any connected cluster is small. But if p is close to 1, the network should be entirely connected, apart from occasional small gaps in the network. At some well-defined value of p, there is a transition in the topological structure of the random network from a macroscopically disconnected structure to a connected one; this value is called the bond percolation threshold, p_c. This is the largest fraction of occupied bonds below which there is no sample-spanning cluster of occupied bonds.

The percolation threshold of a network can be calculated numerically by Monte Carlo simulation. Both Stauffer[160] and Sahimi[161] summarized in their books the percolation thresholds of some regular networks. Table 3.1 shows the percolation thresholds of some 3D regular networks. A significant feature thus has been found that the product Zp_c is essentially an invariant of percolation networks, as shown in Table 3.1.

Table 3.1 Precolation thresholds for some 3D networks

Network	Z	p_c	Zp_c
Diamond	4	0.389	1.55
Simple cubic	6	0.249	1.49
Body-centred cubic	8	0.179	1.44
Face-centred cubic	12	0.198	1.43

In addition to the percolation threshold p_c, the topological properties of percolation networks are characterized by several important quantities. Here we just give the quantities to be used in this work.

i) Bond occupation probability p. This is the probability that, the bonds in the lattice are occupied.

ii) Accessibility A. This is the probability that, when the fraction of occupied bonds is p, a given bond belongs to the infinite (sample-spanning) cluster of occupied bonds.

A is a function of p. For a simple cubic lattice, the relation between A and p can be found by carrying out Monte Carlo simulation on the lattice, which is given in Figure 3.2. Simply, the relation between A and p can be expressed as $A = f(p)$. Based on this, the relation between ZA and Zp, i.e. $ZA = f(Zp)$, can be found, making use of Zp_c as an invariant of percolation networks. Section 3.2 will show how this relation is used to determine the mean coordination number $\overline{Z}$ of porous media.

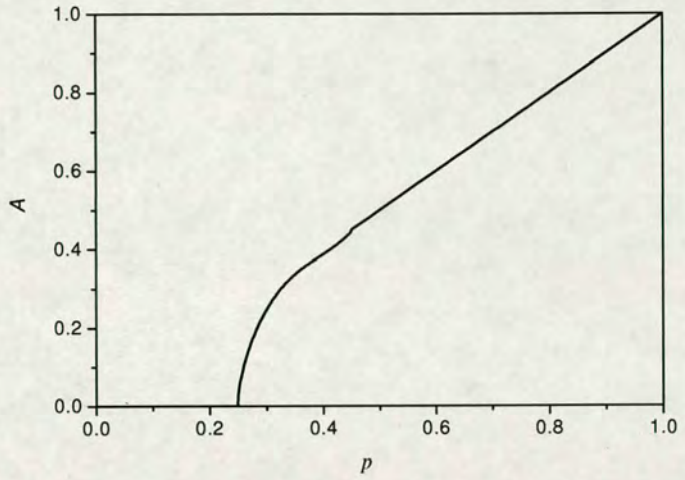

Figure 3.2 Accessibility A as a function of bond occupation probability p.

3.2 Application of Percolation Theory to Characterize Porous Media

Seaton[52] proposed an analysis method, based on percolation theory, that allows a measure of the mean coordination number, $\overline{Z}$, of the pore network, to be determined from nitrogen adsorption-desorption isotherms. This method is for the measurement of the connectivity of mesoporous solids as it is dependent on the adsorption-desorption hysteresis loop which is the characteristic of mesoporous solids. Seaton and coworkers[54] later developed the previous idea to provide an approach for determining the mean coordination number of the pore network for microporous solids. We use their approach here to characterize our virtual porous carbons that contain mainly micropores, like most real porous carbons.

This approach makes use of the feature that for a specific probe species in a given pore network, some big pores are connected only by smaller impenetrable pores and are thus not accessible to the probe molecules. This feature is illustrated in Figure 3.3. For example, in this depicted pore network, we can see that some pores (e.g. pore 1) are too small to let either CH_4 or SF_6 in; some pores (e.g. pore 2) are big enough to accommodate both CH_4 and SF_6; some pores (e.g. pore 3) are able to let CH_4 in but not big enough to accommodate SF_6; some pores (e.g. pore 4), though big

enough to accommodate SF_6, are shielded by smaller pores and only accessible to CH_4. Comparing with CH_4, SF_6 probes less pore volume. If we choose SF_6 as the probe species, two variables regarding this phenomenon arise: the fraction of pores in a network that are large enough to accommodate the probe species (the "bond occupation probability" p) and the fraction of pores that are actually accessible to this adsorptive (the "accessibility" A). The deviation of A from p reflects the finite connectivity of the pore network, which can be analyzed using percolation theory.

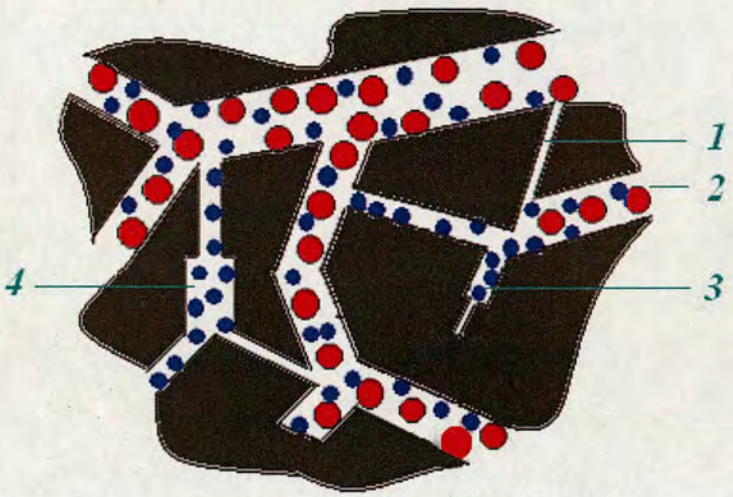

Figure 3.3. Schematic illustration of the pore network accessibility. The blue and red circles represent small molecules (CH_4 here) and bigger molecules (SF_6 here) respectively. "1" indicates pores which are too small to let either CH_4 or SF_6 in; "2" indicates pores in which both CH_4 and SF_6 can reside; "3" indicates pores that are not able to accommodate SF_6 but able to let CH_4 in; "4" indicates pores which are big enough to accommodate SF_6 but shielded by smaller pores and accessible to CH_4.

In this approach, the pore network connectivity is determined based on the PSDs obtained using adsorptives of increasing size. Three adsorptives – CH_4, CF_4 and SF_6 – are used to probe the pore structure. An overall PSD is obtained by combining the partial information obtained using the different adsorptives, as described in Chapter 2. By comparing the PSD derived from the adsorption isotherm of an adsorptive (for example, SF_6) against the overall PSD, an estimate of the connectivity of the pore network, i.e. the mean coordination number, $\overline{Z}$, can be extracted using percolation theory.

In this work, we chose SF_6 as the probe species to obtain an estimate of the mean coordination number of the pore network. The SF_6 PSD and the overall PSD are given in Figure 2.14 and 2.15 for Carbon 1 and in Figure 2.17 and 2.18 for Carbon 2. For the convenience of analysis, the SF_6 PSD is denoted by $f_s(w)$ and the overall PSD is denoted by $f_0(w)$. The pore size distribution is formally defined as:

$$f(w) = \frac{dV}{dw} \tag{3.1}$$

Since percolation theory deals with the number of pores of different sizes, we transform the PSD, $f(w)$, which is in terms of pore volume, to the function $n(w)$, which is in terms of the number of pores. Assuming that the length and breadth of the pores are uncorrelated with their width:

$$n_0(w) = \frac{f_0(w)}{w} \tag{3.2}$$

$$n_s(w) = \frac{f_s(w)}{w} \tag{3.3}$$

where $n_0(w)$ contains all the pores that are big enough to accommodate SF_6 and some smaller pores, $n_s(w)$ contains the pores that are actually accessible to SF_6.

The fraction of pores in the network that are large enough to accommodate SF_6, i.e. the bond occupation probability p, is the normalized integral of $n_0(w)$ over the range of pore sizes that are large enough to accommodate the probe molecule:

$$p = \frac{\int_{w^*}^{\infty} n_0(w)dw}{\int_{0}^{\infty} n_0(w)dw} \tag{3.4}$$

where w^* is the width of the smallest pores that can accommodate SF_6.

The fraction of pores that are actually accessible to SF_6, i.e. the accessibility A, is the normalized integral of $n_s(w)$ over the same range of pore sizes.

$$A = \frac{\int_{w^*}^{\infty} n_s(w)dw}{\int_{0}^{\infty} n_0(w)dw} \tag{3.5}$$

The relation between A and p was obtained by carrying out Monte Carlo simulations of percolation on the simple cubic lattice in a simple expression by Zhang and Seaton.[162] They use the results which are close to those for an infinite network, to represent the local percolation behaviour. The simulation results are correlated, making use of the accepted value of the percolation threshold for the undiluted simple-cubic lattice[160], p_c = 0.249, and the known scaling behaviour of the accessibility near the percolation threshold, $A \sim (p - p_c)^{0.41}$, as follows.

$$\begin{aligned} A &= 0 && p < 0.249 \\ A &= 0.4567(p-0.249)^{0.41} + 3.153(p-0.249) - 20.88(p-0.249)^2 + 51.58(p-0.249)^3 && 0.249 < p < 0.45 \\ A &= p && 0.45 < p \end{aligned} \tag{3.6}$$

Dimensional invariance implies that the number of accessible pores per pore intersection, $\overline{Z}A$, is a general function of the number of "occupied" pores (i.e. pores large enough to accommodate the probe molecule) per intersection, $\overline{Z}p$. Eq. 3.6 can be generalized to represent a network of arbitrary $\overline{Z}$ by replacing p by $\overline{Z}p/6$ and A by $\overline{Z}A/6$ to give the following function:[54]

$$\begin{aligned} \overline{Z}A &= 0 && \overline{Z}p < 1.494 \\ \overline{Z}A &= 1.314(\overline{Z}p-1.494)^{0.41} + 3.153(\overline{Z}p-1.494) - 3.480(\overline{Z}p-1.494)^2 + 1.433(\overline{Z}-1.494)^3 && 1.494 < \overline{Z}p < 2.7 \\ \overline{Z}A &= \overline{Z}p, && 2.7 < \overline{Z}p \end{aligned} \tag{3.7}$$

The value of $\overline{Z}$ for the virtual porous carbon is estimated by fitting the (p, A) values calculated from Eq. 3.4 and 3.5 to Eq. 3.7 at each temperature.

3.3 The Pore Network Connectivity of the two Carbons

The pore network connectivity, in terms of the mean coordination number, $\overline{Z}$, was obtained for the two virtual porous carbons – Carbon 1 and Carbon 2, using the approach given in Section 3.2. The bond probability p and the accessibility A are shown in Table 3.2. Figure 3.4 gives an example to show how the (p, A) is fitted to Eq. 3.7 to estimate $\overline{Z}$. The solid line is the plot of Eq. 3.7 and the dotted line gives the relation between p and A. The cross point gives the value ($\overline{Z}p, \overline{Z}A$). Thus $\overline{Z}$ is calculated as p and A are known.

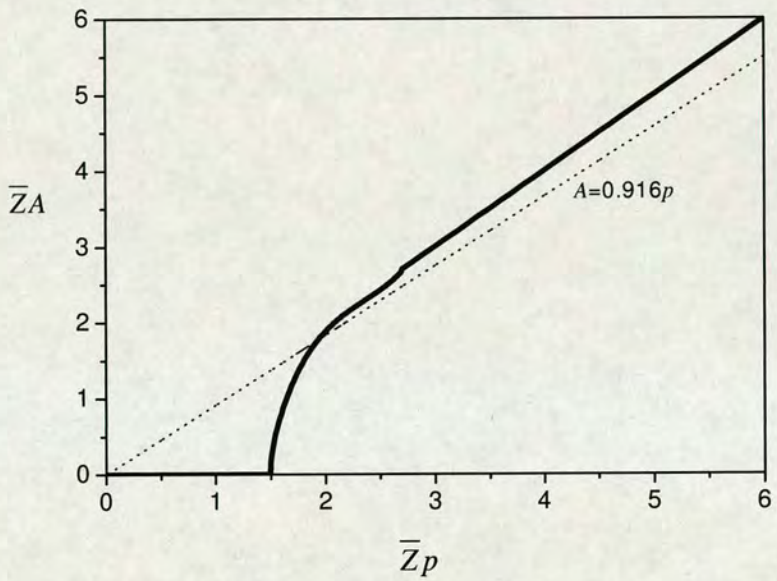

Figure 3.4 Showing how the (p, A) is fitted to Eq. 3.7 to estimate $\overline{Z}$.

The mean coordination numbers of both Carbon 1 and Carbon 2 are shown in Table 3.2. The values of p for Carbon 1 are quite close to those for Carbon 2, while the values of A for Carbon 1 are much smaller than that for Carbon 2. This indicates that the two carbons have very similar factions of pores big enough to accommodate SF_6 molecules, but because of the connectivity effect, more pores are inaccessible to SF_6 in Carbon 1. This is in agreement with the observation made in Chapter 2, that Carbon 2 has a higher accessibility. For Carbon 1, the values of $\overline{Z}$ at different temperatures are very consistent, at around 1.7. The mean coordination number for Carbon 2 is slightly higher, at 2.1. Note that the function $A(p)$ is very steep just above

the percolation threshold, so that a small change in p can give a big change in A. In the context of application, for example, diffusion in the pore network, this feature indicates that a little change in the probability of occupied bonds will result in a big change in the properties we are interested in (i.e. effective diffusivity). This will be shown in Chapter 5.

Table 3.2 Values of p, A and $\overline{Z}$ obtained at the three temperatures.

Carbon 1			
Temperature(K)	***p***	***A***	$\overline{Z}$
258	0.983	0.521	1.65
275	0.982	0.584	1.67
296	0.972	0.605	1.70
Carbon 2			
258	0.935	0.856	2.06

Some remarks need to be made considering the connectivity information obtained here. Firstly, at the most basic level, the approach measures the accessibility of the pore network to molecules below a certain size, i.e. the smallest pores that the smallest adsorptive used can probe. In heterogeneous materials such as nanoporous carbons, the pores are connected randomly and the probe molecules will only penetrate and fill those pores that are connected through pores larger than the size of the probe molecule. Secondly, the mean coordination numbers reported in Table 3.2 are averages over values with a wide variation in the local coordination number; some nodes are connected to three or more pores, while others are at the end of dead-end pores, as illustrated in Figure 3.3. This method provides no information about the distribution of coordination numbers within the pore network. Thirdly, the estimation of $\overline{Z}$ in this method involves the calculation of p and A, which in turn depends on the adsorptives used (and the particular way they interact with the material) and the process for obtaining the PSD. Instead of using partial PSDs of three gases to build up an overall PSD, Ismadji and Bhatia[120] obtained the overall PSD from argon

adsorption data and then compared the PSD from the adsorption of esters with the overall PSD to estimate the connectivity. The mean coordination numbers they obtained for real carbons were 2.97 and 4.0. Navarro *et al.*[121] obtained the overall PSD from nitrogen adsorption data at 77 K and then compared the PSD from the adsorption of ethane at 264 K with the overall PSD to yield the mean coordination numbers around 2.0 for several carbons. The mean coordination numbers we obtained in this work for the VPCs are very close to the "experimental" values for real carbons.

3.4 Summary

In this chapter, the mean coordination number $\overline{Z}$, which is a useful measure of the connectivity of the disordered pore network of nanoporous carbons, was determined based on the PSDs obtained using adsorptives of increasing size – CH_4, CF_4 and SF_6, with the aid of percolation theory. The estimate of $\overline{Z}$ was obtained by comparing the PSD obtained from the adsorption of SF_6 with the overall PSD obtained by combining those of the three adsorptives. We see good agreement between the values of $\overline{Z}$ determined at different temperatures, supporting the consistency of this approach. The mean coordination numbers for the two different carbons show the difference between them, i.e. Carbon 1 has lower accessibility than Carbon 2, which is in agreement with the evidence from the adsorption isotherms in Figure 2.10 that adsorption of SF_6 is much less in Carbon 1 than that in Carbon 2.

It is worth noting that we were also trying to evaluate the correctness of the mean coordination number $\overline{Z}$ obtained from this approach, by comparing $\overline{Z}$ from this approach with that from the geometric analysis of the virtual porous carbons. The idea is similar to the evaluation of the correctness of a PSD, as discussed in Chapter 2. However, we failed to do so because the geometric analysis of the VPC is unable to provide a well-defined $\overline{Z}$. The difficulty comes from the fact that in the pore space of real or virtual porous carbons, it is ambiguous what should be defined as a "pore" and what should be defined as a "junction". So the correctness of $\overline{Z}$ can not

be evaluated in a purely geometrical term. Later in Chapter 5, we will evaluate the correctness of $\overline{Z}$ obtained in this chapter, by relating to the process of predicting the effective diffusivity. In this sense, the correctness of the effective diffusivity predicted by making use of $\overline{Z}$ can be used to indicate the correctness of $\overline{Z}$.

4. Molecular Dynamics Simulation of Diffusion in Carbon Nanopores

In this chapter, the database of single-pore transport diffusivities in a series of individual pores will be constructed, as the input to the pore network model (which is built with the PSD obtained in Chapter 2 and the connectivity obtained in Chapter 3) for calculating the effective diffusivity in Chapter 5. Meanwhile, the influence of different wall conditions, namely a smooth wall, an atomic wall and a diffuse wall, on self-diffusion and macroscopic transport will be systematically investigated using MD simulations. As discussed in Chapter 1, the assumed pore wall surface has big effects on dynamic properties of the fluid confined in the pore, and diffusivities governing self-diffusion and transport diffusion are fundamentally different quantities. The study of the effects of the assumed pore wall surface on self-diffusion and transport diffusion will help us choose the "right" surface models for obtaining reliable diffusivities.

The chapter begins with the fundamental difference between self-diffusion and transport diffusion in porous media, given in Section 4.1. As MD simulation is the vital tool to study diffusion in porous materials, Section 4.2 will give a detailed description of the MD simulation method and involved techniques in this work. Section 4.3 and 4.4 will compare self-diffusion coefficients and transport diffusion coefficients from the three wall conditions. The influence of the assumed pore wall surfaces on self-diffusion and transport diffusion will be discussed, and the single-pore diffusivities for the input to be used in Chapter 5 will be shown.

4.1 Fundamentals of Diffusion

Two different diffusion phenomena may be distinguished: self-diffusion, which reflects the Brownian motions of molecules in an equilibrium system, and transport diffusion, which is driven by a chemical potential gradient in a non-equilibrium system. The diffusion coefficients governing self-diffusion and transport diffusion in porous materials are fundamentally different quantities.[17]

4.1.1 Self-diffusion

In an equilibrium system with N molecules at temperature T, all the molecules are in a state of motion with velocities that are consistent with the Maxwell-Boltzmann distribution at that temperature. If we follow the trajectory of an individual molecule in this system it may appear as though the molecule is performing a random walk in space. The self-diffusion coefficient D_s is defined by the mean square displacement (MSD) via Einstein's equation:

$$D_s = \frac{1}{2d_0 t} \lim_{t \to \infty} \left\langle \frac{1}{N} \sum_{i=1}^{N} [\boldsymbol{r}_i(t) - \boldsymbol{r}_i(0)]^2 \right\rangle \tag{4.1}$$

where $\boldsymbol{r}_i(t)$ and $\boldsymbol{r}_i(0)$ are the vectors describing the positions of molecule i at time t and time 0, d_0 is the dimension of the system ($d_0 = 1$ for cylindrical pores, $d_0 = 2$ for slit pores and $d_0 = 3$ for bulk phase). The average is taken over time for the mean square displacement of all the molecules.

The self-diffusion coefficient can also be calculated by measuring the velocity autocorrelation of a molecule during its movement, via the following relation:

$$D_s = \frac{1}{d_0 t} \int_0^{\infty} dt \left\langle \frac{1}{N} \sum_{i=1}^{N} \boldsymbol{v}_i(t) \bullet \boldsymbol{v}_i(0) \right\rangle \tag{4.2}$$

where $\boldsymbol{v}_i(t)$ and $\boldsymbol{v}_i(0)$ are the vectors describing the velocities of molecule i at time t and time 0.

4.1.2 Transport diffusion

In a non-equilibrium system with N molecules at temperature T, a macroscopic flux forms along the direction of the concentration gradient. Fick's law of diffusion states that the flux is linearly proportional to the concentration gradient $\nabla \boldsymbol{c}$.

$$\boldsymbol{J} = -D_t \nabla \boldsymbol{c} \tag{4.3}$$

$\boldsymbol{J}$ is the macroscopic flux, expressed as the mean number of molecules flowing per unit cross-sectional area of the nanoporous material due to a concentration gradient,

and D_t is the transport (Fickian) diffusion coefficient, which in general is a function of concentration.

The definition of the diffusivity according to Eq. 4.3 carries the implication that the driving force for transport diffusion is the gradient of concentration. However, since transport diffusion is simply the macroscopic manifestation of the tendency to approach equilibrium, it is clear that the true driving force must be the gradient of chemical potential μ. Considering the chemical potential gradients as the fundamental driving forces for transport diffusion in porous materials, the flux can be related to an Onsager coefficient L:

$$\boldsymbol{J} = -L\nabla\mu \tag{4.4}$$

L is a coefficient that can be calculated from MD simulations. The transport diffusion coefficient defined in Eq. 4.3, D_t, is then related to L by:

$$D_t = L\frac{RT}{c}\frac{d\ln f}{d\ln c} \tag{4.5}$$

where R is gas constant, c is the density of the confined fluid in the pore, f is the fugacity. $d\ln f / d\ln c$ represents simply the gradient of the equilibrium adsorption isotherm in logarithmic coordinates, which is called the thermodynamic correction factor. This factor may vary substantially with density, depending on the relation between f and c. At very low density, the density of the adsorptive in porous materials is directly proportional to the fugacity (pressure) of the adsorptive in equilibrium with the bulk, which satisfies Henry's law (i.e. $c = Hf$, where H is a constant). $d\ln f / d\ln c$ can be calculated from the adsorption isotherm and approaches a constant value of 1.0 at low density within the Henry's Law region.

Eq. 4.5 can also be expressed as

$$D_t = D_c\frac{d\ln f}{d\ln c} \tag{4.6}$$

D_c, defined in this way, is generally referred to as the "corrected diffusivity", although D_t is actually the diffusion coefficient that we need to describe the transport diffusion process.

As explained before, in a dilute (i.e. low density) system, the thermodynamic correction factor $d\ln f / d\ln c$ approaches 1.0. From Eq. 4.6, an approximation is thus made to the relationship between the corrected and transport diffusivities, giving $\lim_{c\to 0} D_c = \lim_{c\to 0} D_t$. On the other hand, as adsorbate loading tends to infinite dilution, the interactions between the diffusing molecules are negligible. In this limit, transport diffusivity is equal to self-diffusivity, i.e. $\lim_{c\to 0} D_t = \lim_{c\to 0} D_s$.[16] The above observation is generalized:

$$\lim_{c\to 0} D_c = \lim_{c\to 0} D_t = \lim_{c\to 0} D_s \tag{4.7}$$

Many researchers made use of Eq. 4.7, to calculate transport diffusion coefficient from self-diffusion coefficient. Assuming that $D_s(c) = D_s(0)$, the so called Darken's equation gives:[17]

$$D_t \cong D_s \frac{d\ln f}{d\ln c} \tag{4.8}$$

Actually many real systems are far from dilute density. In such systems, transport, corrected, and self-diffusivities are all dependent on the density of the adsorbed species and are only equal in the limit of dilute density. Recently Darken's equation has been shown to give inaccurate transport diffusivity at high loadings.[28] Moreover, as we will show later in Section 4.3 and 4.4, the values of self-diffusion coefficients and transport diffusion coefficients rely on the surface models in different ways. D_t should not be related to D_s in such a simple way by Eq. 4.8.

4.2 Molecular Dynamics Simulation

Molecular dynamics (MD) simulations provide a deep understanding of the mechanisms of self-diffusion and transport diffusion through porous materials. MD simulations are in many respects very similar to real experiments. When we perform a real experiment, we proceed as follows. We prepare a sample of the material that we wish to study. We connect this sample to a measuring instrument, and we measure the property of interest (here self-diffusion coefficient and transport diffusion coefficient) during a certain time interval. If our measurements are subject to statistical noise, then the longer we average, the more accurate our measurement becomes. An experimental measurement of diffusion is often under isothermal conditions. In an MD simulation, we follow exactly the same approach. First, we prepare a sample: we select a model system consisting of N molecules and keep this system at the desired temperature. Second, we solve Newton's equations of motion for this system until the properties of the system no longer change with time. After equilibration, we perform the actual measurement. The MD simulations carried out in this work are to sample the canonical ensemble where the number of molecules, N, the volume of the system, V, and temperature T, are constant. The pieces of the recipe of a MD simulation are given in the following sections.

4.2.1 Pore models

As the slit pore model is a simple and good representative of the pores of nanoporous carbons, it was used to study adsorption in nanoporous carbons in Chapter 2. To be consistent, this slit pore model is also used here to study diffusion. The slit pores are defined by the basal surfaces of two opposing semi-infinite blocks of graphite – and are hence termed here basal plane slit pores – and the width, w, is defined as the distance between the centre of the surface carbon atoms of the opposing pore walls. It has been found that dynamic properties (for example, diffusion) depend considerably on the surface of the confining walls of the slit pores and how the fluid molecules interact with the walls.[122, 123, 125, 126] Therefore, three wall conditions, namely the smooth wall, the atomic wall and the diffuse wall, are considered here to examine the influence of the assumed pore surface on diffusion.

In a pore with smooth walls, the carbon atoms on all the graphite planes are smeared out. In a pore with atomic walls, the graphite planes that are directly in contact with the fluid molecules are constructed by presenting all the carbon atoms. Each graphite plane has a size of 100Å×100Å in the x and y directions and contains 3772 carbon atoms. Periodic boundary conditions are applied in the x and y directions. Figure 4.1 shows the structure of a slit pore with the atomic surface, where the carbon atoms are arranged according to the hexagonal structure of graphite. The smooth wall and atomic wall are the explicit representation of the smooth and the corrugated surface of the pore walls respectively. The diffuse wall takes the atomic surface, but implicitly reflects the vibrational motion of the solid atoms by using the fluid-solid thermal diffuse scattering (TDS) algorithm (which will be described in Section 4.2.6).

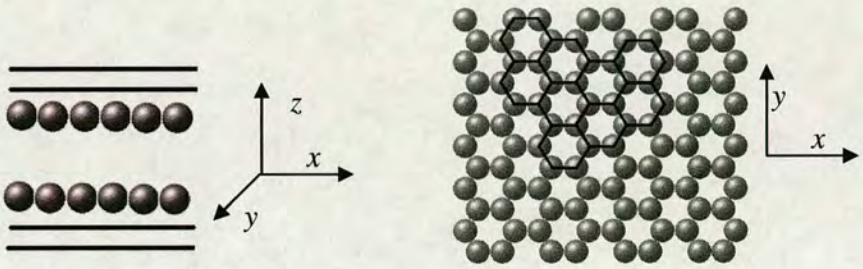

Figure 4.1 Structure of a slit pore with atomic surface

4.2.2 Determination of the fluid density in the pores

Methane is chosen as the adsorptive for studying diffusion in carbon pores, as it is one of the adsorptives used to characterize the porous structure in Chapter 2 and the main component of natural gas. The storage of natural gas has attracted a large amount of work. It has been found that compared to the conventional storage method in heavy steel cylinders at high pressure (20 MPa), natural gas can be stored at a promising low pressure (3 - 4 MPa) in nanoporous carbons at 298 K.[163] In this work, diffusion of methane in carbon nanopores is investigated at pressures ranging from 1 – 40 bar (1, 5, 10, 30 and 40 bar). This study will give us a picture of how fast or slow methane diffuses in pores of different sizes at different pressures.

Remember that the MD simulation is carried out in a system with a constant number of molecules. The numbers of molecules in the pores at different pressures are determined by carrying out the GCMC simulation in the corresponding pores at 298 K. This relates the adsorptive density to the pressure. The GCMC simulation method is described in Chapter 2. For each isotherm point, the system is allowed to equilibrate over 10^7-10^9 Monte Carlo (MC) steps, where an MC step involves one random creation/destruction attempt and a move. After equilibration, data is collected over further 10^7-10^9 steps. Figure 4.2 shows the adsorption isotherms from GCMC simulations for pores of different sizes. The number of molecules adsorbed in each pore to be put in MD simulations is thus determined. The thermodynamic correction factor $d\ln f / d\ln c$, for the calculation of transport diffusion coefficient using Eq. 4.5, can also be determined from the isotherm. Figure 4.3 shows the density profile of methane as a function of pore width w.

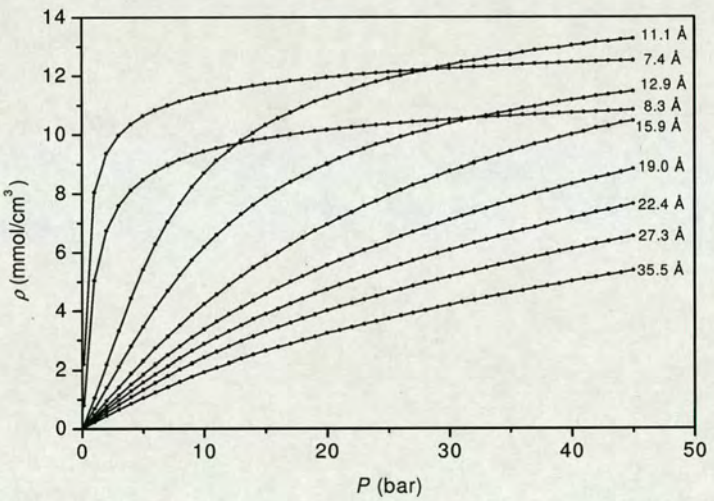

Figure 4.2 Adsorption isotherms of CH_4 in a series of slit carbon pores at 298 K from GCMC simulation.

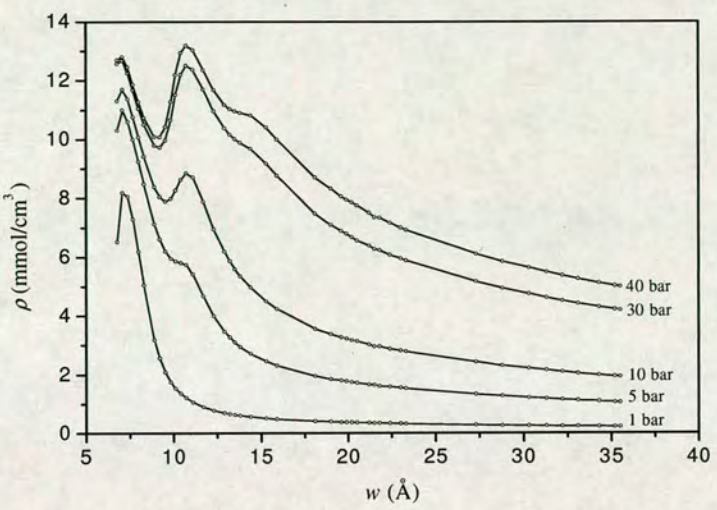

Figure 4.3 Variation of density of CH_4 as a function of pore width w at 298 K, from GCMC simulation.

4.2.3 Initialization of the system

In a system of N molecules at temperature T, the initialization is done by randomly giving the molecules non-overlapping initial positions and attributing to each velocity component of every molecule a value that is drawn from a uniform distribution in the interval [-0.5, 0.5]. A Maxwell-Boltzmann distribution of velocity is rapidly established by molecular collisions.[151] To ensure that the initial system is at the desired temperature which is associated with the mean kinetic energy, the mean kinetic energy is adjusted to the desired value. All velocities are shifted such that the total momentum is zero and the resulting velocities are scaled with a factor $(T/T(t_0))^{1/2}$. $T(t_0)$ is the instantaneous temperature at time t_0, given by:

$$k_B T(t_0) = \frac{1}{N}\sum_{i=1}^{N} m_i \boldsymbol{v}_i^2 \tag{4.9}$$

where k_B is the Boltzmann constant and m_i is the molecular mass of molecule i.

4.2.4 The force field

In MD simulations, the molecular positions, $\boldsymbol{r}$, are obtained by solving Newton's classical equation of motion:

$$m_i \frac{\partial^2 \boldsymbol{r}_i(t)}{\partial t^2} = \boldsymbol{F}_i(t) = -\frac{\partial U(\boldsymbol{r}^N)}{\partial \boldsymbol{r}_i} \tag{4.10}$$

where $\boldsymbol{F}_i(t)$ is the force acting on molecule *i*, and $U(\boldsymbol{r}^N)$ is the interaction energy of molecule *i* with the system. The force acting on each molecule changes whenever the molecule itself or any other molecule in the system changes its position.

The force field considered here comes from the fluid-fluid interaction and the fluid-solid interaction. The fluid-fluid interaction can be calculated using the 12-6 Lennard-Jones potential function (Eq. 2.13). The interaction between a fluid molecule and the solid is calculated as follows. In pores with smooth walls, the interaction between a fluid molecule and the graphite planes of the walls is calculated using Steele's 10-4-3 potential (Eq. 2.14). When the pore surface is atomic, the interaction between a fluid molecule and the carbon atoms on the first graphite layer of the carbon wall is calculated using LJ 12-6 potential and the interaction between the fluid molecule and the rest of the graphite layers of the carbon wall is calculated using Steele's 10-4-3 potential. For LJ 12-6 potential calculation, interactions are truncated and shifted with a cutoff radius of $5.35\sigma_{CH4}$ for the fluid-fluid interaction and $2.5\sigma_{CH4}$ for the fluid-solid interaction. All the parameters needed refer to Table 2.2 in Chapter 2.

4.2.5 Equations of motion

The equations of motion are integrated using a finite difference method. The essential idea of finite difference methods is that the integration is broken down into many small stages, each separated by a fixed time step Δt. The size of Δt depends on the method but Δt should be significantly smaller than the typical average time between collisions of two molecules.[151] In this work, $\Delta t = 1.5$ fs is used, as this has been shown a suitable time step for the system we are studying.[42] There are many algorithms for integrating the equations of motion. In general, any algorithm that conserves the total energy (i.e. where the numerical error does not cause a drift in the total energy) and makes the molecule positions vary smoothly with time can be used.

In this work, the Verlet-based algorithms are used to integrate the equations of motion, as they are fast and exhibit little long-term energy drift.

The Verlet algorithm (see, e.g. Allen & Tildesley, 1987[151]) is based on a Taylor series expansion of position of molecule *i* about time *t*.

$$\boldsymbol{r}_i(t+\Delta t) = \boldsymbol{r}_i(t) + \boldsymbol{v}_i(t)\Delta t + \frac{\boldsymbol{F}_i(t)}{2m_i}\Delta t^2 + \frac{\boldsymbol{r}_i(t)}{3!}\Delta t^3 + \mathrm{O}(\Delta t^4) \tag{4.11}$$

$$\boldsymbol{r}_i(t-\Delta t) = \boldsymbol{r}_i(t) - \boldsymbol{v}_i(t)\Delta t + \frac{\boldsymbol{F}_i(t)}{2m_i}\Delta t^2 - \frac{\boldsymbol{r}_i(t)}{3!}\Delta t^3 + \mathrm{O}(\Delta t^4) \tag{4.12}$$

Summing up the two equations yields the Verlet algorithm:

$$\boldsymbol{r}_i(t+\Delta t) = 2\boldsymbol{r}_i(t) - \boldsymbol{r}_i(t-\Delta t) + \frac{\boldsymbol{F}_i(t)}{m_i}\Delta t^2 + \mathrm{O}(\Delta t^4) \tag{4.13}$$

Eq. 4.13 states that the position of a molecule at time $t+\Delta t$ is related to the positions at time t and $t-\Delta t$, with an error of $\mathrm{O}(\Delta t^4)$. This shows that the Verlet algorithm is properly centred (i.e. $\boldsymbol{r}(t-\Delta t)$ and $\boldsymbol{r}(t+\Delta t)$ play symmetrical roles in Eq. 4.13), making it time-reversible. For this reason the Verlet algorithm gives good conservation of the total energy (see, e.g. Allen & Tildesley, 1987[151] and Haile, 1992[164]). As we can see, the velocities do not appear explicitly in the Verlet algorithm (Eq. 4.13), but they are useful for estimating the kinetic energy (and hence the total energy). If the velocity is of interest, it can be calculated from the formula:

$$\boldsymbol{v}_i(t) = \frac{\boldsymbol{r}_i(t+\Delta t) - \boldsymbol{r}_i(t-\Delta t)}{2\,\Delta t} + \mathrm{O}(\Delta t^2) \tag{4.14}$$

An alternative formulation of the Verlet algorithm is the "velocity Verlet" scheme of Swope *et al.*[165] The velocity Verlet algorithm takes the form:

$$\boldsymbol{r}_i(t+\Delta t) = \boldsymbol{r}_i(t) + \boldsymbol{v}_i(t)\cdot\Delta t + \frac{\boldsymbol{F}_i(t)}{2m_i}\Delta t^2 \tag{4.15}$$

$$\boldsymbol{v}_i(t+\Delta t) = \boldsymbol{v}_i(t) + \frac{1}{2}\Delta t\left(\frac{\boldsymbol{F}_i(t)}{m_i} + \frac{\boldsymbol{F}_i(t+\Delta t)}{m_i}\right) \tag{4.16}$$

This method, with its numerical stability, convenience and simplicity, has been a very attractive algorithm to apply.

Another popular Verlet-based algorithm is the so called "leapfrog" algorithm, which takes the form:[151]

$$\boldsymbol{r}_i(t+\Delta t) = \boldsymbol{r}_i(t) + \boldsymbol{v}_i(t+\frac{1}{2}\Delta t)\Delta t \tag{4.17}$$

$$\boldsymbol{v}_i(t+\frac{1}{2}\Delta t) = \boldsymbol{v}_i(t-\frac{1}{2}\Delta t) + \frac{\boldsymbol{F}_i(t)}{m}\Delta t \tag{4.18}$$

The current velocities may be calculated:

$$\boldsymbol{v}_i(t) = \frac{1}{2}\left[\boldsymbol{v}_i(t-\frac{1}{2}\Delta t) + \boldsymbol{v}_i(t+\frac{1}{2}\Delta t)\right] \tag{4.19}$$

This is necessary so that the energy at time t can be calculated, as well as any other quantities that require positions and velocities at the same instant. Following this, Eq. 4.18 is used to propel the positions once more ahead of the velocities. Because the leapfrog algorithm needs only small storage, it is suitable for extremely large-scale studies where storage can become an important issue.

The velocity Verlet algorithm is used in the systems with the diffuse wall, whilst the leapfrog algorithm is used in the systems with the smooth wall and the atomic wall. They are so chosen because the equations of motion are always coupled with the appropriate thermostats to keep the temperature of the system constant during the simulation. This will be given in Section 4.2.6.

4.2.6 Thermostats

The algorithms used to calculate the trajectories of molecules conserve the total energy of the system, giving a constant-energy system. Therefore, the microscopic properties we can obtain in such MD simulations are those at a constant (N, V, E) condition, corresponding to the micro-canonical ensemble in statistical mechanics. As discussed before, MD simulations performed in this work should be at constant

temperature, in accordance with the real experiment, i.e. the canonical ensemble with constant (N, V, T) should be used. The constant temperature MD simulations thus require the control of temperature. From a statistical mechanical point of view, keeping a system at constant temperature means bringing it into thermal contact with a large heat bath. There are different thermostats to keep temperature constant. A key factor in distinguishing between these methods is the way in which the thermal contact between the studied system and a heat bath is taken into consideration. The details of these thermostats can be found in the book by Allen and Tildesley[151] and a review paper by Nosé [166]. Here we just introduce the two thermostats used in this work: the Gaussian thermostat and the thermal diffuse scattering (TDS) algorithm. The Gaussian thermostat is a mathematical method to keep temperature constant by rescaling the velocity of every molecule at each time step; while the TDS algorithm adjusts the temperature by collisions of the fluid molecules with the pore wall, which is more descriptive of the physical situation.

Gaussian thermostat

The idea of the Gaussian thermostat is to introduce a mechanical constraint ξ to Newton's equation of motion to ensure constant kinetic temperature dynamics. The constraint is chosen so as to perturb as little as possible the classical equations of motion. This principle of least constraint is due to Gauss, and so it is called the Gaussian thermostat.[167] Brown and Clarke[168] proposed a variant of the leapfrog scheme, to combine with the least constraint method. The leapfrog velocity equation (Eq. 4.18) takes its modified form:

$$\boldsymbol{v}_i(t+\frac{1}{2}\Delta t) = \boldsymbol{v}_i(t-\frac{1}{2}\Delta t) + (\frac{\boldsymbol{F}_i(t)}{m} - \xi \boldsymbol{v}_i(t))\Delta t \qquad (4.20)$$

Eq. 4.20 implies that the Brown-Clarke form of the Gaussian thermostat actually rescales the velocity of every molecule using the mechanical constraint ξ at every time step. It is very simple and easy to implement. Moreover, it gives correct thermodynamical quantities and dynamical response in simulations at constant temperature. For simple systems (for example, the systems in our work where the

molecules can be taken as LJ particles), the Gaussian thermostat is a good choice. As the Gaussian thermostat has been a standard method to keep temperature constant,[151] it is used in this work, except for the diffuse wall condition where the TDS algorithm is used.

Thermal diffuse scattering (TDS) algorithm

The TDS algorithm developed by MacElroy and Boyle[23] keeps the temperature constant in a way that the temperature is adjusted by collisions of the fluid molecules with the pore wall, which mimics the physical situation. A full description of the TDS algorithm is given in the paper by MacElroy and Boyle.[23] Here we just give a brief description. The method involves changing the momentum and kinetic energy of the molecules at potential minimum of the fluid/wall interaction. Fluid molecules coming close to the pore wall are reflected from a collision plane located at the potential minimum according to the cosine law of diffusive scattering, while simultaneously satisfying conditions corresponding to thermal equilibration with the surface of the walls. Molecules emanated from the collision plane are scattered with a Maxwellian distribution of molecular speeds. This thermal effect takes place only during a collision of a fluid molecule with a carbon atom on the wall and does not influence the other molecules in the system. The velocity Verlet algorithm gives great convenience to couple with the TDS algorithm for calculating trajectories of molecules.

4.2.7 The structure of the MD program

With the recipes of the MD simulation given in previous sections, we now summarize the structure of the MD program in Figure 4.4. The system will go through a number of time steps till it reaches equilibrium, i.e. the properties to be calculated do not change with time any more. Finally, properties of interests are calculated. In this work, we are interested in self-diffusion coefficients and transport diffusion coefficients. The calculation of these two properties will be introduced in the following sections.

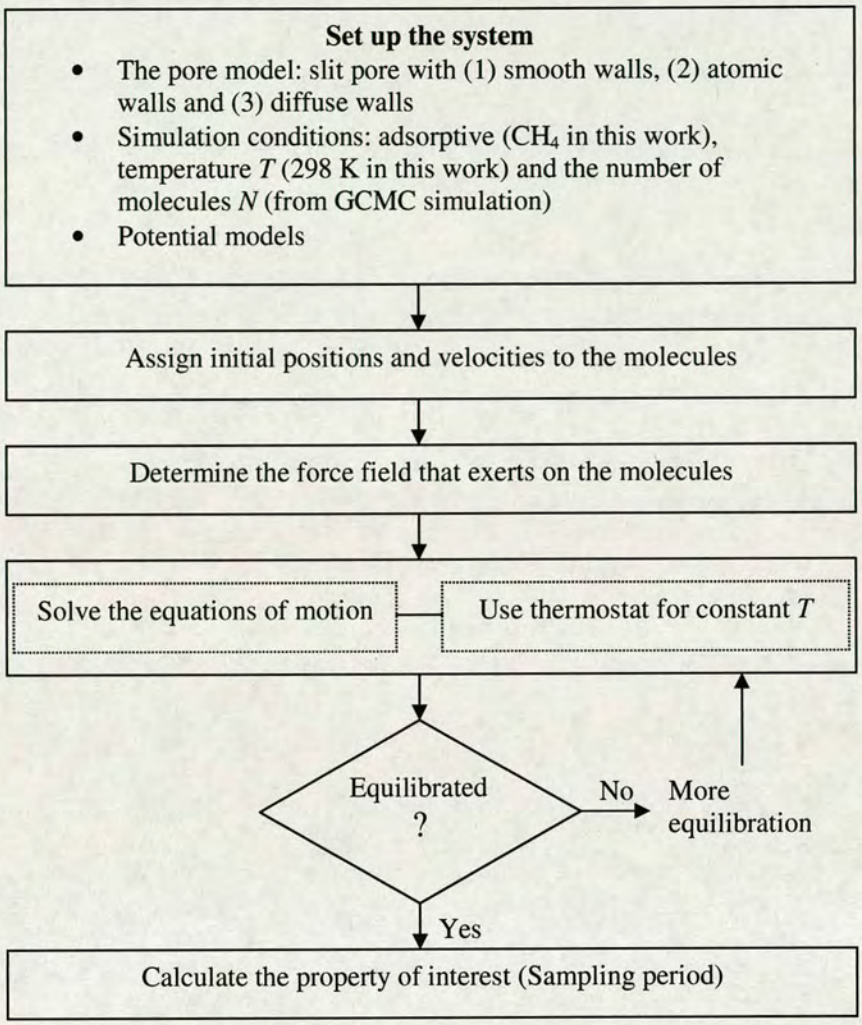

Figure 4.4 Schematic diagram showing the structure of the MD program

4.2.8 MD for self-diffusion

We use equilibrium MD (EMD) simulations to study self-diffusion. Self-diffusion coefficients are related to the mean square displacement (MSD) according to Eq. 4.1:

$$D_s = \frac{1}{4t}\lim_{t\to\infty}\frac{1}{N}\sum_{i=1}^{N}\left[(x(t)-x(0))^2+(y(t)-y(0))^2\right] \tag{4.21}$$

Note that we just measure the MSD in the x and y directions, as the movements of molecules along the pore walls are important and the movements in the z direction perpendicular to the pore walls are negligible. For every molecule, we measure the distance travelled in time t, and plot the mean square of these distances as a function

of time t, as shown in Figure 4.5. Eq. 4.21 states that in the limit of $t \to \infty$, the MSD is proportional to t, i.e. $MSD = 4D_s t$. However, in an MD simulation, it is computational demanding to reach the limit of $t \to \infty$. In practice we simulate long enough so that a linear relation between the MSD and t is established. The self-diffusion coefficient D_s is obtained by finding the slope of the linear part, where $MSD = 4D_s t + const$. A self-diffusion coefficient D_s of 4.58×10^{-8} m^2/s is obtained from the slope of the linear part shown in Figure 4.5.

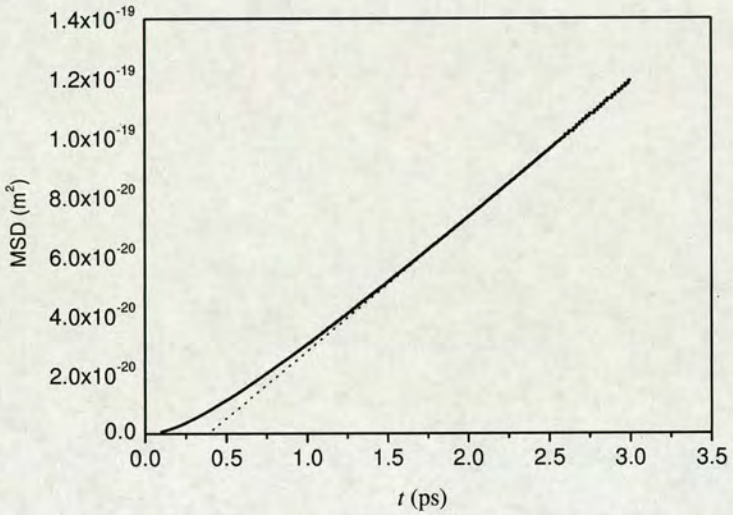

Figure 4.5 Development of MSD (solid line) with time in a pore of 12.9Å with atomic walls at 30 bar. The slope of the dotted line gives the self-diffusion coefficient D_s.

Due to the variation of the fluid density in pores of different sizes at different pressures, different simulation lengths are required to assure that the system reaches equilibrium, and then there is sufficient time to collect data with acceptable statistical errors. In our case, total simulation lengths (including equilibrating lengths and sampling lengths) ranging 0.42 ns – 12.0 ns are used.

4.2.9 MD for transport diffusion

As shown in Eq. 4.5, the transport diffusion coefficient is calculated from the Onsager coefficient L which can be obtained from MD simulations. There are four MD methods that can be used to calculate the Onsager coefficient L: dual control

volume grand canonical molecular dynamics (DCV-GCMD),[23, 41, 42, 130, 131, 169, 170] gradient relaxation molecular dynamics (GRMD),[33] equilibrium molecular dynamics (EMD),[28, 32, 36, 46, 171] and external force non-equilibrium molecular dynamics (EF-NEMD).[30, 33] A critical comparison of these simulation methods was given by Arya *et al.*[172]

The DCV-GCMD method involves the use of two control volumes (reservoirs) located at the ends of a diffusion zone and maintained at different chemical potentials through insertion and deletion of molecules by Monte Carlo moves. A concentration (chemical potential) gradient along the diffusion zone is thus created and the molecules are driven to move under the influence of this concentration gradient. This method has been enthusiastically adopted by many researchers[23, 41, 42, 130, 131, 169, 170] because it is a conceptually attractive method – concentration or chemical potential gradients are established that mimic a real system, and the flux develops as a natural consequence. The DCV-GCMD method requires that the ratio of Monte Carlo to MD moves to be large so that the reservoirs are maintained at a fixed chemical potential, which is computationally intensive. Moreover, it has been argued that the addition of "streaming velocities" to newly inserted molecules is necessary to avoid discontinuities in velocities at the reservoir/transport region interface, and that failure to add these streaming velocities leads to severely underestimated fluxes.[131] However, the streaming velocity is not known *a priori*, and so the addition of the proper streaming velocity is nontrivial. The GRMD method has a good physical basis as in this method an actual concentration gradient is set up within the simulation cell and then allowed to relax using MD.[33] However, this method suffers from some difficulties in setting up an initial concentration profile and uncertainty about whether or not the simulation is occurring in the linear response regime (The importance of the linear response behaviour of MD simulations will be discussed later.). The EMD method involves the use of the Green-Kubo relation which includes both the autocorrelation (self-diffusion) and cross-correlation of molecules to calculate the corrected diffusivities. Computing corrected diffusivities from EMD simulations requires averaging over multiple independent simulations. This method is straightforward to implement, and because it is an equilibrium method, allows the

user to compute other equilibrium properties from a single simulation. This method has been used to calculate single and multicomponent diffusivities in zeolites. [28, 32, 36, 46, 171] The EF-NEMD method involves using an extra external force to mimic a chemical potential gradient along the pore. This method was first applied by Maginn *et al.*[33] to predict transport diffusivity of gases in zeolites, and recently by Chempath *et al.*[30] to predict multicomponent transport coefficients in faujasite. The EF-NEMD method is also used to simulate transport properties of electrolytes, for example, Wheeler and Newman simulated aqueous KCl and NaCl salt solutions[173] and Tang *et al.*[174] simulated the transport properties of water-KCl in a nanopore.

Arya *et al.*[172] concluded from their work that EMD and EF-NEMD are the best methods to use when examining diffusion along a pore; the transport coefficients calculated from these two methods agree well with each other. Sanborn and Snurr[175] have shown that EMD might not work well for multi-component systems at low loadings or when one species is very dilute. Chempath *et al.*[30] demonstrated in their work that EF-NEMD is more efficient than EMD when calculating transport diffusivities of multi-component in faujasite. Our work here is the first application of the EF-NEMD method for calculating transport diffusivities in nanoporous carbons.

EF-NEMD Simulation

In the EF-NEMD simulation, an external force F_{ex} is applied to every molecule in the x-direction (i.e. along the pore), and hence a chemical potential gradient along the x-direction is generated. The force field in this case is from two parts: the potential of the system itself and the external force. Newton's equation of motion given by Eq. 4.10 now becomes:

$$m_i \frac{\partial^2 \boldsymbol{r}_i(t)}{\partial t^2} = \boldsymbol{F}_i(t) = -\frac{\partial U(\boldsymbol{r}^N)}{\partial r_i} + F_{ex} \tag{4.22}$$

where $U(r)$ is the interaction energy of molecule i with the system, as described in Section 4.2.4.

The system responds to this external perturbation by developing a flux along the *x*-direction. The flux *J* during the simulation is given by:

$$\langle J \rangle = \rho \langle v \rangle = \rho \frac{1}{\tau} \int_0^{t=\tau} (\frac{1}{N} \sum_{i=1}^{N} v_i) dt \tag{4.23}$$

where $\langle J \rangle$ is the average flux, ρ is the density of molecules in the pore, $\langle v \rangle$ is the average velocity over all the molecules and also over the length of the simulation, *V* is the pore volume, τ is the time span of the simulation. By taking the integral inside the summation and substituting $\rho = N/V$, Eq. 4.23 becomes:

$$\langle J \rangle = \frac{1}{V} \frac{1}{\tau} \sum_{i=1}^{N} \int_0^{t=\tau} v_i dt = \frac{1}{V\tau} \sum_{i=1}^{N} [r_i(\tau) - r_i(0)] \tag{4.24}$$

Thus only the final positions and initial positions of all molecules are needed for the evaluation of the average flux. Once the steady-state value of the flux $\langle J \rangle$ has been measured in the linear regime, the coefficient *L* is then obtained by dividing it by the applied force:

$$L = \frac{\langle J \rangle}{F_{ex}} \tag{4.25}$$

Complete details of the EF-NEMD method can be found else where.[30, 33] The advantages of this technique are that it is easy to implement, computationally efficient, and a range of gradients may be used. The latter feature enables us to examine and ensure that the system is actually in the linear response regime. Linear response theory describes the reaction of an equilibrium system to a small external perturbation and defines generalized "susceptibilities" that are expressed in terms of various equilibrium correlation functions. This enables statistical mechanics to deal with the system away from equilibrium (see, e.g. Rapaport, 1995[176]). So in MD simulations, it is very important that the system responds to the perturbation satisfying the linear response theory, i.e. in the linear regime.

Determination of the appropriate external force

The linear response regime is examined simply by conducting a series of simulations at increasingly small external force and extrapolating the result to zero strength. The linear response is seen in pores of a wide range of sizes and at all the investigated pressures. Figure 4.6 gives an example of the linear response of the flux $\langle J \rangle$ to the applied external force F_{ex} in a pore of 35.5 Å (the biggest pore used in our simulations) at 1 bar (the lowest pressure in this work) at 298 K. The linear regime investigated and shown in Figure 4.6 is: (0-0.4) kJ/(mol Å) for the system with smooth walls, (0-0.1) kJ/(mol Å) for the system with atomic walls, and (0-0.4) kJ/(mol Å) for the system with diffuse walls. Note that the response of $\langle J \rangle$ to F_{ex} behaves differently for different wall conditions (for example, the reduced flux is largely different). This is because the applied external force does work on the system and different systems react to the force differently. Further discussion will be given later.

Ideally, it is better to use as big an external force as possible while remaining in the linear regime. Figure 4.7 shows the variation of transport diffusivities obtained from the EF-NEMD simulations with different external forces. With the smaller force (F_{ex} = 0.05 kJ/(mol Å)), the scatter in the data is greater because the flux is smaller; the system needs longer time to equilibrate. Figure 4.7 shows that with F_{ex} = 0.1 kJ/(mol Å), the system equilibrates at t = 9 ns, while with F_e = 0.05 kJ/(mol Å), the system is still not in equilibrium at t = 10 ns. This shows the importance of using a sufficiently large external force.

However, it is not always true that the largest possible F_{ex} should be used. When the TDS algorithm is used (as described in Section 4.2.6), in the systems with diffuse walls, we found that bigger F_{ex} makes the kinetic energy of the system drift. Figure 4.8 gives an example of this effect. It can be seen that the kinetic energy (indicated by triangles) drift away when the big F_{ex} of 0.2 kJ/(mol Å) is added to the system, leading to higher kinetic energy and therefore higher temperature. This happens because the TDS algorithm used in the diffuse wall condition to keep the system at constant temperature works in such a way that only the molecules that collide with

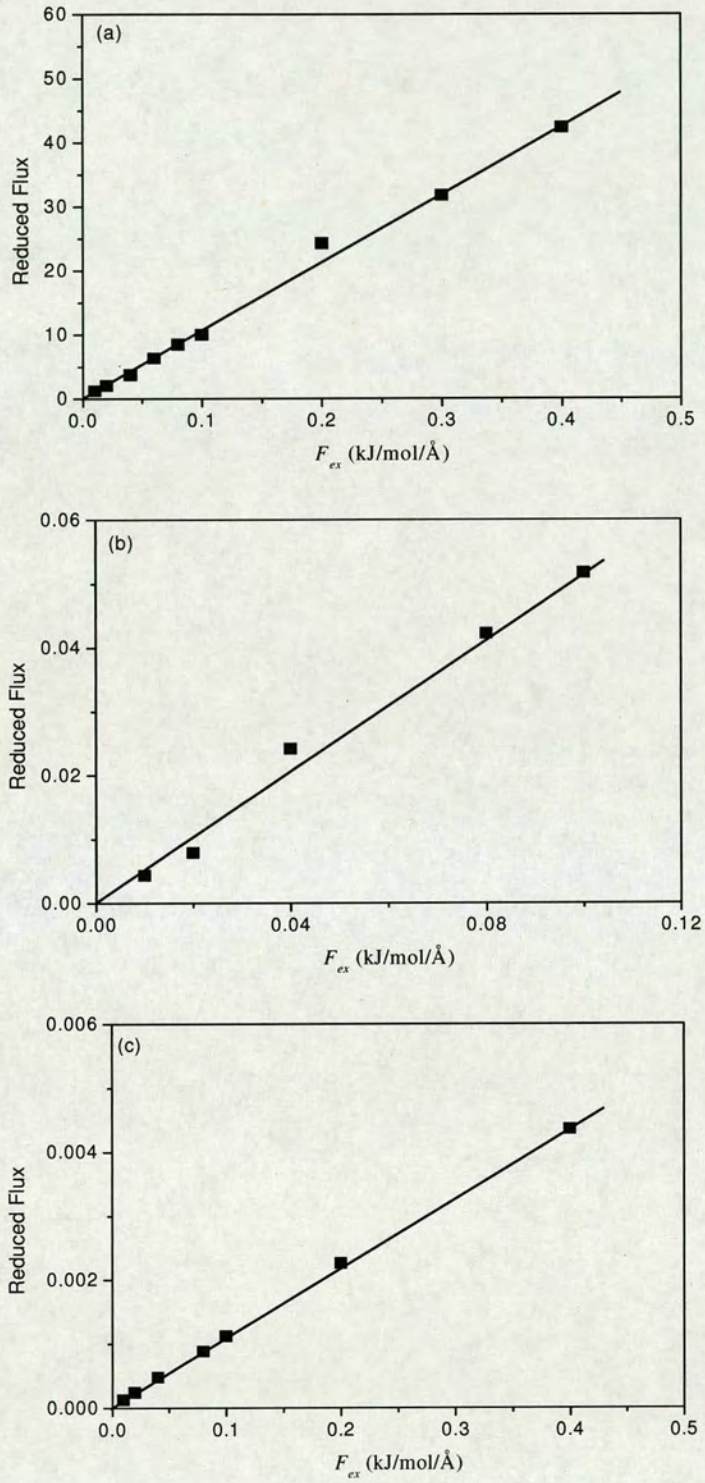

Figure 4.6 Linear response behaviour of the flux responds to the external force in a pore of 35.5 Å with (a) smooth walls, (b) atomic walls and (c) diffuse walls at 1 bar, 298 K.

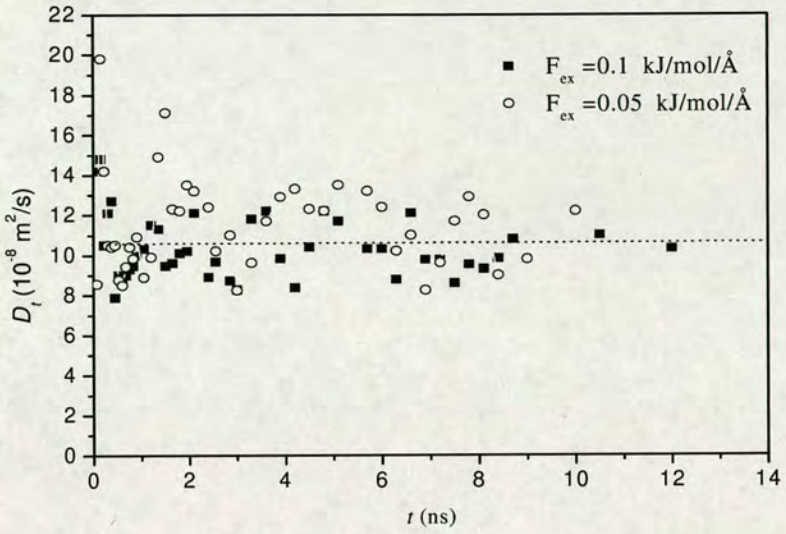

Figure 4.7 Influence of applied external forces on the simulation length in a pore of 35.5Å with diffuse walls (47 CH_4 molecules in the pore).

the walls are affected by this thermostat. When the pore is very big (as given in Figure 4.8, the pore width is 35.5 Å), some molecules in the middle of the pore are unable to collide with the walls. Under the influence of the big F_{ex}, these molecules just move away without colliding with the walls. Figure 4.9 shows a snapshot of the system during the simulation. We can see that although most of the molecules are very close to the pore walls, a considerable number of them are in the middle of the pore. In this case, F_{ex} leads to heating of the system, which is not desirable.

To ensure that the system is at the desired temperature during the simulations, a small value of F_{ex} = 0.1 kJ/(mol Å) is used for systems with diffuse walls. The kinetic energies have been checked to show that the systems with this F_{ex} are at the desired temperature of 298 K. For convenience, an external force of F_{ex} = 0.1 kJ/(mol Å) is also determined for the systems with smooth walls and with atomic walls, although larger force (for example, F_{ex} = 0.3 kJ/(mol Å)) can be used. Note that the energy drift effect caused by larger forces is not observed with the systems with smooth walls and atomic walls, in which the Gaussian thermostat "rescales" the velocity of every molecule at every time step.

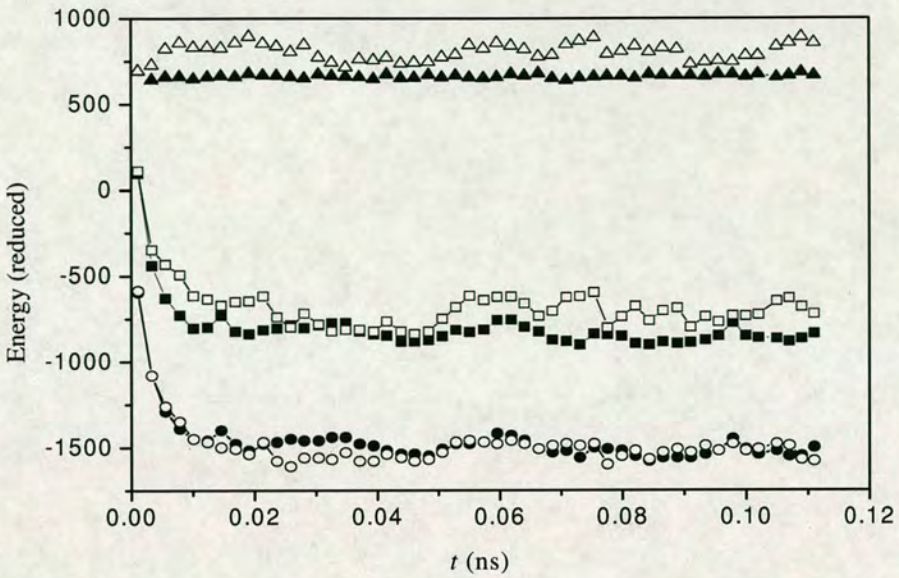

Figure 4.8 Influence of external force on the energy for a pore of 35.5 Å with 225 CH_4 molecules. The filled symbols indicate the energy of the system without an external force, and the empty symbols indicate the energy with an external force of F_{ex}= 0.2 kJ/(mol Å). Triangles indicate kinetic energy, circles indicate potential energy and squares indicate total energy.

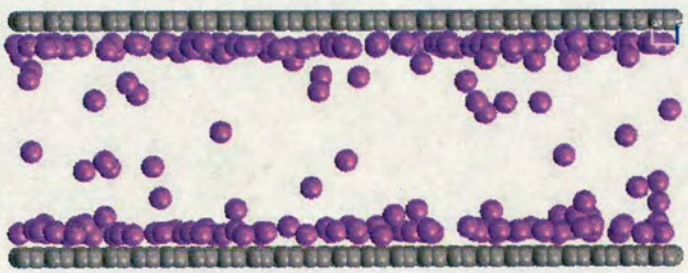

Figure 4.9 A snapshot of the configuration of CH_4 molecules (represented by purple spheres) in a pore of 35.5 Å at 298 K. The total number of CH_4 molecules in the pore is 225.

The simulation length for EF-NEMD simulations can be examined by conducting a series of simulations with increasing simulation length to see the variation of transport diffusivities, for example, as shown in Figure 4.7. When the simulation length is long enough, the transport diffusivity will stay at a constant value. The

simulation length is determined from where the constant value begins. Due to the variation of the fluid density in pores of different sizes at different pressures, different simulation lengths are required to assure that data are collected when the system has reached equilibrium. In this case, total simulation lengths (including equilibrating lengths and sampling lengths) ranging 0.42 ns – 12.0 ns are used.

4.3 Comparison between the Atomic Wall and the Diffuse Wall

In this section, we compare the influence of the atomic wall and the diffuse wall on self-diffusion and transport diffusion. As described in Section 4.2, both the atomic wall and the diffuse wall provide a structured surface, but apply different thermostats; the atomic wall is associated with the Gaussian thermostat whilst the diffuse wall is associated with the TDS thermostat. The comparison between the atomic wall and the diffuse wall is in fact a comparison between the two thermostats. The two thermostats work on the system differently: the Gaussian thermostat works on every molecule by rescaling the velocities of the molecules at every time step to keep temperature constant, whilst the TDS thermostat works on the molecules colliding with the pore walls by reflecting them diffusively, thus giving the diffuse wall condition. The Gaussian thermostat is a long standing thermostat whilst the TDS thermostat is quite new and its applicability has been questioned recently.[40]

4.3.1 Comparison for self-diffusion

Figure 4.10 shows the variations of self-diffusion coefficients as a function of pore size. At a given pressure, the self-diffusivities increase with increasing pore width in a manner related to the packing of fluid molecules in the pores. While the density of adsorbed CH_4 molecules in the pores decreases with increasing pore width, shown in Figure 4.3, the self-diffusion coefficients keep increasing. This indicates that the density of the fluid inside the pore plays an important role in determining the mobility of the fluid in the pore. The denser the molecules pack in the pore, the more difficult it is for them to move around and so the shorter the molecular trajectories.

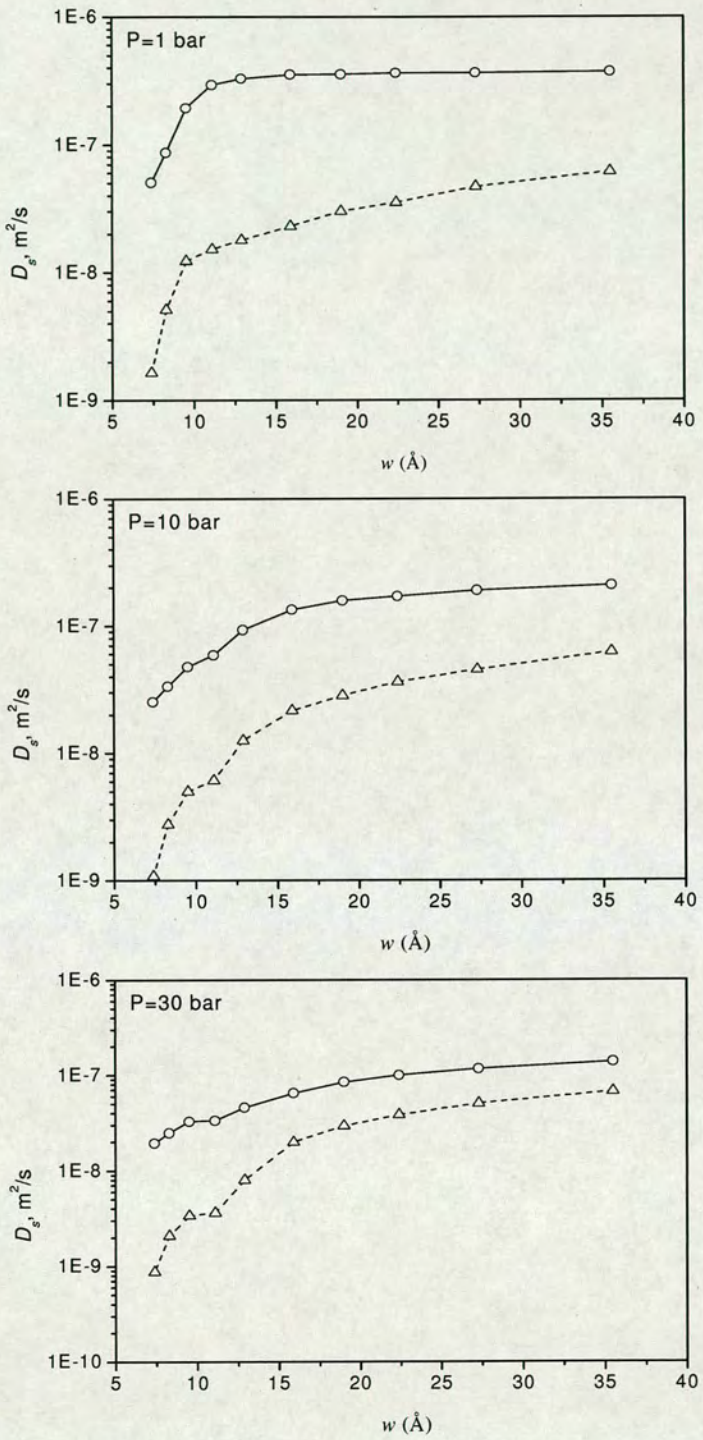

Figure 4.10 Variations of self-diffusion coefficients as a function of pore size, obtained using EMD simulations with atomic walls (empty circles and solid lines) and diffuse walls (empty triangles and dashed lines).

There is a marked difference between the self-diffusivities calculated from the atomic wall and the diffuse wall at all the pressures over all the pores investigated. This is because the TDS thermostat in the diffuse wall gives too many thermalizations (collisions) to the molecules which makes the trajectories of the molecules shorter and so the self-diffusivities smaller. Especially, in the narrow pores (e.g. w = 7.38 Å, 8.3 Å, 11.1 Å, 12.9 Å), the molecules feel strong interaction with the pore walls and have a lot of collisions with the walls, and so the self-diffusivities from the diffuse wall are much lower than those from the atomic wall at all the pressures.

An interesting observation is that the self-diffusivities from the atomic wall and the diffuse wall become closer at very high pressure (e.g. P = 30 bar) in wider pores (e.g. w = 19.0 Å, 22.4 Å, 27.3 Å, 35.5 Å). To explain this, we then come to compare the development of self-diffusivities with pressures in pores of different sizes. As shown in Fig. 4.11, a decrease of the self-diffusion coefficient with increasing pressure is seen in all the pores with the atomic wall, which means that the self-diffusion coefficients is mainly influenced by the fluid density. As the fluid density in the pore increases with increasing pressure, giving more resistance to the movement of the molecules, the self-diffusivity decreases. For the diffuse wall condition, the self-diffusion coefficient decreases with increasing pressure in narrower pores (w = 7.38 Å, 8.3 Å, 11.1 Å, 12.9 Å) but keeps more or less the same with increasing pressure in wider pores (e.g. w = 19.0 Å, 22.4 Å, 27.3 Å, 35.5 Å). This is probably because that both the fluid density in the pore and the TDS thermostat influence self-diffusivity. As we can see from the density variations in different pores, shown in Figure 4.3, fluid density in smaller pores is much higher and the pores are fully filled; in this case, the influence from the density plays a more important role, resulting in a decrease in self-diffusivity with increasing density. In wider pores, the pores are far away from being fully filled; in this case, as pressure increases, more molecules are adsorbed on the surface of the wall, while the number of molecules in the middle of the pore keep more or less the same. Under the influence of the TDS thermostat, the molecules close to the wall surface are kept close to the wall because of many collisions, while the molecules in the middle of the pore are not influenced, so that

the average trajectory keeps more or less the same as increasing pressure. Together with that the atomic wall makes the self-diffusion coefficient decrease with increasing pressure in wider pores, this leads to closer diffusivities obtained from the two wall conditions in wider pores as pressure increases.

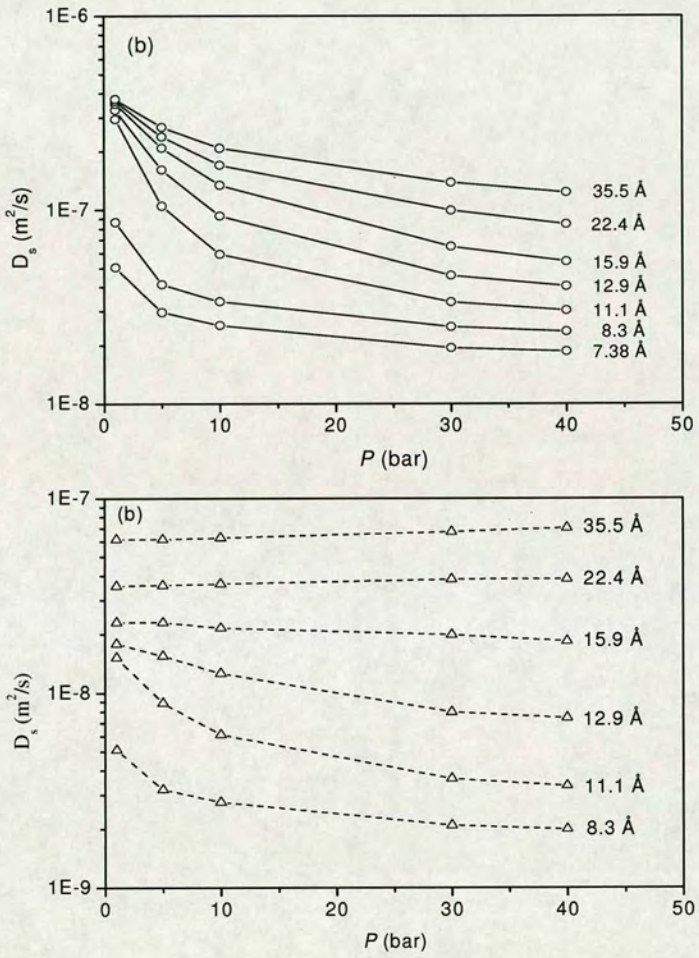

Figure 4.11 Self-diffusion coefficients as a function of pressures, obtained using EMD simulations with (a) the atomic wall and (b) the diffuse wall.

The influence of the atomic wall and the diffuse wall on self-diffusion is for the first time compared directly in this work. Other researchers also investigated self-diffusion using the two wall conditions applied to carbon nanotubes, rather than to

the slit-pore model in this work. Recently, Jakobtorweihen *et al.*[40, 129] investigated the influence of the diffuse wall on self-diffusion in carbon nanotubes, compared to a flexible wall condition. The flexible wall represents the flexibility of the nanotubes by taking into account the vibrations, bending and torsions of the carbon-carbon bonds of the wall, which is a more realistic model for carbon nanotubes. The self-diffusion coefficients obtained with the diffuse wall are three orders of magnitude lower for low loadings and one order of magnitude lower for high loadings than that with the flexible wall. They noted that it is because the diffuse wall gives too many diffuse collisions (thermalizations) that lead to an under-prediction of self-diffusion. Chen *et al.*[38] also examined the self-diffusion using the flexible wall developed by Jakobtorweihen *et al.*, making comparison with the atomic wall (i.e. representing the atomic structure of the carbon nanotube while holding the atoms rigid). Their results showed that the atomic wall give very similar self-diffusion coefficients with that from the flexible wall, which indicates that representing the nanotube wall with atomic detail rather than invoking the flexible wall condition is probably good enough for studying self-diffusion. If we put the results of Jakobtorweihen *et al.* and Chen *et al.* together, the indirect conclusion is that the diffuse wall should give lower self-diffusion coefficients than the atomic wall does. Our results here are very important – they show that the diffuse wall does give lower self-diffusion coefficients, in accordance with the previous work, and so the diffuse wall is unrealistic for this purpose.

Unlike carbon nanotubes where the flexibility of the wall is probably important, in real nanoporous carbons, it is unlikely that the wall has flexibility. The atomic wall is likely to be a good approximation for real carbons. However, there is no work indicating that the TDS thermostat in the diffuse wall condition influences transport diffusion in the same way as it influences self-diffusion. As self-diffusion and transport diffusion are fundamentally different, it is important to investigate the influence of the TDS thermostat on transport diffusion as this will show if the diffuse wall should be used for studying transport diffusion.

4.3.2 Comparison for transport diffusion

Figure 4.12 shows the development of transport diffusivity with pressure in pores of different sizes using the atomic wall and the diffuse wall. We see that the development of transport diffusivity with pressure varies in pores of different sizes. As given in Eq. 4.5, transport diffusivity calculated is the product of two terms: the flux which is influenced by the wall conditions and the density of the pore fluid, and the thermodynamic factor. The behaviour of the transport diffusivity depends on the interplay of these factors and can exhibit a variety of behaviours.

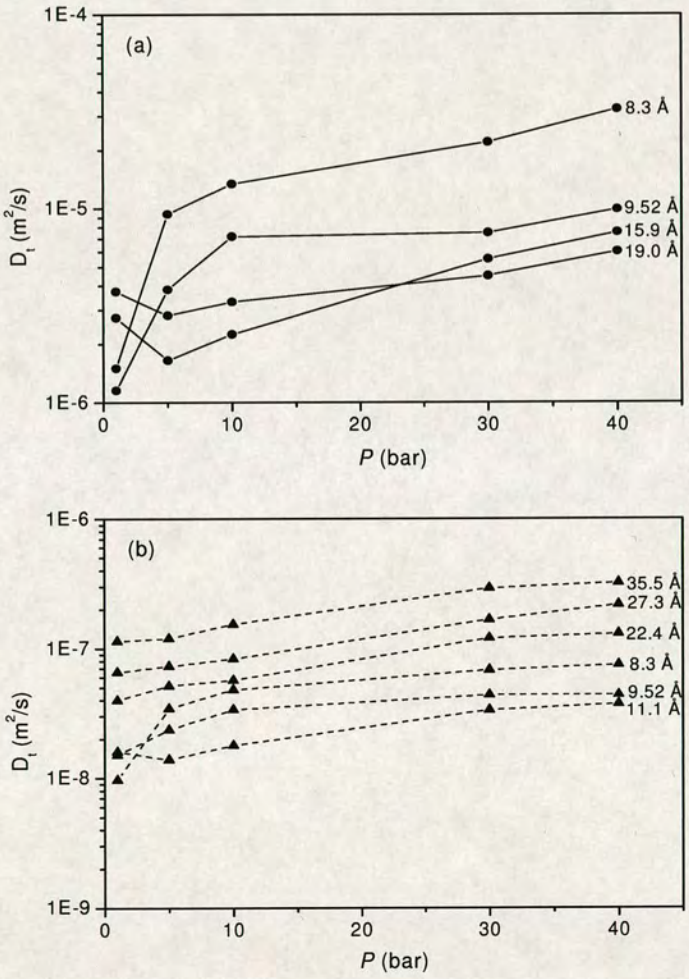

Figure 4.12. Transport diffusion coefficients, as a function of pressure, obtained using EF-NEMD simulations with (a) smooth walls and (b) atomic walls.

As shown in Figure 4.12, transport diffusion coefficients generally increase with increasing pressure. As expected, this is in agreement with previous studies on different materials.[28, 38, 39, 46] The variation of transport diffusivities with pressure in pores of different sizes is very different from the behaviour of self-diffusivities which decrease with increasing pressure, shown in Figure 4.11. This can be explained by examining the mechanisms of self-diffusion and transport diffusion. In the case of self-diffusion, the motion of a molecule is influenced by the molecules around it and how it interacts with the walls; the denser the molecules pack in the pore, the more difficult it is for them to move around and so the shorter the molecular trajectories. Whilst in the case of transport diffusion, apart from the influence from the system itself as in the case of self-diffusion, the motion of a molecule is under the influence of a gradient along the pore length (i.e. the external force in the x direction); the denser the molecules pack in the pore, the less freedom they have in moving along the direction of the pore width (i.e. the z direction) and the faster they can move along the direction of the external force, so that the flux in the x direction is larger. This indicates that transport diffusivities are different properties from self-diffusivities. The roles that different wall conditions play in self-diffusion can not be taken to study transport diffusivity.

Figure 4.13 shows the variations of transport diffusion coefficients with pores of different sizes. The development of transport diffusion coefficients with pore sizes (or indirectly, with the fluid density in the pores) shows the dependence of transport diffusion coefficients on density. As we can see, the diffuse wall gives lower transport diffusion coefficients than the atomic wall does. The transport diffusion coefficients from the diffuse wall are in the order of 10^{-8} m^2/s, which is in accordance with previous work with the diffuse wall condition but using the DCV-GCMD simulation method.[42] Whilst, the transport diffusivities from the atomic wall are in the order of 10^{-6} m^2/s, which are two orders of magnitude higher than those from the diffuse wall. The much lower transport diffusivity from the diffuse wall can be attributed to that the TDS thermostat gives too many thermalizations (collisions) to the molecules, as in the case of self-diffusion.

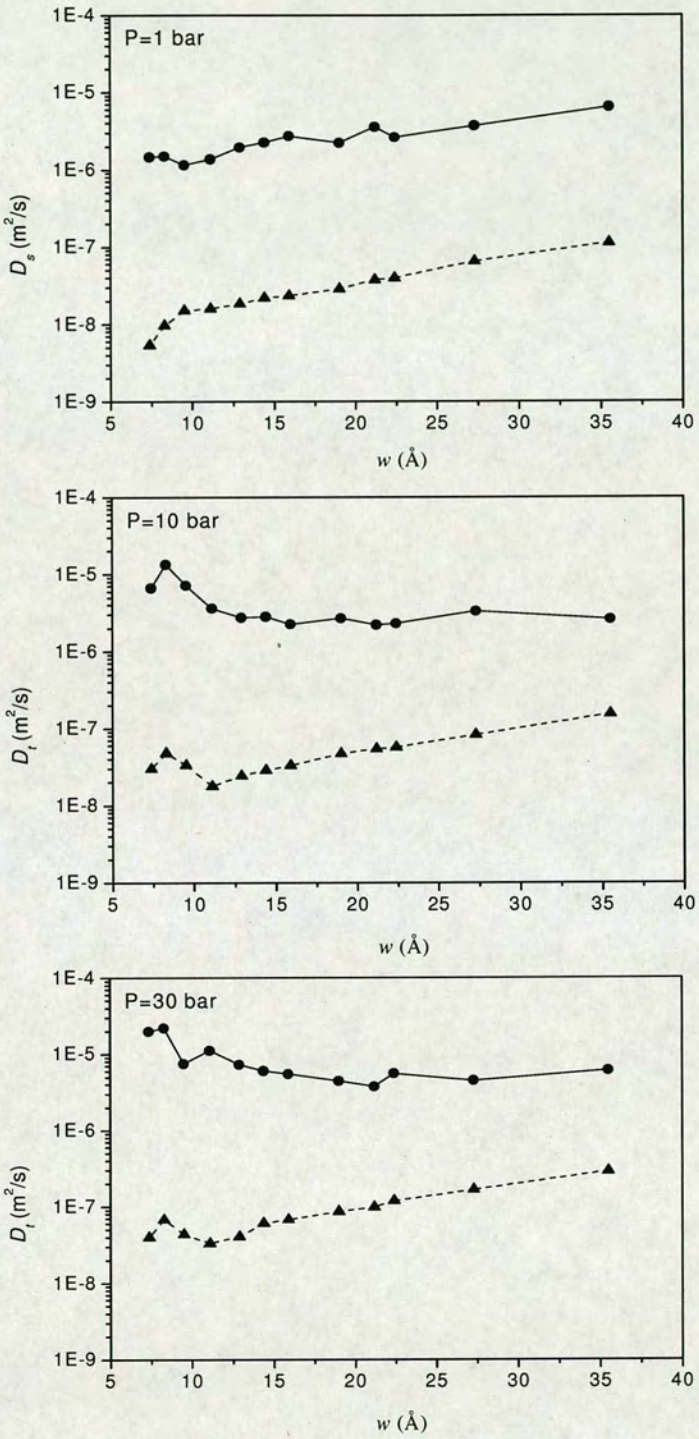

Figure 4.13 Variations of transport diffusion coefficients as a function of pore size, obtained using EF-NEMD simulations with atomic walls (filled circles and solid lines) and diffuse walls (filled triangles and dashed lines).

From the discussions in Section 4.3.1 and Section 4.3.2, we can conclude that the diffuse wall, which makes use of the TDS thermostat, should not be used in MD simulations to study either self-diffusion or transport diffusion, as the TDS thermostat gives too many thermalizations to the molecules, resulting in much lower diffusivities.

4.4 Comparison between the Atomic Wall and the Smooth Wall

In the previous section, we discussed that the atomic wall is likely to be a good model for studying diffusion in real carbon materials. However, we have found in the literature that the smooth wall, which assumes the wall surface as smooth, has been used and is still being used extensively for studying self-diffusion and transport diffusion (especially self-diffusion) in nanoporous carbons. On the other hand, we did not find any study on self-diffusion using the atomic wall. Can we say that the results from the smooth wall are not correct as the atomic wall should be more realistic? However, there has been no work so far to compare the two wall conditions in studying diffusion in nanoporous carbons. In this section, we aim to investigate the influence of the smooth wall and the atomic wall on both self-diffusion and transport diffusion, to give a clear idea if the smooth wall should be used at all. Note that the Gaussian thermostat is used in both the smooth wall and the atomic wall. The difference between the two wall conditions is that the smooth wall and the atomic wall present the smoothness and the corrugation of the wall surface respectively.

4.4.1 Comparison for self-diffusion

Figure 4.14 shows the development of self-diffusion coefficients as a function of pressure in pores of different sizes. A decrease of the self-diffusion coefficient with increasing pressure is seen in all the pores with the smooth wall. This is in agreement with previous observation with the atomic wall shown in Figure 2.11 (a). The self-diffusion coefficients generally decrease with increasing pressure, as the increase of pressure results in more molecules adsorbed and so the fluid density in the pore increases, making the motion of the molecule more difficult and so the trajectory shorter, as discussed before.

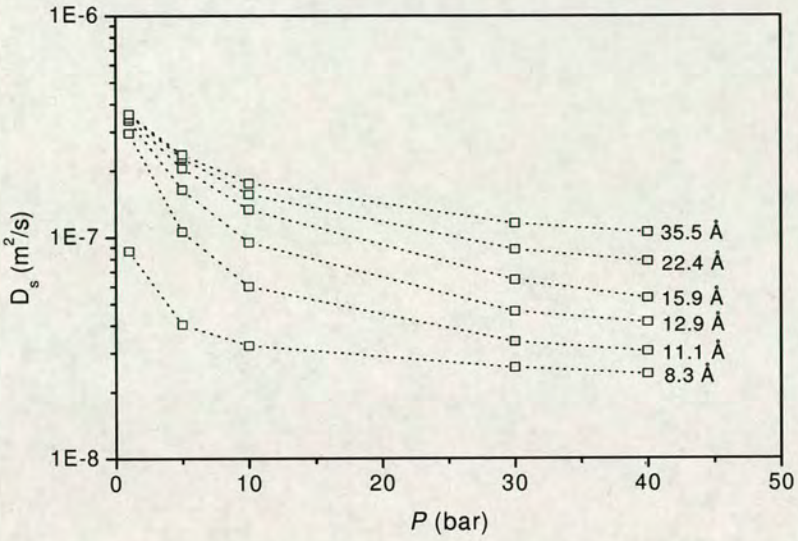

Figure 4.14 Self-diffusion coefficients as a function of pressure, obtained using EMD simulations with the smooth wall.

Figure 4.15 compares self-diffusion coefficients from the smooth wall and the atomic wall. At a given pressure, the self-diffusivities from both the smooth wall and the atomic wall increase with increasing pore width. This is related to the fluid density in these pores (as shown in Figure 4.3), i.e. the fluid density in the bigger pore is lower so that the self-diffusivity is higher. Interestingly, the smooth wall and the atomic wall give very similar self-diffusivities, which are in the order of 10^{-8} m^2/s. There are various but similar values for self-diffusion coefficients in the literature. The self-diffusion coefficients of Ar-Kr,[128] C_2H_6 [45] and CO_2[44] in slit carbon pores are in the order of 10^{-9} m^2/s. The magnitude of the self-diffusion coefficient of CH_4 in a carbon pore of 19.0 Å at 298 K is of the order of 10^{-8} m^2/s in the paper by *Cao et al.*[43] Our simulation results at the same condition also show self-diffusion coefficients of the order of 10^{-8} m^2/s, but a bit higher than the results from Cao *et al.*[43] A possible reason is that different parameters for fluid molecules were used in calculating the interaction potentials.

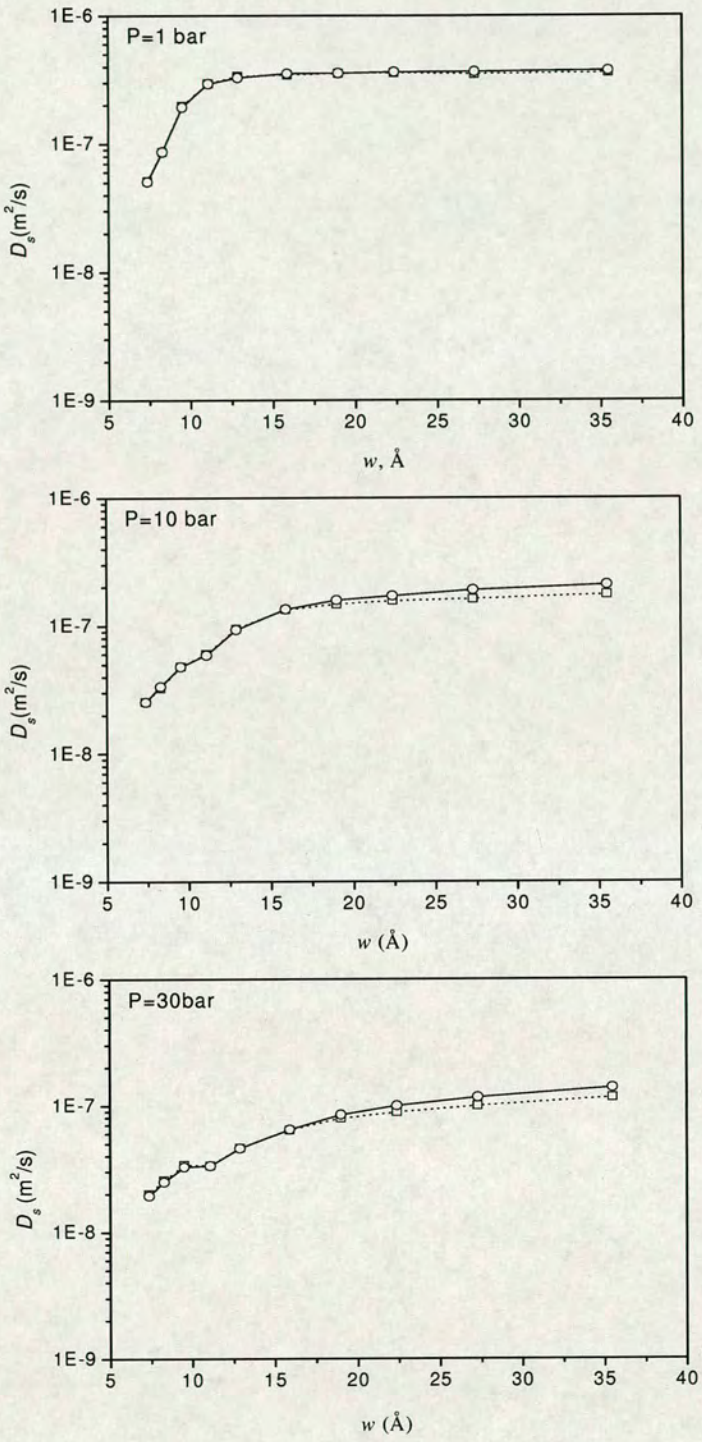

Figure 4.15 Variations of self-diffusion coefficients as a function of pore size, obtained using EMD simulations with the atomic wall (empty circles and solid lines) and the smooth wall (empty squaures and dotted lines).

The similarity between the self-diffusivities from the smooth wall and the atomic wall indicates that the corrugation of the wall surface itself does not influence the trajectories of the molecules that much; both the smooth surface and the corrugated surface reflect the molecules away when colliding and the molecules travel in the pore space. We conclude that the smooth wall can continue being used to investigate the self-diffusion throughout micropores and small mesopores, though it predicts a slightly lower self-diffusion coefficient in small mesopores than the atomic wall does. We note that an EMD simulation with the atomic wall takes much longer time than an EMD simulation with the smooth wall does, because calculating the interaction of molecules with an atomic wall is time demanding. For example, a simulation with the smooth wall takes 6 hours, but a same simulation with the atomic wall may take 2 days. The advantage of using a smooth wall is that it saves computing time.

As we discussed before, self-diffusion is different from transport diffusion. The observation that the smooth wall and the atomic wall give similar self-diffusivity does not guarantee that the two wall conditions will also give similar transport diffusivities. The influence of the smooth wall on transport diffusion will be compared with that of the atomic wall in the following section.

4.4.2 Comparison for transport diffusion

Figure 4.16 compares transport diffusion coefficients from the smooth wall with those from the atomic wall. The transport diffusion coefficients from the smooth wall are extremely high, in the order of 10^{-3} m^2/s, which are 2-3 orders of magnitude higher than those from the atomic wall. This is very different from the observation in Section 4.4.1 that the smooth wall and the atomic wall give similar self-diffusion coefficients.

A comparison, in terms of the difference between transport diffusivities and self-diffusivities exerted by the same wall condition, provides an insight into the role of different wall conditions. Figure 4.17 shows the ratio of transport diffusion coefficients to self-diffusion coefficients, as a function of pore size. We see that the

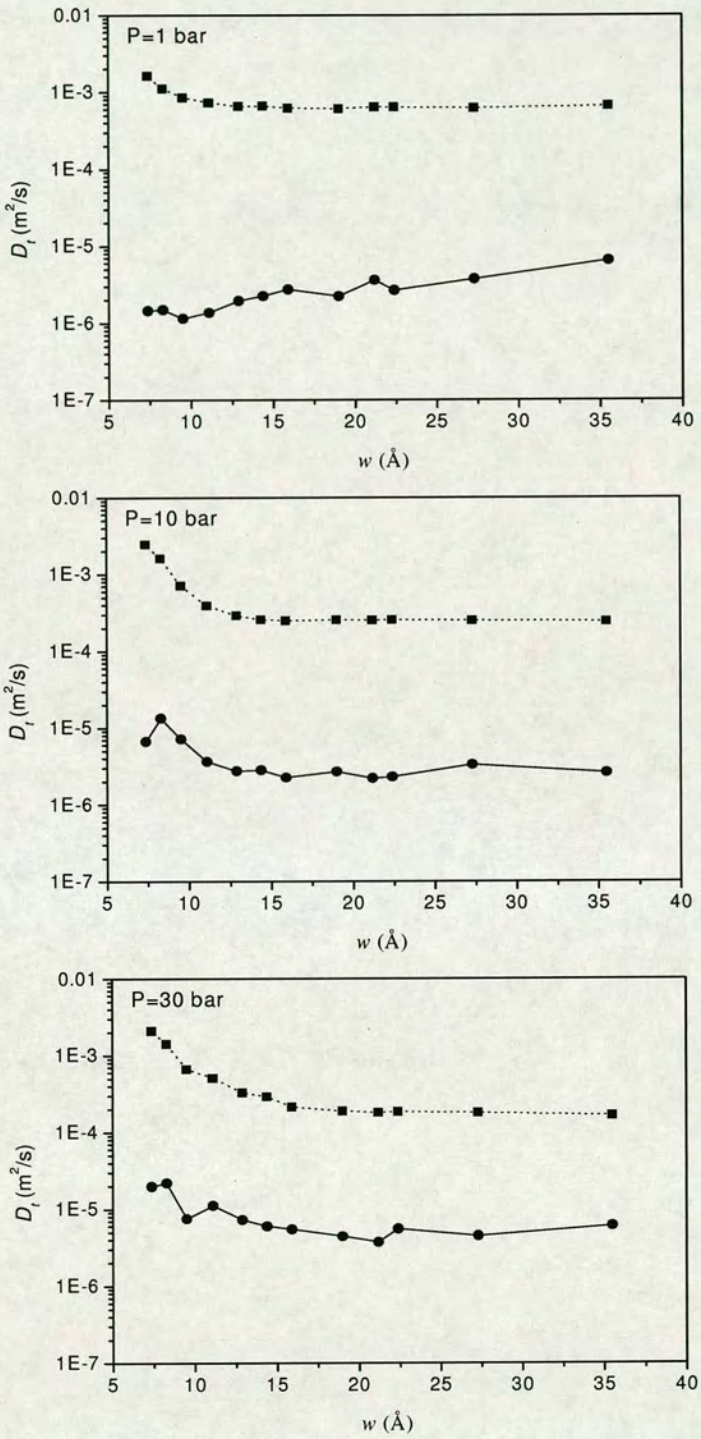

Figure 4.16 Variations of transport diffusion coefficients as a function of pore size, obtained using EF-NEMD simulations with atomic walls (filled circles and solid lines) and smooth walls (filled squares and dotted lines).

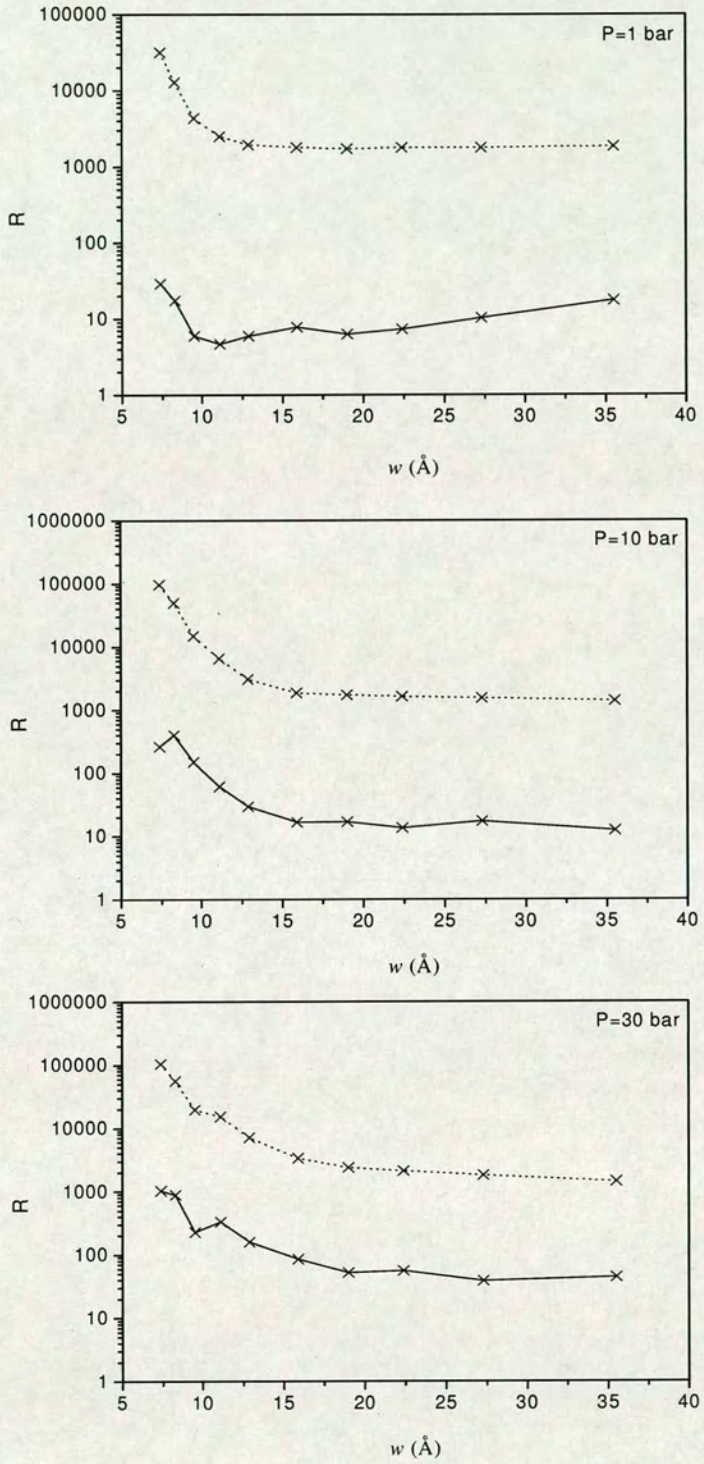

Figure 4.17. Ratio of transport diffusion coefficient to self-diffusion coefficient, as a function of pore size. Solid lines indicate smooth walls and dotted lines indicate atomic walls.

ratios of transport diffusivities to self-diffusivities, $R_{Dt/Ds}$, are about the orders of 10 and 1000 for the atomic wall and the smooth wall respectively in the whole pore size range, except that they are higher in narrower pores (w = 7.38 Å, 8.3 Å and 9.52 Å). In pores of w = 7.38 Å, 8.3 Å and 9.52 Å, only one layer of molecules can be accommodated. It is thus merely impossible for the molecules to move along the pore width. This is true in the case of either self-diffusion or transport diffusion. However, the movement of molecules along the pore length in the x direction are different with or without a driving force. Since the molecules are packed very densely, in the case of self-diffusion without driving force, it is difficult for the molecules to move around, resulting in short trajectories and so small diffusivities; while in the case of transport diffusion, the external force in the x direction drives the molecules to flow along this direction but the movement of the molecules in other directions are restricted, resulting in a high flux and so high transport diffusivity.

The fluid confined by smooth walls moves much faster than the fluid confined by atomic walls. The reasons are as follows. The smooth wall surface offers no resistance to the movements of molecules, so that the molecules merely flow on the surface of the wall. On the other hand, the corrugated surface of the atomic wall offer resistance to the movements of molecules along the direction of the external force; the molecule is reflected away from the walls and spends its time travelling in the pore space. Thus the transport diffusivities from smooth walls are much higher than those from atomic walls. Together with the fact that the self-diffusivities from the two wall conditions are very similar (as discussed in Section 4.4.1), this gives that $R_{Dt/Ds}$ is much higher for the smooth wall than for the atomic wall.

Comparing Figure 4.13 with Figure 4.16, we can see that the transport diffusivities from the atomic wall are lower than those from the smooth wall but higher than those from the diffuse wall. This means that the resistance from the atomic wall to transport diffusion is in between that from the smooth wall and that from the diffuse wall. This agrees with the discussion in Chapter 1: the atomic wall gives the realism of fluid-solid collisions, i.e. collisions of molecules with the wall are partly specular (no momentum lost, in the case of smooth wall) and partly diffuse (complete

momentum lost, in the case of the diffuse wall). A conclusion thus can be drawn that the assumed wall surface influences the transport diffusivities, and the atomic wall condition is a more realistic model for studying transport diffusion.

We therefore will use the transport diffusivities from the atomic wall for the input to the pore network to calculate the effective diffusivities. Figure 4.18 shows the transport diffusivities from the atomic wall in a series of pores at different pressures investigated. As we can see, transport diffusivities generally increase with increasing pressure. Moreover, at the lowest pressure of P = 1 bar, transport diffusivities increase with increasing pore width, whilst at higher pressures (from P = 5 bar) transport diffusivities are much higher in some smaller pores than those in bigger pores. It is very helpful to relate the pore fluid density (which is shown in Figure 4.3) with transport diffusivity. At low pressure (P = 1 bar), the fluid density is low in all the pores. In this case, the effect of the external force to drive the molecules to flow is very weak because the molecules have much free space to move around, and so the effect from the molecule-molecule interaction takes its role, giving that the less the number of molecules, the faster the molecules move, similar with what happens in self-diffusion. This makes the transport diffusivity at 1 bar increase with increasing pore width as the fluid density decreases with increasing pore width. At higher pressures, the molecules pack denser. In this case the effect of the external force to drive molecules to flow becomes important, so that the denser the molecules pack, the less freedom for them to move around and the more preferable the molecules move under the influence of the external driving force. This is why in some smaller pores the transport diffusivities are much higher than those in bigger pores because the molecules in these pores pack much denser.

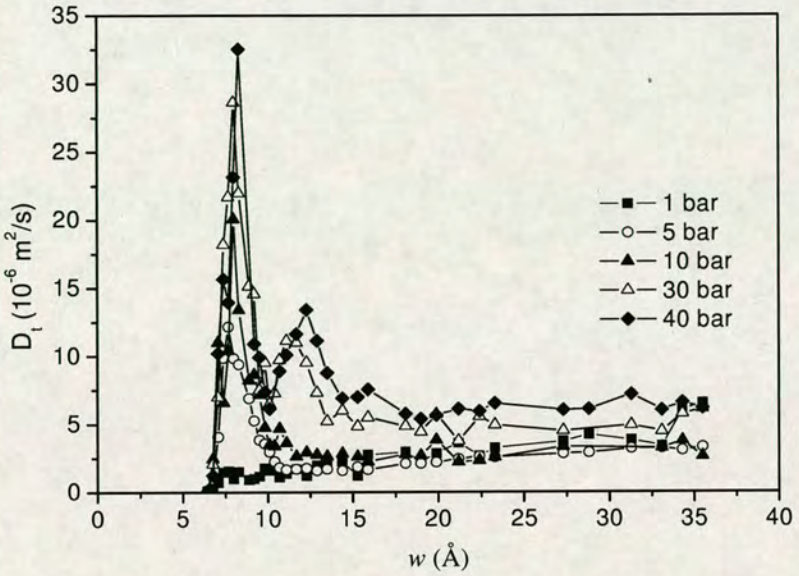

Figure 4.19 Transport diffusion coefficients in a series of pores at different pressures.

4.5 Summary

In this chapter, we have systematically investigated the influence of different wall conditions, namely the smooth wall, the atomic wall and the diffuse wall, on self-diffusion and macroscopic transport in carbon nanopores using molecular dynamics simulations. Self-diffusion coefficients are calculated from EMD simulations, whilst transport diffusion coefficients are calculated from EF-NEMD simulations.

The results show that the diffuse wall underestimates both the self-diffusivity and the transport diffusivity, because the TDS thermostat used to give the diffuse wall condition gives too many thermalizations (collisions) to the molecules and provides an inaccurate description of the wall condition. The diffuse wall (or the TDS thermostat) should not be used for studying diffusion in nanopores.

Representing the wall surface as atomic rather than using a simple smooth wall model or invoking the diffuse condition is very important for studying transport diffusion. The smooth wall gives extremely high transport diffusivities as the

assumed smooth wall surface offers no resistance to the movement of the molecules and the molecules merely flow on the surface of the walls; whilst the diffuse wall underestimates the transport diffusivities by offering too much resistance.

The smooth wall and the atomic wall give very similar self-diffusivities. We conclude that the smooth wall can continue being used to study self-diffusion in carbon nanopores, considering that simulations with the atomic wall are more time demanding.

The atomic wall should be used for studying transport diffusion. The single-pore transport diffusivities which are to be input to the pore network to obtain the effective diffusivities are obtained using EF-NEMD simulations with atomic walls.

5. Prediction of the Effective Diffusivity from the Hybrid MD/PNM Approach

This chapter brings us to the end of the story. Now, let us look back at the previous parts of the story, as this will (hopefully) give us a better understanding of the whole story. In Chapter 2, the pore size distribution (PSD) of the pore network model (PNM) was obtained by analyzing the adsorption isotherms. In Chapter 3, the pore network connectivity, in terms of the mean coordination number, $\overline{Z}$, was obtained by analyzing the PSDs using percolation theory. The PNM thus was built based on the PSD and $\overline{Z}$. In Chapter 4, the database of transport diffusivities in single pores was built by carrying out extensive molecular dynamics (MD) simulations. In this chapter, all these things will be brought together; the effective diffusivity will be obtained by using the single-pore transport diffusivities as input to the PNM using the renormalized effective medium approximation (REMA), as shown below.

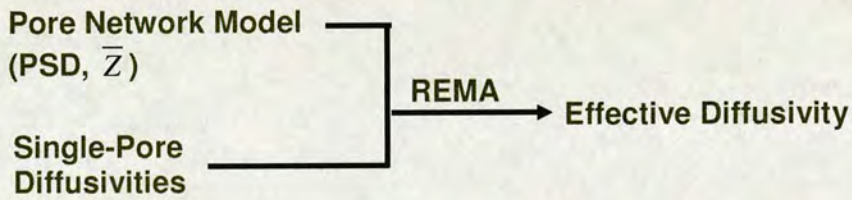

This chapter is arranged as follows. In Section 5.1, the basis of the REMA approach and how this approach is applied to obtain the effective diffusivity will be given. In Section 5.2, the influence of the factors on the effective diffusivity will then be investigated. In Section 5.3, the absolute assessment methodology, which was applied to evaluate the correctness of the adsorption-based PSD in Chapter 2, will be applied here to evaluate the PNM-based approach by comparing the PNM-based effective diffusivity with the actual diffusivity directly from the virtual porous carbon (VPC). Remember that we characterized two VPCs in Chapter 2 and Chapter 3 to build two PNMs that can capture the essential features of the pore network of the VPCs, or the real carbons. The evaluation of the REMA approach in this chapter is based on the two VPCs.

5.1 Calculation of the Effective Diffusivity in the PNM

The macroscopic transport diffusion in the whole pore network is described by Fick's law

$$\boldsymbol{J} = -D_e \nabla \boldsymbol{c} \tag{5.1}$$

where $\boldsymbol{J}$ is the flux across the network, D_e is the effective diffusion coefficient and $\boldsymbol{c}$ is the concentration in the pore space.

The effective diffusivity, D_e, is obtained by solving the diffusion problem at a microscopic level, using the PNM. This involves solving a set of mass balance equations at the nodes of the network. For every node in the network, the mass balance equation is satisfied.

$$\sum J_i = 0 \tag{5.2}$$

where the summation is over all pores that meet at the node, J_i is the microscopic version of Fick's law, describing diffusion through an individual pore. For a slit pore

$$J_i = \frac{D_i(w_i) w_i b_i}{l_i} \Delta c_i \tag{5.3}$$

where $D_i(w_i)$ and Δc_i are respectively the transport diffusion coefficient and the concentration drop across pore *i*. w_i, l_i and b_i are the width, the length and the breadth of pore *i* respectively. The width of each pore on the PNM is associated with a particular pore size, chosen at random from the appropriate pore-size distribution. In our work, the length and the breadth of the slit pore are set to be equal, and only the pore width varies from pore to pore, thus Eq. 5.3 becomes

$$J_i = D_i(w_i) w_i \Delta c_i \tag{5.4}$$

where the quantity

$$g_i = D_i(w_i) w_i \tag{5.5}$$

is called the conductance of pore *i*.

The mass balance equations can be solved numerically to give the effective diffusivity. This approach is called the direct solution (DS) method. In this method, the microscopic concentration field that is needed for the computation of the fluxes in various pores can be obtained by using the direct solution of the transport equation (i.e. Eq. 5.2) for the pore network. Once the concentrations have been calculated, the flux across the lattice and hence the effective diffusivity can be obtained. Unlike the DS method in which the microscopic concentrations in various pores are actually solved, most pore network-based flux models (e.g. REMA) are based on the smooth field assumption (SFA).[137] The REMA and related methods are given in the following.

5.1.1 Effective medium approximation (EMA)

Remember that the disordered pore network of nanoporous carbons is mapped to a 3D simple cubic lattice, as described in Chapter 3, so that the properties of the pore network can be studied on the simple cubic lattice. The bonds and the nodes of the lattice represent the pores and junctions respectively, and the pores carry conductance of the network. For the networks built around the 3D simple cubic lattices, the effective-medium theory for a resistor network by Kirkpatrick[143] can be used to find the effective conductance of each pore, g_e, in a uniform network that presents, approximately, the same overall resistance to diffusion as the original network, as shown in Figure 5.1.

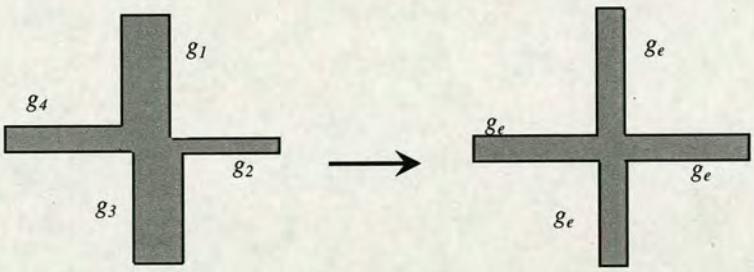

Figure 5.1 A network (on the left) with distributed conductances equal to a network (on the right) with uniform conductances g_e. The two networks present the same overall resistance to diffusion.

For a network of uniform pore length and pore breadth (and pore length is equal to pore breadth), which is the case of our network, the pore conductance is a single function of the pore width w ($g(w)$ is thus used to represent the conductance of a pore of width w), as shown in Eq. 5.5. In this case, the effective medium equation for the mass transport problem in the pore network is written[137]

$$\int_w \frac{g(w)-g_e}{g(w)+(\frac{Z}{2}-1)g_e} h(w)dw = 0 \tag{5.6}$$

where Z is the coordination number of the network of cubic lattice ($Z = 6$), $h(w)$ is the conducting bond distribution which is associated with the PSD as the conductance is only a function of pore size, $h(w)dw$ is the number of pores per unit volume of porous medium in the interval $[w, w+dw]$. For a network in which the mean coordination number is reduced from that of the original network by the random removal of bonds, the conducting bond distribution, $h(w)$, is given below.

$$h(w) = (1-p)\delta(w) + pn_n(w) \tag{5.7}$$

where $\delta(w)$ is the Dirac delta function, and p is the bond occupation probability which is the mean coordination number $\overline{Z}$ of the modified network divided by the coordination number of the original network (i.e. $p = \overline{Z}/6$). $n_n(w)$ is the PSD, defined in Eq. 3.2, renormalized so that its integral is unity. So $n_n(w)$ is a pore-size distribution function in terms of the number of pores.

The effective conductance, g_e, calculated using Eq. 5.6, is then used to determine the effective diffusivity of the network, utilizing the observation that a network of pores of uniform conductance satisfies the smooth field approximation (SFA).[137] The SFA[137] assumes that the concentration gradient in a pore can be represented by the projection of the macroscopic concentration gradient on the pore axis. Figure 5.2 gives a schematic illustration of this. For a pore identified by the subscript i, the SFA states that the concentration gradient, Δc_i, is related to the macroscopic concentration gradient, ∇c, by

$$\Delta c_i = l_i \underline{n}_i \bullet \nabla c \tag{5.8}$$

where $\underline{n}_i$ is the unit vector parallel to the pore axis and l_i is the length of pore i.

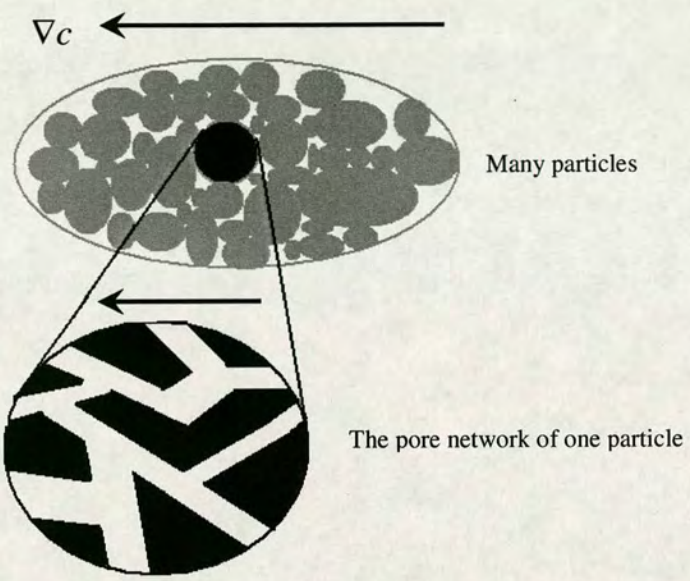

Figure 5.2 Schematic illustration of the pore network of one of the many particles, with the axis of each pore forming a certain angle with the direction of the macroscopic concentration gradient.

Solving Eq. 5.2, by making use of Eq. 5.4, 5.5 and 5.8, taking the summation of the pore flux (as in Eq. 5.2) over all the pores present in the network, the effective diffusivity for a 3D network of pores of uniform length is given by

$$D_e^S = \frac{1}{3} K \bar{g} l_u^2 \tag{5.9}$$

where K is the number of pores per unit volume of porous medium, $\bar{g}$ is the number-average pore conductance over the network, and l_u is the pore length. The superscript S is used to denote the effective diffusivity obtained from the smooth field approximation. Details about how Eq. 5.9 is derived can be found in the paper of Burganos *et al.*[137]

As a network of pores of uniform conductance g_e (which is obtained with the EMA approach) satisfies the smooth field approximation and g_e is actually the number-average pore conductance over the network in this case, the effective diffusivity given in Eq. 5.9 becomes

$$D_e^{E-S} = \frac{1}{3} K g_e l_u^2 \tag{5.10}$$

where the superscript *E-S* means the combination of EMA and SFA approaches. The number of pores per unit volume, K, is related to the porosity of the solid, ε_p, by the equation

$$\varepsilon_p = K l_u b_u \langle w \rangle \tag{5.11}$$

where l_u and b_u are the pore length and breath of a slit pore respectively, $\langle w \rangle$ is the arithmetical mean value of the pore width in the network.

$$\langle w \rangle = \int_0^\infty n_n(w) w dw \tag{5.12}$$

Comparison of the estimated diffusivities using EMA with those obtained from the DS method reveals high accuracy and reliability of the method when the bond occupation probability p is much greater than the percolation threshold p_c.[137] The correct percolation threshold of a cubic lattice network is $p_c = 0.2493$,[144] whilst the EMA gives a higher value of $p_c = 1/3$. The EMA gives a wrong p_c because it can not deal with the networks close to p_c.

5.1.2 Renormalized effective medium approximation (REMA)

It has been shown that the EMA method is inaccurate when the network is close to the percolation threshold.[134] This indicates that the EMA method can not be used directly in this work, as the mean coordination numbers of the mapped lattices of the two carbons studied in this work ($\overline{Z}_1 = 1.65$ for Carbon 1 and $\overline{Z}_2 = 2.06$ for Carbon 2) are close to the percolation threshold of the lattice ($Zp_c = 1.5$). The renormalized effective medium approximation (REMA) is thus used in this work for the calculation of the effective diffusivity. REMA was first proposed by Sahimi *et al.*[134] by combining the real-space renormalization group (RSRG) theory[177-179] and the

EMA method, to enable an excellent prediction in the region that p is close to the percolation threshold p_c. Effectively, the REMA method allows a larger section of the network to be handled, i.e. for networks that are far or close to the percolation threshold.

The real-space renormalization group (RSRG) theory

The idea of RSRG is that cells of conducting bonds in a system with p close to p_c behave as single bonds in a renormalized system that has renormalized p farther from p_c. The system renormalization is achieved by removing sites and joining the remaining sites with new bonds to form a lattice of the original type. The mean coordination number does not change after renormalization since it is determined solely by the lattice topology. After renormalization, the new network is farther from the percolation threshold than the original one, and so the problem of the inaccurate value of p_c in EMA is avoided.

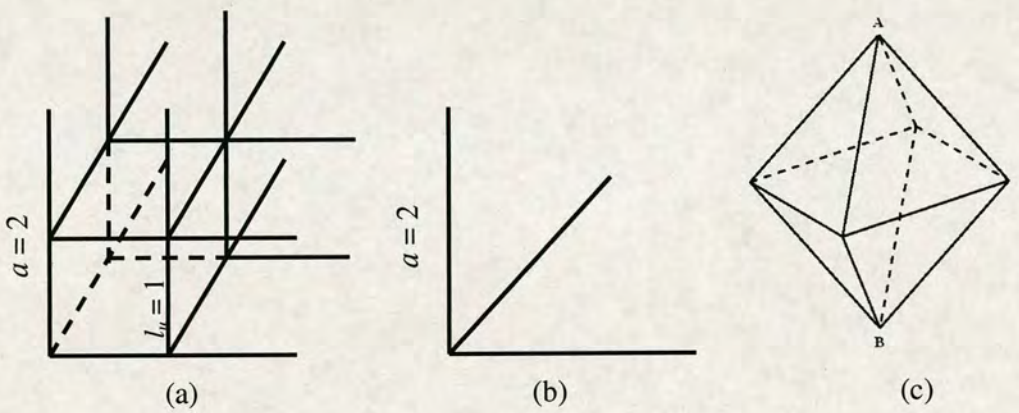

Figure 5.3 (a) the example cell for the simple cubic lattice; (b) bonds that replace the example cell after renormalization; and (c) an octahedral network that has an equivalent electrical circuit to the example cell.

An example of renormalization of the simple cubic lattice is shown in Figure 5.3. The original network can be divided into identical cells of linear dimension $a = 2$. To differentiate from the unit (smallest) cell of the simple cubic lattice, we call such a cell the "example cell". Figure 5.3 (a) shows an example cell that consists of 8 identical unit cells of linear dimension $l_u = 1$. The conducting bonds are distributed

according to the conductance distribution $h(w)$ (as shown in Eq. 5.7); that is, the bonds are absent with probability (1-p), and the remaining bonds are assigned conductance which is related to the pore size from the distribution $n_n(w)$. The example cell of Figure 5.3 (a) is equivalent to the electrical circuit of the octahedral network with 12 bonds shown in Figure 5.3 (c) (a generalized Wheatstone bridge). The renormalization procedure is repeated. After several realizations of renormalization, the example cell can be replaced by three renormalized bonds shown in Figure 5.3 (b). The linear dimension of the renormalized cell is then a factor of a larger than that of the unit cell of the original network.

The fraction of occupied bonds changes on renormalization. The conducting bond distribution h (w) given in Eq. 5.7 after renormalization is $h'(w)$.

$$h'(w) = [1 - R(p)]\delta(w) + R(p)n_n'(w) \tag{5.13}$$

where $R(p)$ is the renormalized bond occupation probability, and $n_n'(w)$ is the renormalized pore size distribution.

The conducting bond distribution of the renormalized network, $h'(w)$, satisfies that the renormalized bonds offer the same resistance to transport as the original cell. That is, if a potential difference were applied in turn across a large number of replicas of the original cell with the conducting bonds being assigned at random from $n_n(w)$, the measured distribution of currents would be the same as those calculated from the conductance distribution of the renormalized bonds.

Figure 5.4 shows the renormalized bond occupation probability, $R(p)$, vs. the original bond occupation probability p for the renormalization cell of Figure 5.3 (a), taken from the paper of Zhang and Seaton.[139] If the initial fraction of occupied bonds satisfies $p^* = R(p^*)$, the fraction of occupied bonds does not change as a result of renormalization, and p^* is an estimate of percolation threshold p_c. If $p > p^*$, the fraction of occupied bonds increases with each renormalization step and tends to unity. If $p < p^*$, the fraction of occupied bonds decreases with each renormalization

step and tends to zero. Thus, with each renormalization, the system moves further from the percolation threshold. In reality, we are only interested in the case of $p > p^*$, as in the region of $p < p^*$, the network is not connected and not open to diffusion.

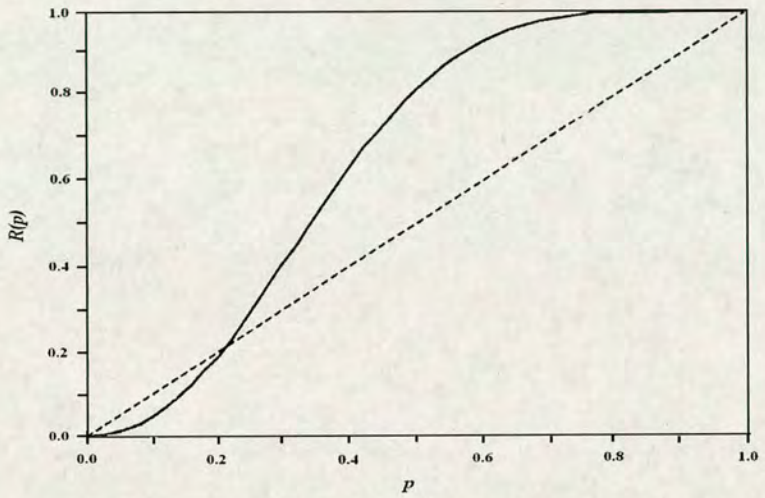

Figure 5.4 Renormalized bond occupation probability, R (p), vs. the original bond occupation probability, p, as depicted by the solid line. The dashed line gives $R(p) = p$.

The REMA approach

The REMA approach, which combines the RSRG theory and the EMA method, involves calculation of the renormalized conducting bond distribution, $h'(w)$, and the renormalized conductance, $g'(w)$, to replace the original $h(w)$ and $g(w)$ in Eq. 5.6, for calculating the renormalized effective conductance, g_e' based on Eq. 5.6. However, calculating $h'(w)$ for many renormalization steps is very difficult and time-consuming.[179] Sahimi *et al.*[134] found that carrying out only a single renormalization step was good enough: REMA performed very well in the region of the percolation threshold. In particular, for a simple cubic lattice, the percolation threshold calculated from REMA is p_c = 0.265, much closer to the true value of 0.2493 than either the RSRG value of 0.2085 or the EMA value of 1/3.

Zhang and Seaton[139] adapted the basic REMA approach of Sahimi *et al.*[134] and used it for the prediction of the effective diffusivity of porous solids with continuous pore size distribution. Their method is described in detail as follows. In each realization of

the example cell of Figure 5.3 (a), every bond in the equivalent electrical circuit of Figure 5.3 (c) is labelled as occupied with probability p, or unoccupied with probability (1-p). If it is occupied, it is assigned a pore size randomly from the pore size distribution. The conductance of each occupied bond is assigned from the database of the single-pore transport diffusivities. The renormalized conductance for each realization is calculated using the solution to the mass balance equations for the circuit, which is given in Appendix I. In this calculation, caution is required to deal with the unoccupied bonds. If a cluster of one or more occupied bonds is not attached to either end of the equivalent electrical circuit, the potentials of the nodes in that cluster are indeterminate and the conductance matrix is singular. To avoid this problem, the unoccupied bonds are assigned a small conductance, chosen so that it is much smaller than any of the real conductances in the network. This procedure has a negligible effect on the calculated renormalized conductance. The output of this procedure is a set of renormalized conductances g_i', which is then input to EMA. If g_i' is the renormalized value of quantity g_i for realization i, Eq. 5.6 becomes

$$\frac{1}{N}\sum_i \frac{[g_i' - g_e']}{[g_i' + (\frac{Z}{2} - 1)g_e']} = 0 \tag{5.14}$$

where N is the number of realizations of the renormalization cell. Large number of realizations is desired for obtaining accurate results. However, Zhang and Seaton have shown that the error introduced by carrying out only 10,000 realizations is less than 1%, so this number of realizations may be sufficient for practical purposes. In this work, N = 20,000 is used.

The effective diffusivity is obtained by rewriting Eq. 5.10 with g_e' in place of g_e and $2l_u$ in place of l_u (as each renormalized bond is twice as long as the original).

$$D_e^{REMA} = \frac{1}{3}K'g_e'(2l_u)^2 \tag{5.15}$$

where K' is the number of pores per unit volume in the renormalized network, the superscript *REMA* denotes the effective diffusivity obtained from the REMA approach.

The number of pores per unit volume decreases by a factor of eight on renormalization. So Eq. 5.11 becomes

$$K' = \frac{1}{8} \frac{\varepsilon_p}{< w > l_u \, b} \tag{5.16}$$

Note that in our work, the pore length l_u and the pore breath b are equal. So the effective diffusivity is given

$$D_e^{REMA} = \frac{1}{6} \frac{\varepsilon_p}{< w >} g_e' \tag{5.17}$$

5.2 Factors that Influence the Effective Diffusivity

From Eq. 5.17, we can see that the effective diffusivity obtained from the REMA method is influenced directly or indirectly by the porosity, ε_p, the mean arithmetic pore size, $< w >$, and the effective conductance, g_e'. $< w >$ is related to the pore size distribution. g_e' is the interplay of the mean coordination number, the pore size distribution and the single-pore diffusivities. In the following sub-sections, we will discuss how these factors influence the effective diffusivity.

Remember that we constructed a PNM for each of the two VPCs – Carbon 1 and Carbon 2 – in this work. As we discussed in Chapter 2 and 3, the two carbons have different porosity (ε_{p1} = 0.36 for Carbon 1 and ε_{p2} = 0.49 for Carbon 2), different mean coordination numbers ($\overline{Z_1} = 1.65$ for Carbon 1 and $\overline{Z_2} = 2.06$ for Carbon 2) and different PSDs (shown in Figure 5.5), which form different PNMs. Note that in the PNMs, we are dealing with the number of pores, instead of the volume of pores. So the PSDs shown in Figure 5.5 are the converted PNM-PSDs of Figure 2.15 and 2.18 given in Chapter 2 where the PSDs were shown in terms of pore volume. Here Figure 5.5 (a) shows the PSDs in terms of the probability density of the number of pores, $n_n(w)$; whilst Figure 5.5 (b) shows the PSDs in terms of the corresponding cumulative probability, $C_n(w)$. $n_n(w)$ and $C_n(w)$ are defined in Eq. 5.18 and 5.19 respectively. $C_n(w)$ is the PSD used in the REMA programme whereby a pore size is assigned to each occupied bond, using a random number in the range of (0, 1).

$$n_n(w) = \frac{n(w)}{\int_0^{\infty} n(w)dw} \tag{5.18}$$

$$C_n(w) = \frac{\int_0^{w} n(w)dw}{\int_0^{\infty} n(w)dw} \tag{5.19}$$

where $n(w)$ is the PSD in terms of the number of pores, defined by Eq. 3.2 in Chapter 3.

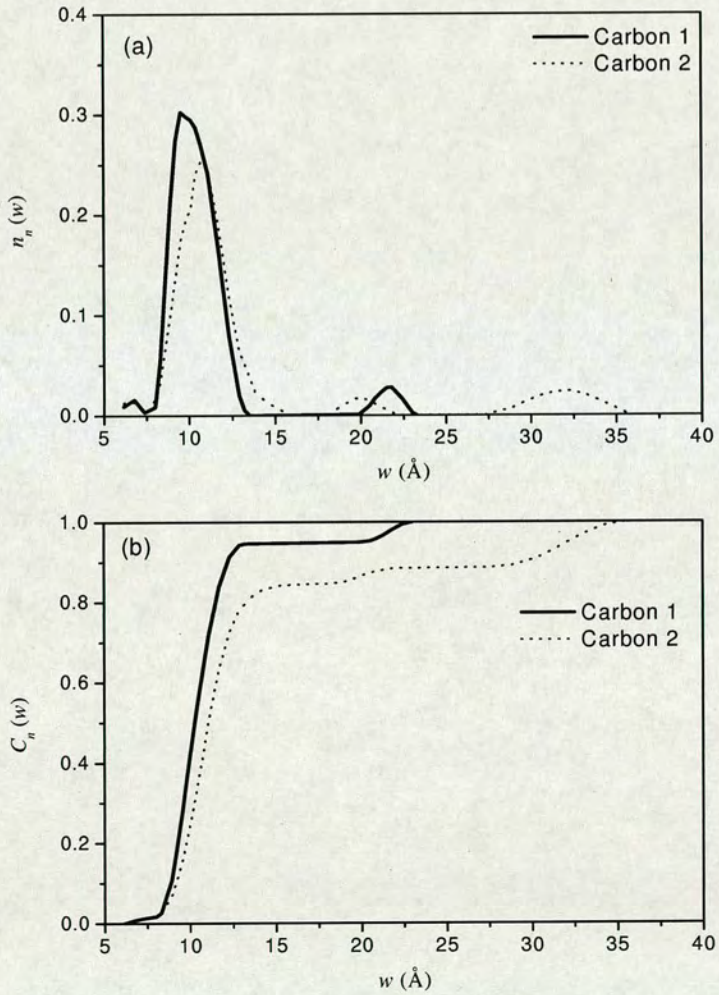

Figure 5.5 Pore size distributions of the two carbons (a) in terms of the probability density of the number of pores, (b) in terms of the corresponding cumulative probability

As we can see from Figure 5.5, the PSDs of the two carbons are different. The PSD of Carbon 1 locates most of the pores in the range of 8 – 13 Å, with a small fraction of pores in the range of 20 – 23 Å; whilst the PSD of Carbon 2 spans a larger pore size range, giving three peaks in the range of 6 – 36 Å, especially locating a considerable fraction of pores in the range of 27 – 36 Å.

5.2.1 The effect of single-pore transport diffusivities

Based on the pore network models, taking the single-pore transport diffusivities from pores with atomic walls given in Chapter 4 as input, effective transport diffusivities are calculated using REMA as described previously in Section 5.1.2. Figure 5.6 shows the effective transport diffusivities of methane in Carbon 1 and Carbon 2 for a number of pressures. As we can see, the effective transport diffusivities, D_e, increase with increasing pressure, for both Carbon 1 and Carbon 2. The effect of pressure on D_e is brought in by the single-pore diffusivities. As the single-pore diffusivities calculated in Chapter 4 increase with increasing pressure, the effective diffusivities calculated based on the single-pore diffusivities also increase with increasing pressure.

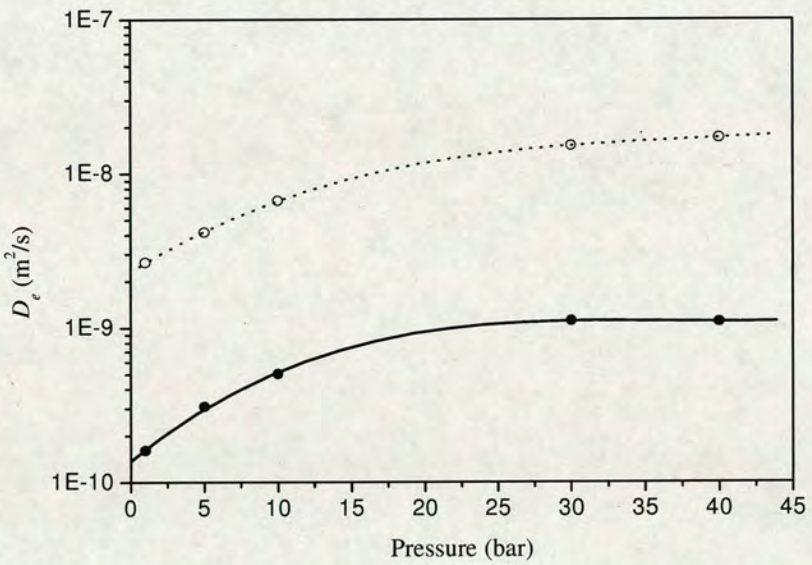

Figure 5.6 Effective transport diffusivities of methane in Carbon 1 (solid line) and Carbon 2 (dotted line).

5.2.2 The effect of the porosity

Although based on the same database of single-pore diffusivities, the effective diffusivities of Carbon 2 are much higher, about fifteen times higher than those of Carbon 1. This indicates that it is the difference between the structures of the two carbons that give different effective diffusivities. We first consider the difference between the porosity of the two carbons. It is obvious from Eq. 5.17 that the porosity influences the effective diffusivity in a way that higher porosity gives higher effective diffusivity. We know that Carbon 2 has a higher porosity ($\varepsilon_{p2} = 0.49$) than Carbon 1 ($\varepsilon_{p1} = 0.36$). Although the higher porosity of Carbon 2 results in a higher effective diffusivity, its contribution just makes the effective diffusivities of Carbon 2 about 1.3 times higher than that of Carbon 1, assuming that the other properties of the two carbons are the same. The difference introduced by the porosity is nearly negligible compared to the real gap in the effective diffusivities between the two carbons. This indicates that it is the further details of the pore network (i.e. the mean coordination number or the pore size distribution, or the combination of them) rather than the porosity play a significant role in determining the effective diffusivities. This will be discussed in the following sections. In the discussions, the effective diffusivities are reduced by the porosity, to get rid of the effect of porosity.

5.2.3 The effect of the mean coordination number

The mean coordination number $\overline{Z}$ influences the effective diffusivities as it determines the bond occupation probability p and thus influences the distribution of the conductances of the network. We investigate the region of $\overline{Z} > 1.5$ (i.e. above the percolation threshold). It is worth noting that we are using some *assumed* mean coordination numbers rather than the true value to investigate the effect of the mean coordination number on the effective diffusivity. Figure 5.7 shows the development of effective diffusivity with increasing the mean coordination number. As discussed before, the effective diffusivities shown in this figure is reduced by the porosity. As we can see, D_e/ε_p increases with increasing $\overline{Z}$ in the entire region of $\overline{Z}$ investigated, for both Carbon 1 and Carbon 2, given single-pore transport diffusivities at the pressures investigated (from 1 bar to 40 bar). The observed increase of D_e/ε_p with increasing $\overline{Z}$ is in agreement with previous work of using REMA to predict effective

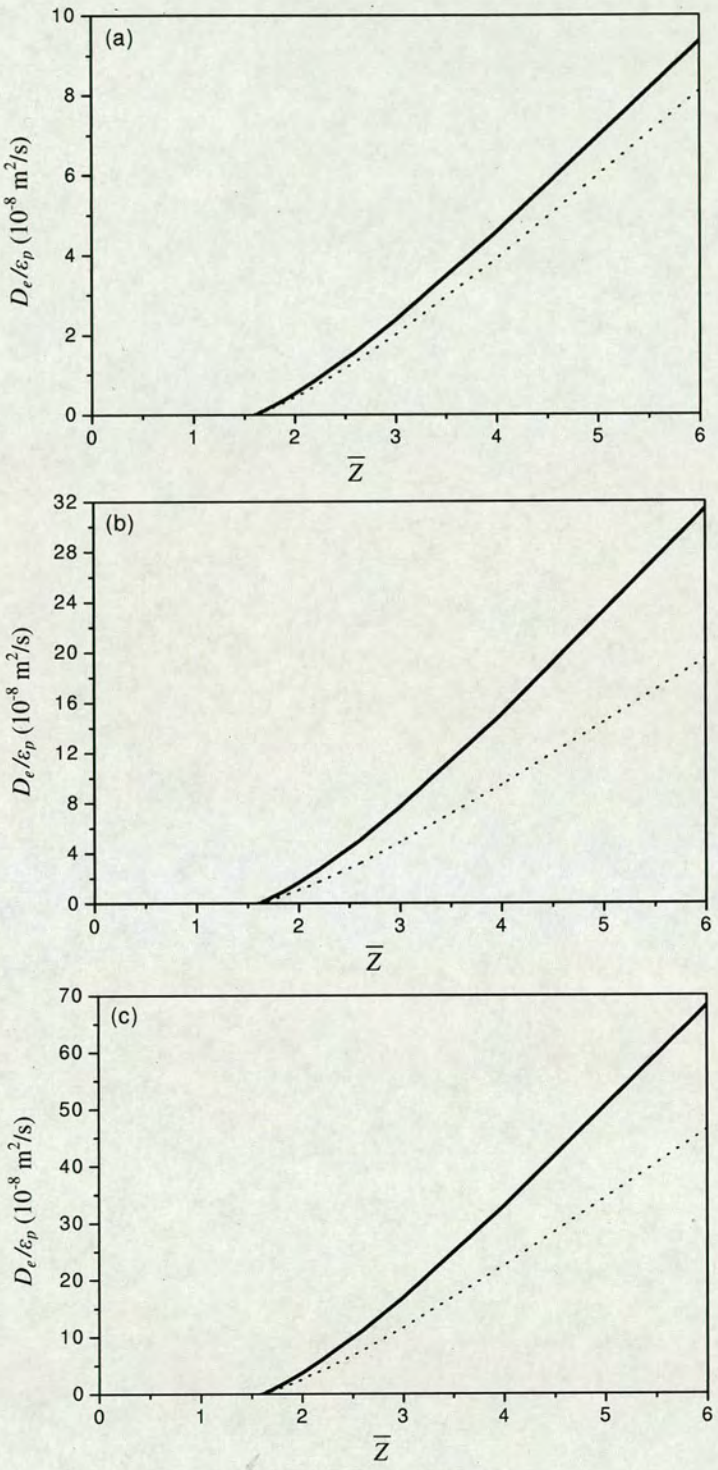

Figure 5.7 Reduced effective transport diffusivities of methane in Carbon 1 (solid lines) and Carbon 2 (dotted lines) as a function of the mean coordination number, $\overline{Z}$ at (a) 1 bar, (b) 10 bar, and (c) 40 bar.

diffusivity. Moreover, D_e/ε_p is very sensitive to $\overline{Z}$; a small change of $\overline{Z}$ gives a big change of D_e/ε_p. The above observation gives us the sense that the molecules move faster in a better connected or more open network. A higher mean coordination number $\overline{Z}$ is desired for higher effective diffusivity.

As Figure 5.7 tells us that $\overline{Z}$ has a big influence on the effective diffusivity, we assume that if the two carbons have the same $\overline{Z}$, the big gap between the effective diffusivities of the two carbons in Figure 5.6 will be smaller. We then give a comparison of D_e/ε_p of the two carbons at the same $\overline{Z}$, shown in Figure 5.8. As we have discussed at the beginning of Section 5.2, the mean coordination numbers of Carbon 1 and Carbon 2 are $\overline{Z}_1 = 1.65$ and $\overline{Z}_2 = 2.06$ respectively. We then compare the D_e/ε_p of Carbon 1 based on its own $\overline{Z}_1 = 1.65$ with the D_e/ε_p of Carbon 2 based on the assumed $\overline{Z} = 1.65$. We also compare the D_e/ε_p of Carbon 2 based on its true own $\overline{Z}_2 = 2.06$ with the D_e/ε_p of Carbon 1 based on the assumed $\overline{Z} = 2.06$. In contrast to Figure 5.6 which shows a big gap between the effective diffusivities of the two

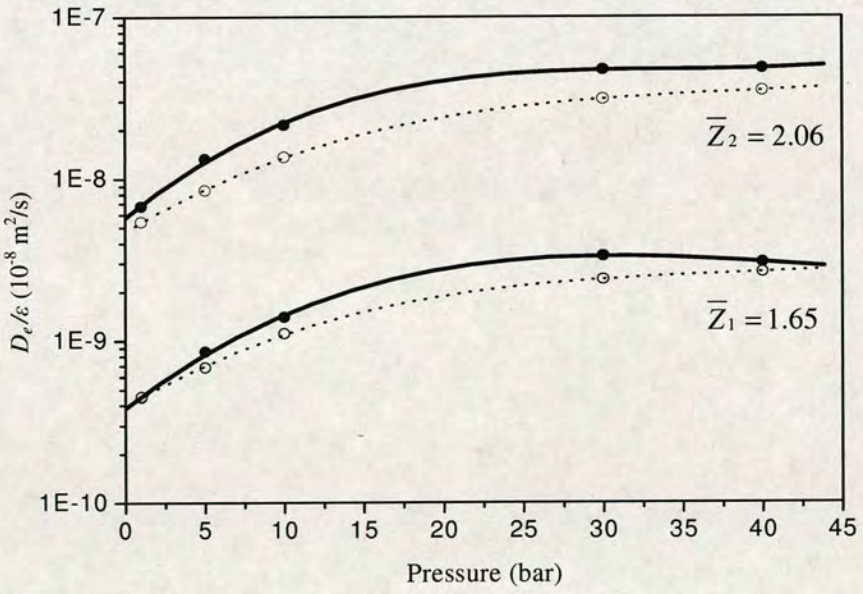

Figure 5.8 Reduced effective transport diffusivities of methane in Carbon 1 (solid lines) and Carbon 2 (dotted lines) for a number of pressures.

carbons, Figure 5.8 shows that when the two carbons have the same mean coordination number, they give very close effective diffusivities (in terms of D_e/ε_p). It is very important that this feature is captured here. It shows us that the connectivity of the pore network, in terms of the mean coordination number, plays a very important role in determining the effective diffusivity, probably much more important than any other factors.

5.2.4 The effect of the PSD

From Figure 5.8, we see that when the two pore network models have the same mean coordination number $\overline{Z}$, the reduced effective diffusivity D_e/ε_p of Carbon 1 is higher than that of Carbon 2. The only reason that can make this difference is that the two carbons have different PSDs. The influence of the PSD on the calculation of effective diffusivity using REMA is examined below.

Firstly, the PSD influences the calculation of D_e/ε_p directly by its mean pore size. Each PSD has its unique mean pore size, $\langle w \rangle$, as defined in Eq. 5.12. From Figure 5.5, we see that the PSD of Carbon 1 is narrower and has more pores in the relative small pore size range (8 – 13 Å), which gives a smaller $\langle w \rangle$, compared with Carbon 2. When using Eq. 5.17 to calculate D_e/ε_p, smaller $\langle w \rangle$ will lead to higher D_e/ε_p. However, a question should be asked here: can the higher D_e/ε_p of Carbon 1 be totally attributed to its smaller $\langle w \rangle$? The answer is that it does not. This will be explained in the following discussions.

Secondly, the PSD was introduced in the first place to build the pore network model. The PSD determines directly the pore sizes that are assigned to the occupied bonds in the network, and thus decides indirectly the conductance distribution in the network. The conductance distribution in the network then determines the effective conductance, g_e', which is used in Eq. 5.17 for calculating D_e. Figure 5.9 gives the comparison of g_e' for Carbon 1 and Carbon 2. Note that in Figure 5.7, we compared D_e/ε_p of the two carbons, in which the influence of both $\langle w \rangle$ and g_e' were included; whilst the comparison of g_e' gets rid of the influence of $\langle w \rangle$ and reveals how a PSD

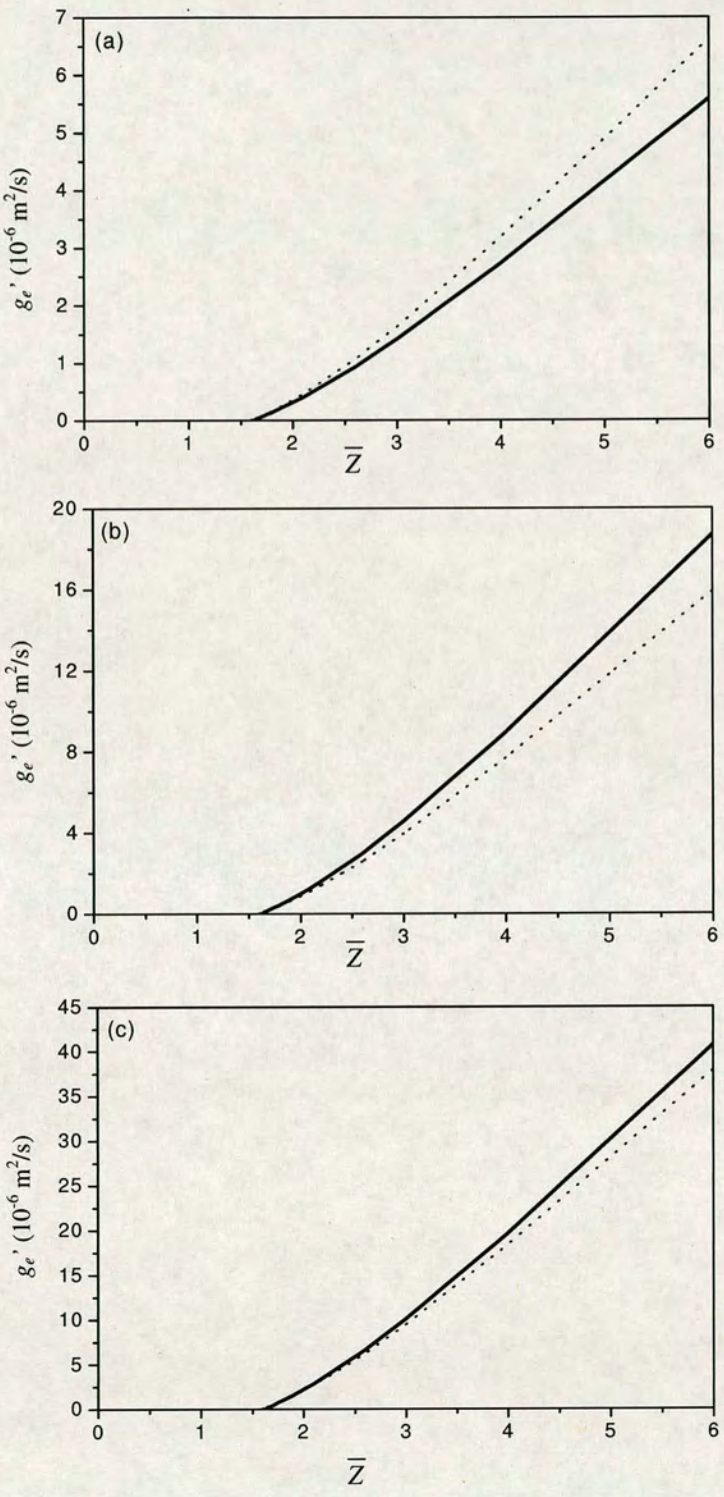

Figure 5.9 g_e' of the pore networks of Carbon 1 (solid lines) and Carbon 2 (dotted lines) at (a) 1 bar, (b) 10 bar, and (c) 40 bar.

is related to g_e' from the network. Interestingly, Figure 5.9 shows that at low pressure (P = 1 bar), Carbon 2 gives higher g_e' than Carbon 1; while at higher pressures (P = 10 bar and 40 bar), g_e' from Carbon 1 is higher than that from Carbon 2. It makes sense when we look at the single-pore transport diffusion coefficients at these pressures. As shown in Figure 5.10, the transport coefficients, D_t, at P = 1 bar basically increase with increasing the pore size, that is, higher transport coefficients are found in bigger pores. So, if bigger pore sizes are assigned to a considerable number of the occupied bonds of the network, the network will have a conductance distribution which includes a considerable number of high conductances. In this case, the effective conductance of the network, g_e', calculated from Eq. 5.14, will be higher. As the PSD of Carbon 2 has a considerable number of pores located at a bigger pore size range (27 – 36 Å) which does not appear in the PSD of Carbon 1, the effective conductance of Carbon 2 is higher than that of Carbon 1. However, at higher pressures, the transport coefficients in the smaller pores (7 – 15 Å) are higher, as shown in Figure 5.10. In this case, if the PSD of the network locates most of the pores at this pore size range, the network will have a conductance distribution which

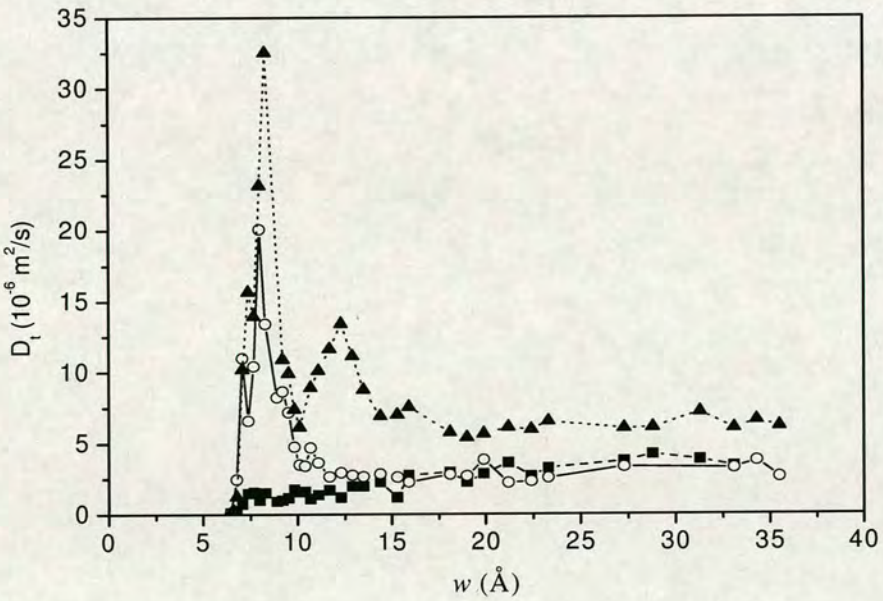

Figure 5.10 Single-pore transport coefficients at 1 bar (squares), 10 bar (circles) and 40 bar (triangles).

includes a large number of high conductances, thus will give high effective conductance. This is why the effective conductance of Carbon 1 is higher than that of Carbon 2 at higher pressures (P = 10 bar and 40 bar), as shown in Figure 5.9. We conclude that g_e' (and thus the effective diffusivity) depends strongly on the distribution of pore sizes.

The above discussion is based on two "experimentally" determined PSDs. We also investigate the case of more general PSDs, using the lognormal PSD. A lognormal PSD takes the form:

$$f(w) = \frac{1}{\sqrt{2\pi}\sigma w} \exp\left[-\frac{(\ln w - \mu)^2}{2\sigma^2} \right] \tag{5.18}$$

where σ is the shape parameter that decides the shape of the PSD and μ is the location parameter. The mean, m, and the standard deviation, s, of the distribution are given by

$$m = e^{(\mu + 0.5\sigma^2)} \tag{5.19}$$

$$s = (e^{(2\mu + 2\sigma^2)} - m^2)^{1/2} \tag{5.20}$$

Note that Eq. 5.18 is a probability density function. By changing σ and μ, we can get various PSDs with different shapes and different ranges of pore size. In this work, we set σ = 0.1, 0.5, 2.0. The PSDs with different σ values are of very different shapes. All the PSDs are set to start from the pore size of 6 Å, below which pores are too small to accommodate methane molecules. μ is increased from 2.32 to 2.93 to give five PSDs with different pore-size ranges.

Figure 5.11 shows type σ = 0.1 PSDs of different pore-size ranges. These five PSDs are about symmetrical to 10.0 Å, 12.4 Å, 14.4 Å, 16.4 Å and 18.8 Å respectively as shown in Figure 5.11 (a). The pores that have non-negligible fraction centre around the peaks to give narrow PSDs in the range of 7.5 – 13.5 Å for PSD 11, 9.0 – 16.0 Å for PSD 12, 10.5 – 19.0 Å for PSD 13, 12.0 – 21.0 Å for PSD 14 and 14.0 – 25.0 Å for PSD 15. Corresponding to these five narrow PSDs, Figure 5.11 (b) shows very steep probability density function of cumulative number of pores.

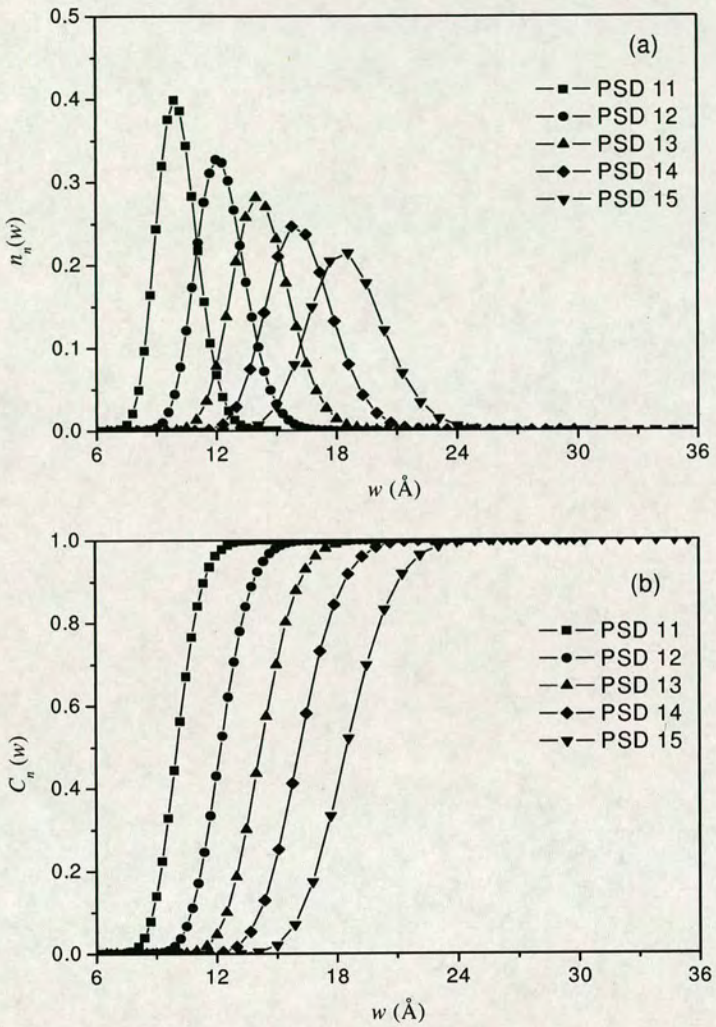

Figure 5.11 Type σ = 0.1 PSDs of different pore-size ranges. (a) in terms of the probability density of number of pores, (b) in terms of the probability density of cumulative number of pores.

Figure 5.12 shows type σ = 0.5 PSDs of different pore-size ranges. Compared with type σ = 0.1 PSDs shown in Figure 5.11, type σ = 0.5 PSDs are broader; the pores that have non-negligible fraction distribute in the range of 6 – 15 Å for PSD 51, 6 – 20 Å for PSD 52, 6 – 25 Å for PSD 53, 6 – 30 Å for PSD 54 and 6 – 35 Å for PSD 55. These PSDs show peaks which are very close to each other, basically around 10 Å.

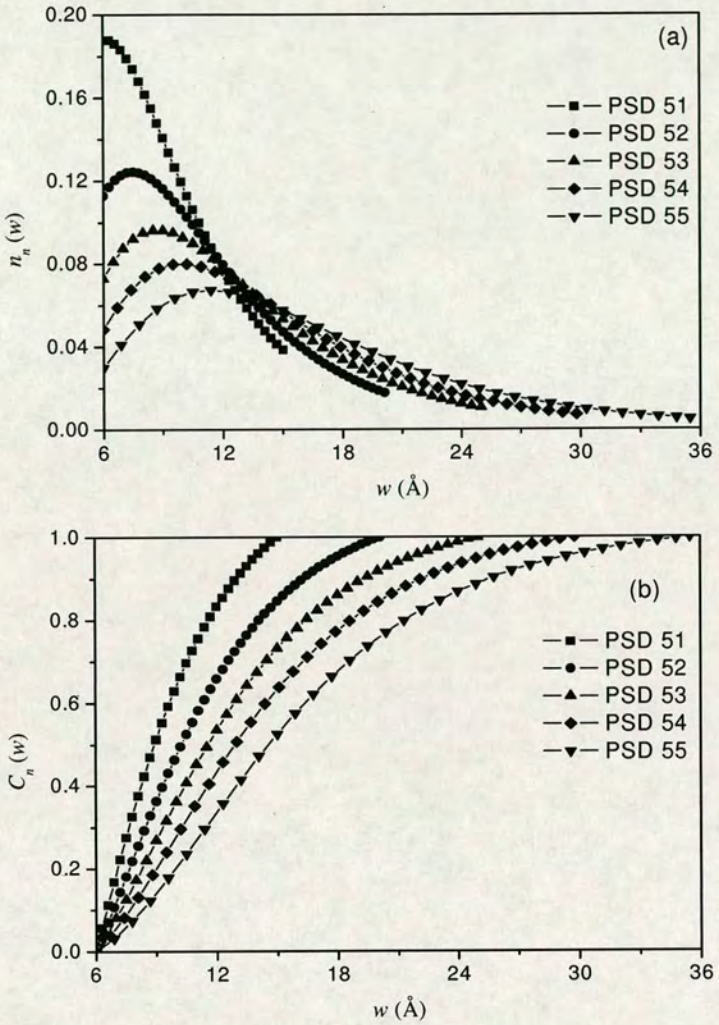

Figure 5.12 Type σ = 0.5 PSDs of different pore-size ranges. (a) in terms of the probability density of number of pores, (b) in terms of the probability density of cumulative number of pores.

Figure 5.13 shows type σ = 2.0 PSDs of different pore-size ranges. These PSDs also have broad distributions; the pores that have non-negligible fraction distribute in the range of 6 – 15 Å for PSD 21, 6 – 20 Å for PSD 22, 6 – 25 Å for PSD 23, 6 – 30 Å for PSD 24 and 6 – 35 Å for PSD 25. However, these PSDs are different from those shown in Figure 5.12 as their peaks locate at the same position - the starting pore size of 6 Å.

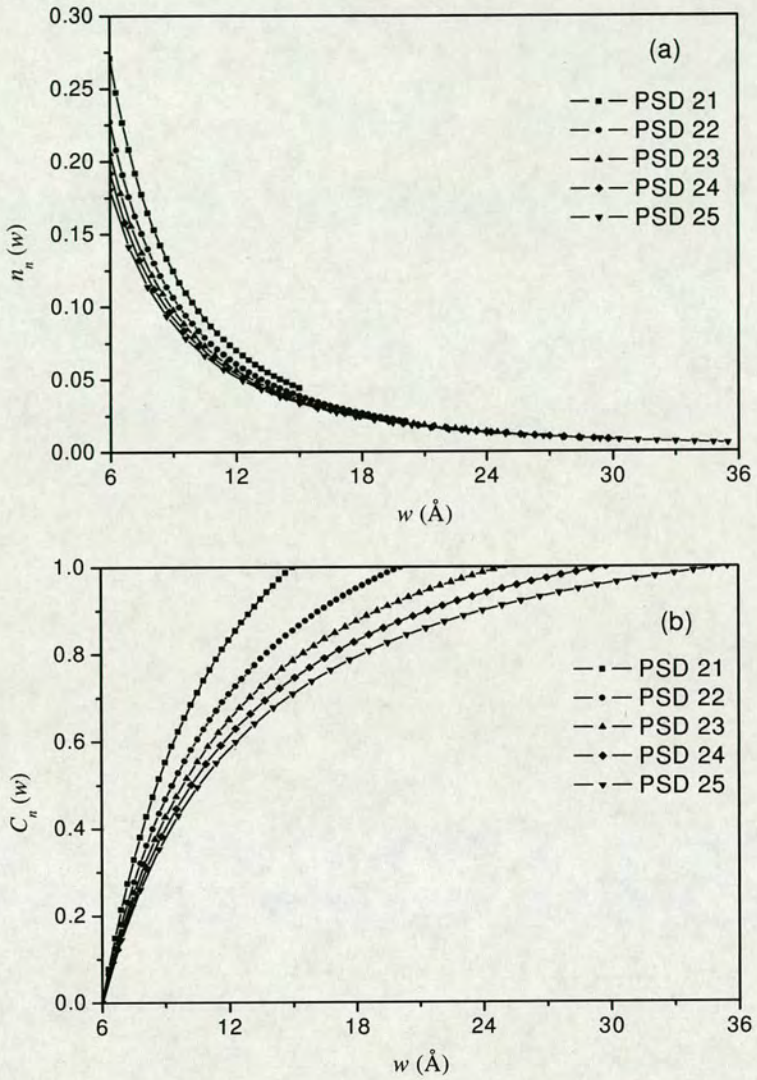

Figure 5.13 Type σ = 2.0 PSDs of different pore-size ranges. (a) in terms of the probability density of number of pores, (b) in terms of the probability density of cumulative number of pores.

The PSDs shown in Figure 5.11-5.13 are used to build up different network models. The single-pore transport diffusion coefficients at P = 30 bar, given in Figure 5.14, are used as the input to the networks. By comparing the effective conductances g_e' and the reduced effective diffusivities D_e/ε_p from different network models, we are

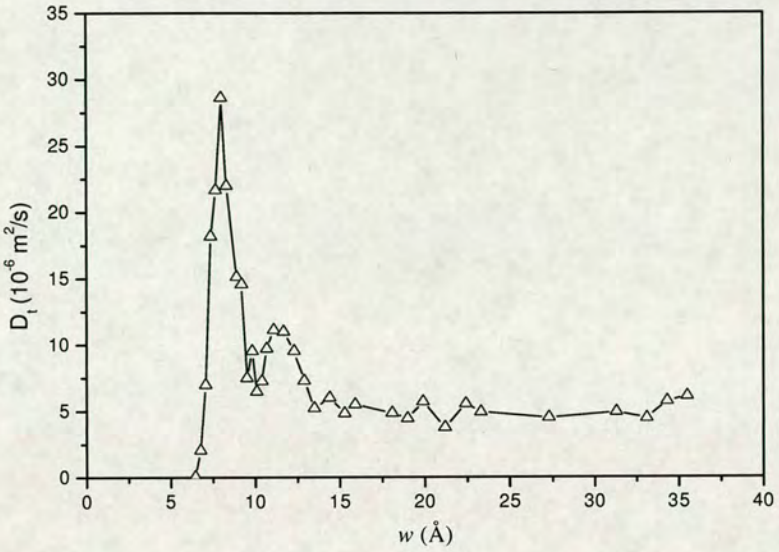

Figure 5.14 Single-pore transport diffusion coefficients of methane at 30 bar.

trying to find out how different PSDs influence these values. Figure 5.15 and 5.16 show respectively g_e' and D_e/ε_p from the networks which are based on different PSDs. Note that PSDs with different pore-size ranges are investigated for all the three types of PSDs (i.e. σ = 0.1, 0.5, 2.0). Comparing Figure 5.15 with Figure 5.16 shows that the mean pore size <w> has considerable influence. A smaller pore-size range gives a smaller <w>, leading to a higher D_e/ε_p (according to Eq. 5.17). The differences between the D_e/ε_p that are based on PSDs of different pore-size ranges are bigger, compared with that of g_e'.

From Figure 5.15 and 5.16, we can see that different types of PSDs behave differently to give the effective diffusivity. For PSDs of σ = 0.1 type, PSD 11 is desirable; the network based on this PSD gives the highest D_e/ε_p and g_e' in the entire region of $\overline{Z} > 1.5$, as shown in Figure 5.15 (a) and 5.16 (a). This is because this PSD includes only the pores (7.5 – 13.5 Å) that carry the highest transport coefficients. PSD 13 and PSD 15 actually place most of their un-negligible pores in the range of 10.5 – 19.0 Å and 14.0 – 25.0 Å. Transport coefficients in these pores are very close,

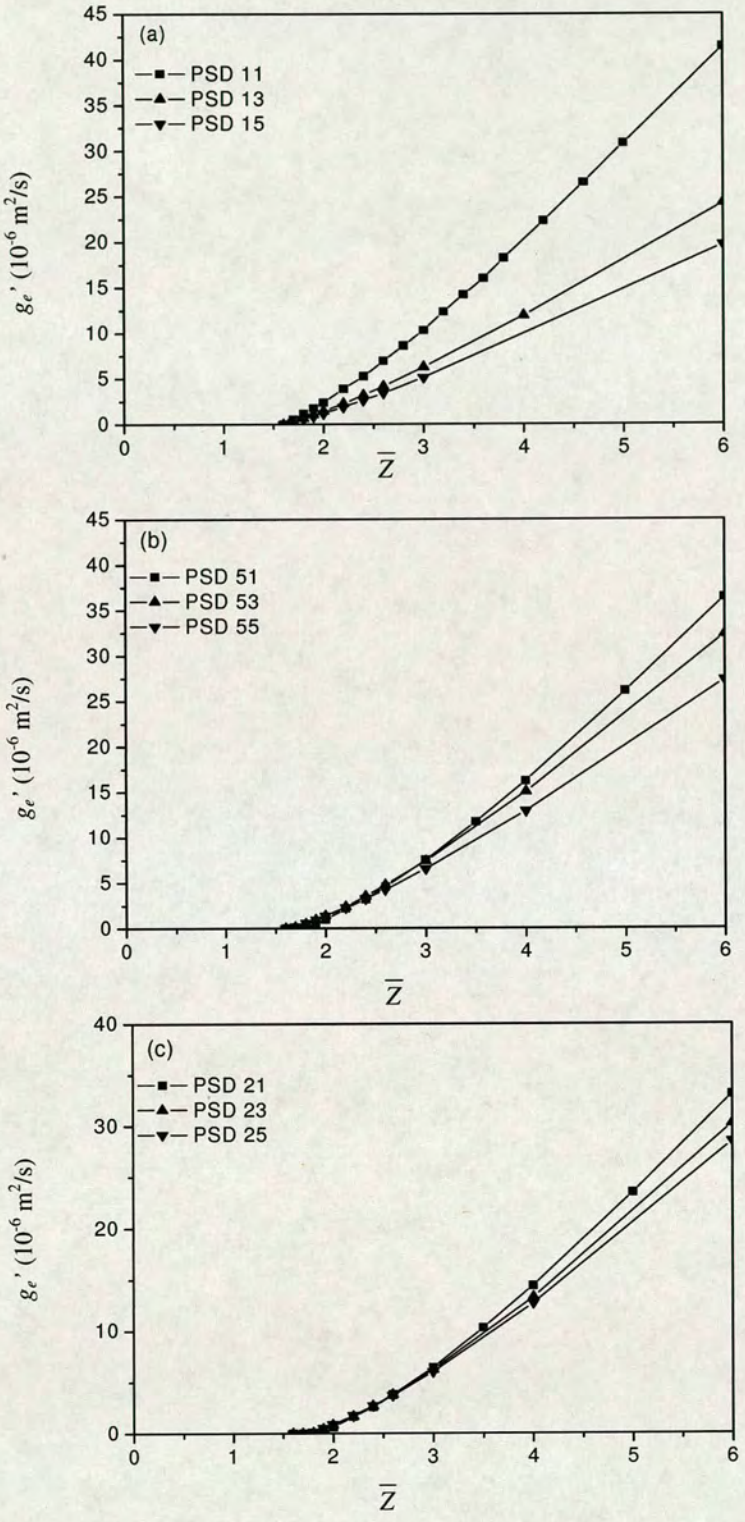

Figure 5.15 g_e' of the pore networks based on the PSDs of (a) σ = 0.1, (b) σ = 0.5, and (c) σ = 2.0. The symbols indicate PSDs that correspond to Figure 5.11-5.13.

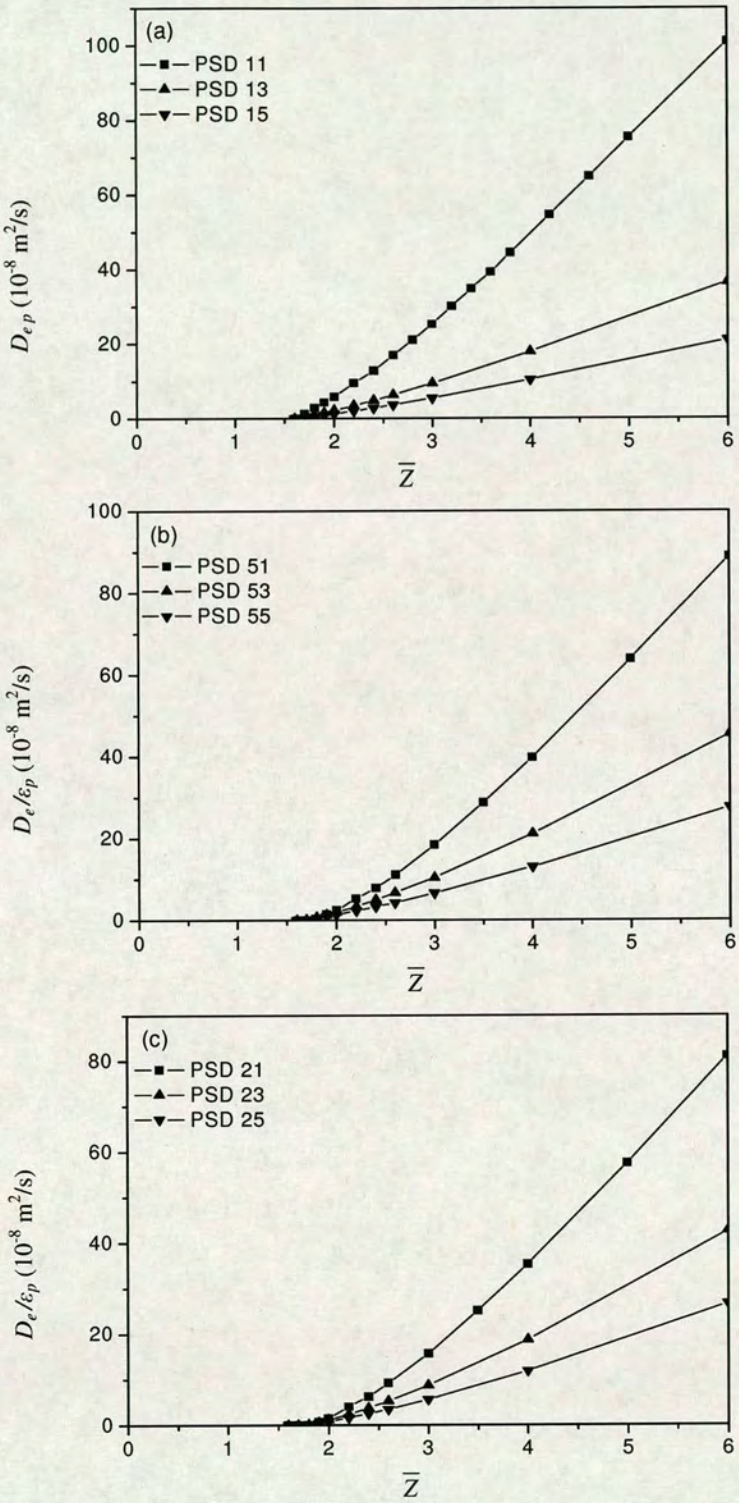

Figure 5.16 D_e/ε_p of the networks based on the PSDs of (a) $\sigma = 0.1$, (b) $\sigma = 0.5$, and (c) $\sigma = 2.0$. The symbols indicate PSDs that correspond to Figure 5.11-5.13.

which makes the g_e' from the networks based on these two PSDs closer, compared with that based on PSD 11. The networks based on PSDs of type $\sigma = 0.5$ and $\sigma = 2.0$ in the smaller pore-size ranges (i.e. PSD 51 and PSD 21) also give higher D_e/ε and g_e' in the entire region of $\overline{Z} > 1.5$, as shown in Figure 5.15 and 5.16.

We conclude the summary from the above discussion regarding the role of the PSD in determining the effective diffusivity. If higher effective transport diffusivity in the pore network of the material is desirable, the materials should have a narrow PSD around the pore size that has the highest diffusion coefficient.

5.3 Evaluation of the Hybrid MD/PNM Approach

The main goal of this thesis is to evaluate the reliability of the hybrid MD/PNM approach for predicting the effective diffusivity in nanoporous carbons. In Chapter 2 and 3, the PSD and the pore network connectivity (i.e. the mean coordination number $\overline{Z}$) were obtained, and so the PNM was built. In Chapter 4, the database of the single-pore transport diffusivities were constructed using MD simulations. In this chapter, we have shown how the single-pore transport diffusivities are incorporated to the PNM to predict the effective diffusivities in the two carbons. We have also discussed the factors that influence the predicted effective diffusivity, giving the information for materials design. However, before the hybrid MD/PNM approach can be taken to the industry for practical applications, a very important question needs to be answered: Is the hybrid MD/PNM approach reliable at all? (Or, can we believe the results?) In this section, we are evaluating the reliability of the hybrid MD/PNM approach by comparing its predicted effective diffusivity against the "true" effective diffusivity of the two carbons.

Figure 5.17 compares the effective diffusivity predicted from the hybrid MD/PNM approach (termed as PNM-D_e), with the "true" effective diffusivity which is determined directly from VPC by carrying out molecular dynamics simulation through the solids (termed as VPC-D_e)[157] for a number of pressures. This figure

shows that the predicted coefficient (PNM-D_e) is in very good agreement with the actual coefficient (VPC-D_e) both quantitatively and qualitatively, for both Carbon 1 and Carbon 2. This agreement is in a wide range of pressures (from 1 bar to 40 bar). Moreover, the development of PNM-D_e with increasing pressure shows a very similar trend with the variation of VPC-D_e with pressure. This is strong evidence that the hybrid MD/PNM approach is reliable enough for predicting the effective diffusivity in porous media. Thus this approach can be put in industry for prediction purposes.

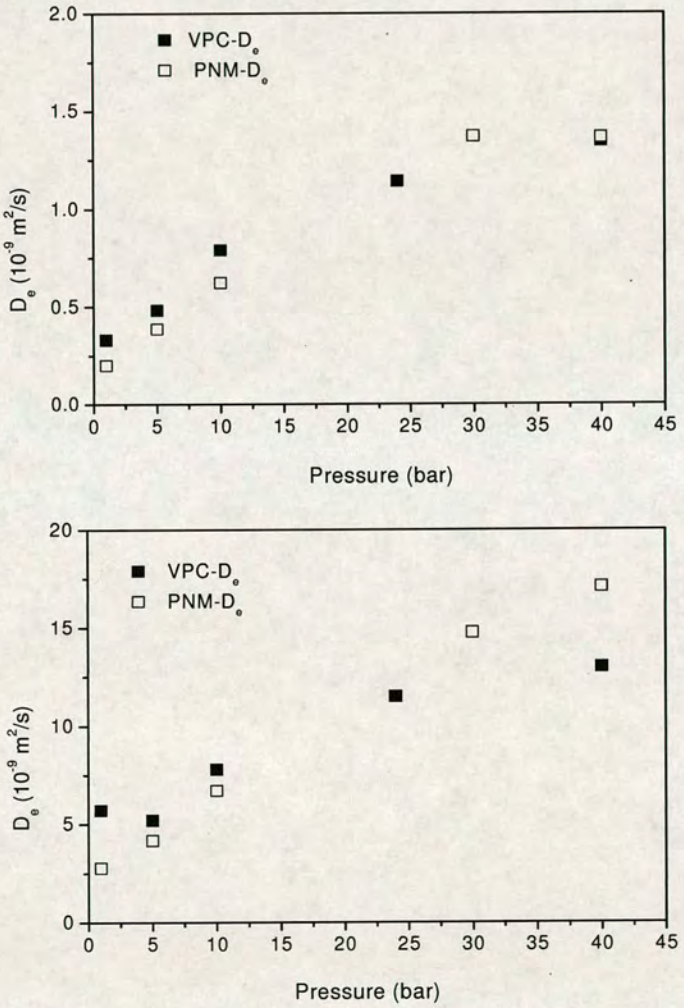

Figure 5.17 Comparison of the effective transport coefficients of methane predicted by the hybrid MD/PNM method with the actual coefficient for the two VPCs (a) Carbon 1 and (b) Carbon 2.

Some discrepancy can be seen between the PNM-D_e and the VPC-D_e. For Carbon 1, the PNM-D_e has excellent agreement with the VPC-D_e at extremely high pressure but smaller than the VPC-D_e at low pressures. For Carbon 2, the PNM-D_e over-predicts the VPC-D_e at extremely high pressure but under-predicts the VPC-D_e at low pressure. This can be explained as follows. The only way in which pressure can influence the diffusion coefficient predicted from the hybrid MD/PNM method is via the single-pore transport coefficients. Consideration of how these vary with pressure and pore size along with the discrepancies between the geometric and adsorption-derived PSDs indicates, at least in part, the reason why the transport coefficients determined from the hybrid MD/PNM are not more correct at the extremes of the pressure range considered. At the low pressure end, the smaller pores in the PNM will carry the vast majority of the flux. As Figure 2.20 in Chapter 2 shows, however, the number of these pores will be less than in reality because some of the porosity has been incorrectly assigned to larger pores (that do not exist in reality). This combined with the fact that the transport diffusion coefficient at low pressure *increases* monotonically with pore size, shown in Figure 5.10, explains why the hybrid MD/PNM under-predicts the diffusion coefficient at low pressures. At high pressures, on the other hand, the larger pores carry a significant amount of flux but, as Figure 5.8 shows, their transport diffusion coefficients are somewhat less than those of the smaller pores in general, including particularly those pores which are missing from the adsorption-derived PSD. Combined with that the adsorption-derived PSD include a considerable number of pores in large pore size range (especially for Carbon 2), this explains why the hybrid MD/PNM over-predicts the diffusion coefficient at high pressures for Carbon 2. Because the PSD of Carbon 1 does not include so many pores in large pore size range and show better agreement with the geometrical PSD, as shown in Figure 2.20, the PNM-D_e gives better agreement especially at high pressure. The above discussion reveals that the correctness of the adsorption-derived PSD is important in predicting the effective diffusion coefficient. The adsorption-derived PSD, though it does not completely grasp the "true" structure, predicts the effective diffusivities that are only in minor discrepancy with the actual values. This, together with that the adsorption-derived PSD gives excellent prediction of adsorption (shown in Chapter 2), is strong support

of the use of the pore network model to characterize the structure of nanoporous carbons by physical adsorption.

The correctness of the adsorption-derived mean coordination number $\overline{Z}$ is also examined. Assumed slightly different mean coordination numbers are used to predict the effective diffusivities from the hybrid MD/PNM method. These predicted effective diffusivities are then compared with the actual effective diffusivities of the two carbons, and with the predicted effective diffusivities based on $\overline{Z}_1 = 1.65$ for Carbon 1 and $\overline{Z}_2 = 2.06$ for Caron 2 as determined in Chapter 3. As shown in Figure 5.18, even slightly different coordination numbers give very different PNM-coefficients which are in big discrepancy with the VPC-coefficients. The PNM-coefficients based on the assumed slightly different $\overline{Z}$ also show big discrepancy with the PNM-coefficients based on the exactly determined $\overline{Z}$. This is strong evidence that the mean coordination numbers obtained using the combined adsorption/percolation method given in Chapter 3 are basically correct in predicting the effective diffusivity. We also learn that it is very important to measure $\overline{Z}$ and to get it "right". (Note that the argument "$\overline{Z}$ is right" is in the sense of giving reliable prediction of the effective diffusivity, not in the sense of a direct comparison with a real value, as it is impossible to obtain a well-defined $\overline{Z}$ in a real carbon (or VPC).)

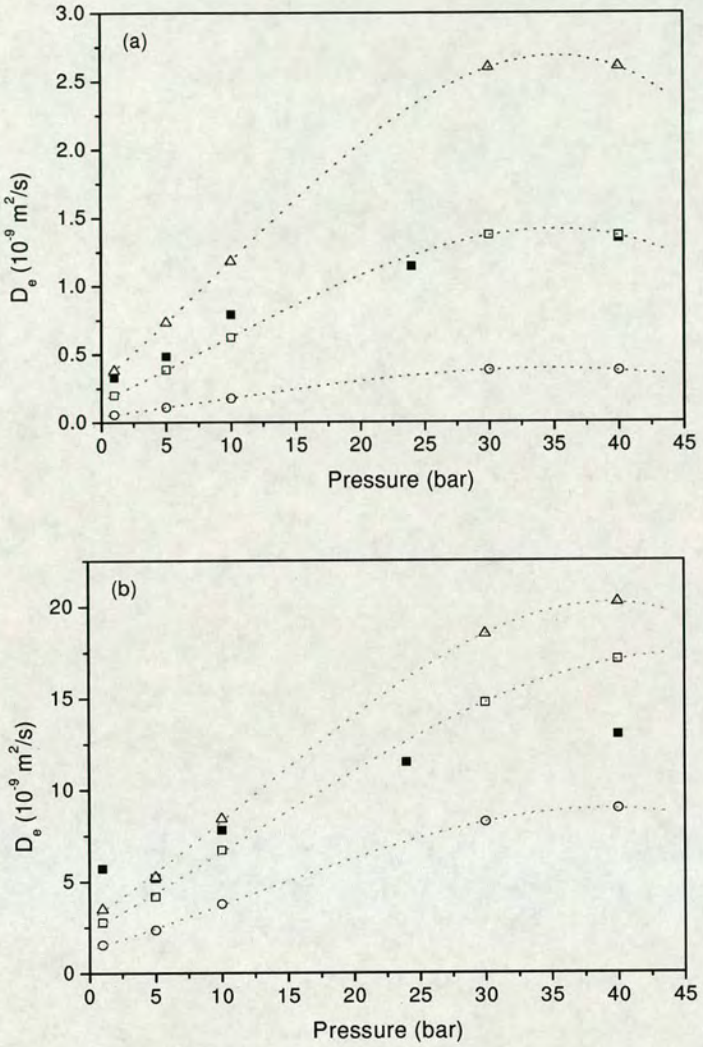

Figure 5.18 Comparison of the effective transport coefficients of methane predicted by the hybrid MD/PNM method with the actual coefficient for the two VPCs (a) Carbon 1 and (b) Carbon 2. Filled squares indicate the actual coefficient for the VPC. Empty squares indicate the coefficients predicted by the MD/PNM method, with the determined (as shown in Chapter 3) $\overline{Z}_1 = 1.65$ for Carbon 1 and $\overline{Z}_2 = 2.06$ for Caron 2 respectively. Empty circles indicate the coefficients predicted by the MD/PNM method, with the assumed $\overline{Z}_1 = 1.63$ and $\overline{Z}_2 = 1.9$ for Carbon 1 and Cabon 2 respectively. Empty triangles indicate the coefficients predicted by the MD/PNM method, with assumed $\overline{Z}_1 = 1.70$ and $\overline{Z}_2 = 2.2$ for Carbon 1 and Caron 2 respectively. The dotted lines are to guide the eye.

5.4 Summary

In this chapter, the hybrid MD/PNM method is used to predict the effective diffusion coefficient for the VPC, using the REMA approach. The PNM is built based on the adsorption-derived PSD for the VPC (also called PNM-PSD), shown in Figure 2.15 and 2.18 in Chapter 2, and the mean coordination number $\overline{Z}$ obtained in Chapter 3 based on the adsorption/percolation approach. The single-pore transport diffusion coefficients, obtained in Chapter 4 using MD simulation with atomic walls, are then incorporated with the PNM using the REMA approach to obtain the effective diffusion coefficient.

We have identified, for the purpose of designing materials, the factors that influence the effective diffusion coefficient. First of all, a high porosity of the solid is desired for obtaining a high coefficient. Second, the connectivity of the pore network, in terms of the mean coordination number, plays an important role in determining the effective diffusion coefficient; the effective diffusion coefficient increases largely with increasing mean coordination number, especially in the region that is close to the percolation threshold. Third, the PSD influences the effective diffusion coefficient in a way that if most of the pores included in the PSD carry high transport diffusivities, the effective diffusion coefficient is going to be high as well; the effective diffusion coefficient will be lowered if some pores that carry low transport diffusivities are included in the PSD. Thus a narrow PSD with most of the pores carrying high transport coefficients is always better to give high effective diffusivity.

The predicted effective diffusion coefficient by the hybrid MD/PNM method is then compared with the actual coefficient from the VPC. The good agreement between the PNM-coefficient and the VPC-coefficient indicate the reliability of the hybrid MD/PNM method. The comparison also shows that the correctness of the adsorption-derived PSD has a considerable contribution to the correctness of the PNM-coefficient. Moreover, the effective diffusion coefficient is very sensitive to the mean coordination number and the mean coordination number obtained by the combined adsorption/percolation approach is basically correct in terms of predicting reliable effective diffusivity.

6. Conclusions and Future Work

The main accomplishment of this thesis highlights the usefulness of the hybrid MD/PNM approach for predicting the effective diffusion coefficient in nanoporous carbons. On the one hand, the pore network model (PNM), which is a relatively simple model to represent the structure of nanoporous carbons, was built from the characteristics (both geometrical and topological) obtained using the conventional characterization methods based on physical adsorption. On the other hand, molecular dynamics (MD) simulation is used to give insights into the mechanism of diffusion in carbon nanopores and provide the single-pore diffusion coefficients that were input to the PNM, whereby the effective diffusion coefficient in the whole solid was determined. Features that describe the real systems are thus brought in by the PNM and MD, and so the hybrid MD/PNM is able to predict the effective diffusivities for real systems (i.e. in real carbons).

The thesis also provides a way for evaluating the reliability of the hybrid MD/PNM approach, by replacing the real carbons in the lab with the computer-generated, and highly realistic, virtual porous carbons (VPC) with which the structure of the carbons and the effective diffusivity in the carbons can be exactly known. This has enabled us to evaluate the conventional characterization methods for obtaining the structure (particularly, the PSD and the pore network connectivity) of nanoporous carbons. The physical adsorption-based PSD showed very good prediction of adsorption, whilst it also showed the discrepancy compared with the "real" structure. However, the discrepancy of the adsorption-based PSD does not hinder its usefulness for predicting both adsorption and the effective diffusion. The correctness of the pore network connectivity characteristic (in terms of the mean coordination number) was also demonstrated: the predicted effective diffusivity is very sensitive to the mean coordination number and the mean coordination numbers obtained are basically correct in terms of giving good prediction of the effective diffusivity. The good agreement between the predicted effective diffusivity from the hybrid MD/PNM and the "true" values from the VPC is strong evidence that the hybrid MD/PNM approach is reliable enough for predicting the effective diffusivity in nanoporous

carbons. This supports the use of the hybrid MD/PNM for predicting the effective diffusivity in industry for practical applications.

A distinct advantage of the MD/PNM approach is that it is relatively straightforward to apply. The single-pore adsorption isotherms can be easily obtained using the developed GCMC program and stored in a database for future use. Given only the adsorption isotherms measured on the material, both the geometrical and topological characteristics of the material can be obtained by routine analysis. Once the single-pore diffusion data has been determined using MD simulations and stored in a database for future use, an effective diffusion coefficient can be predicted for the material using the developed REMA program in a matter of several minutes. Thus the effective diffusion coefficients of various species (e.g. a series of hydrocarbons from CH_4 to C_4H_{10}) at different temperatures and at different pressures can be thoroughly and easily investigated in a wide range of nanoporous carbons, by only changing the input parameters to these programs. Therefore, the influence of a wide range of factors (e.g. temperature, pressure, molecular size and shape) on the effective diffusion can be investigated. This is a natural extension of the work presented in this thesis.

Another advantage of using the hybrid MD/PNM approach is that it provides a direct link between the molecular-level internal structure and the macroscopic properties. The molecular-level description of the materials depends on the systems requirement and more aspects of the materials can be added to the model. It is thus straightforward to improve the model for the materials in order to have a more realistic description of the systems. For example, water (or other strongly polar species, e.g. volatile organic compounds) adsorption and diffusion can be more realistically described, with the inclusion of the chemical heterogeneity of nanoporous carbons by presenting the polar groups on the surface of the pore walls.[72] Moreover, in real applications, it often involves multi-component species, in which diffusion and separation of mixtures are of interests. The effective diffusion of multi-species in such systems can also be predicted using the hybrid MD/PNM approach. This can be an important area of future research. In this context, the computational

effort involved in the MD simulations will be relatively large (compared to the simulation of single non-polar species). However, the rapid rate of improvement in computer power, as well as in the development of simulation techniques, opens good prospects for the widespread use of molecular simulation methods and the difficulties will be overcome.

As the PNM provides a means of linking topological and geometrical characteristics of a porous solid to its transport behaviour, the MD/PNM approach provides a great tool for materials design for their applications in which transport diffusion of guest species is of importance. We have demonstrated in Chapter 5 that for the purpose of materials design, a solid with a high porosity, a narrow PSD which has most of the pores carrying high transport diffusion coefficients, and a high mean coordination number which indicates a well connected pore network, is desirable for obtaining a high effective diffusivity. This is rather general.

The hybrid MD/PNM also allows linking the porous structure to the specific value of the effective diffusivity, and so designing the materials for the particular application where the effective diffusivity needs to be exactly known. The design of materials lies in two-folds. On the one hand, its flexibility allows for an accurate description of complex and highly non-ideal systems and thus can be applied to predict the effective diffusivity in a hypothetical structure. On the other hand, the desired properties (e.g. the desired values of the effective diffusivity) can be input to the MD/PNM process whereby the output is the required structure of the material. These provide crucial information for the design of new, "tailor-made", materials for particular applications – those that may be (?!) more obvious to society include improved mobile phone battery life and better drug delivery devices.

7. References

1. Rouquerol, J.; Avnir, D.; Fairbridge, C. W.; Everett, D. H.; Haynes, J. H.; Pernicone, N.; Ramsay, J. D. F.; Sing, K. S. W.; Unger, K. K., Recommendations for the characterization of porous solids. In *Pure & Applied Chemistry*, 1994; Vol. 66, pp 1739.
2. Mays, T. J. In *A new classification of pore sizes*, Charaterization of Porous Solids VII, 2005; Llewellyn, P. L.; Rodriquez-Reinoso, F.; Rouqerol, J.; Seaton, N., Eds. Elsevier: 2005; pp 57.
3. Marsh, H.; Rodriguez-Reinoso., F., *Activated carbon*. Elsevier: Oxford, 2006.
4. Bansal, R. C.; Goyal, M., *Activated carbon adsorption*. Taylor & Francis Group: USA, 2005.
5. Cai, Q.; Huang, Z. H.; Kang, F. Y.; Yang, J. B., Preparation of activated carbon microspheres from phenolic-resin by supercritical water activation. *Carbon* **2004,** 42, 775.
6. Talu, O.; Sun, M. S.; Shah, D. B., Diffusivities of n-alkanes in silicalite by steady-state single-crystal membrane technique. *AIChE Journal* **1998,** 44, 681.
7. Shah, D. B.; Ruthven, D. M., Measurement of zeolites diffusivities and equilibrium isotherm by chromatography. *AIChE Journal* **1977,** 23, 804.
8. Yasuda, Y., Determination of vapour diffusion coefficients in zeolite by the frequency response method. *Journal of Physical Chemistry* **1982,** 86, 1913.
9. Bae, J. S.; Do, D. D., Surface diffusion of strongly adsorbing vapours in activated carbon by a differential permeation method. *Chemical Engineering Science* **2003,** 58, 4403.
10. Prasetyo, I.; Do, D. D., Adsorption rate of methane and carbon dioxide on activated carbon by the semi-batch constant molar flow rate method. *Chemical Engineering Science* **1998,** 53, 3459.
11. Mugge, J.; Bosch, H.; T. Reith, Measuring and modelling gas adsorption kinetics in single porous particles. *Chemical Engineering Science* **2001,** 56, 5351.

12. Sun, M. S.; Talu, O.; Shah, D. B., Diffusion measurements through embedded zeolite crystals. *AIChE Journal* **1996,** 42, 3001.

13. Heink, W.; Kärger, J.; Pfeifer, H.; Seiffert, G., High-temperature pulsed field gradient nuclear magnetic resonance self-diffusion measurement of n-alkanes in MFI-type zeolites. *J. Chem.Soc. Farad.Trans.* **1992,** 88, 3505.

14. Jobic, H.; Schmidt, W.; Krause, C. B.; Kärger, J., PFG NMR and QENS diffusion study of n-alkane homologues in MFI-type zeolites. *Microporous and Mesoporous Materials* **2006,** 90, 299.

15. Jobic, H.; Bee, M.; Caro, J.; Bülow, M.; Kärger, J., Molecular self-diffusion of methane in zeolite ZSM-5 by quasi-elastic neutron scattering and nuclear magnetic resonance pulsed field gradient technique. *J. Chem.Soc. Farad.Trans.* **1989,** 85, 4201.

16. Papadopoulos, G. K.; Jobic, H.; Theodorous, D. N., Transport diffusivity of N2 and CO2 in silicalite: coherent quasielastic neutron scattering measurements and molecular dynamics simulations. *J. Phys. Chem. B* **2004,** 108, 12748.

17. Kärger, J.; Ruthven, D., Diffusion in Zeolites and Other Microporous Materials. In John Wiley & Sons: New York, 1992.

18. Mota, J. P. B.; Rodrigues, A. E.; Saatdjian, E.; Tondeur, D., Dynamics of natural gas adsorption storage systems employing activated carbon. *Carbon* **1997,** 35, 1259.

19. Saghafi, A.; Faiz, M.; Roberts, D., CO2 storage and gas diffusivity properties of coals from Sydney Basin, Australia. *International Journal of Coal Geology* **2007,** 70, 240.

20. Wang, F.; Shao, X.; Wang, W.; Xue, R.; Shen, Z., Measurements of diffusion coefficients for methane and carbon dioxide in activated meso-carbon microbeads. *Journal of Chemical Industry and Engineering (China)* **2006,** 57, 1891.

21. Do, D. D., *Adsorption analysis: equilibria and kinetics*. Imperial College Press: London, 1998.

22. Serbezov, A. S.; Sotirchos, S. V., Mathematic modelling of multicomponent nonisothermal adsorption in sorbent particles under pressure swing conditions. *Adsorption* **1998,** 4, 93.

23. MacElroy, J. M. D.; Boyle, M. J., Nonequlibrium molecular dynamics simulation of a model carbon memebrane seperation of CH4/H2 mixtures. *Chemical Engineering Journal* **1999,** 74.

24. Sokhan, V. P.; Nicholson, D.; Quirke, N., Fluid flow in nanopores: An examination of hydrodynamic boundary conditions. *J.Chem.Phys.* **2001,** 115, 3878.

25. Xu, L.; Sedigh, M. G.; Tsotsis, T. T.; Sahimi, M., Nonequilibrium molecular dynamics simulation of transport and separation of gases in carbon nanopores. II. Binary and ternary mixtures and comparison with the experimental data. *J.Chem.Phys.* **2000,** 112, 910.

26. Seo, Y. G.; Kumb, G. H.; Seaton, N. A., Monte Carlo simulation of transport diffusion in nanoporous carbon membranes. *Journal of Membrane Science* **2002,** 195, 65.

27. Huitemaa, H. E. A.; Eerden, J. P. v. d., Can Monte Carlo simulation describe dynamics? A test on Lennard-Jones systems. *Journal of Chemical Physics* **1999,** 110, 3267.

28. Skoulidas, A. I.; Sholl, D. S., Direct tests of the darken approximation for molecular diffusion in zeolites using equilibrium molecular dynamics. *J.Phys.Chem.B* **2001,** 105, 3151.

29. Skoulidas, A. I.; Sholl, D. S.; Krishna, R., Correlation effects in diffusion of CH4/CF4 mixtures in MFI zeolite. A study linking MD simulations with the Maxwell-Stefan formulation. *Langmuir* **2003,** 19, 7977.

30. Chempath, S.; Krishna, R.; Snurr, R. Q., Nonequilibrium molecular dynamics simulations of diffusion of binary mixtures containing short n-alkanes in faujasite. *J.Phys.Chem.* **2004,** 108, 13481.

31. Skoulidas, A. I.; Sholl, D. S., Molecular dynamics simulations of self-diffusivities, corrected diffusivities, and transport diffusivities of light gases in four silica zeolites to assess influence of pore shape and conectivity. *J. Phys. Chem. A* **2003,** 107, 10132.

32. Skoulidas, A. I.; Sholl, D. S., Transport diffusivities of CH4, CF4, He, Ar,Xe and SF6 in Silicalite from atomistic simulations. *J.Phys.Chem.B* **2002,** 106, 5058.

33. Maginn, E. J.; Bell, A. T.; Theodorou, D. N., Transport diffusivity of methane in silicalite from equilibrium and nonequilibrium simulations. *J. Phys.Chem* **1993,** 97, 4173.

34. Mao, Z.; Sinnott, S. B., computional study of molecular difffusion and dynamic flow through carbon nanotubes. *J. Phys. Chem. B* **2000,** 104, 4618.

35. Skoulidas, A. I.; Ackerman, D. A.; Johnson, J. K.; Sholl, D. S., Rapid transport of gases in carbon nanotubes. *Physical Review Letters* **2002,** 89, 185901-1.

36. Sokhan, V. P.; Nicholson, D.; Quirke, N., Transport properties of nitrogen in single walled carbon nanotubes. *J.Chem.Phys.* **2004,** 120, 3855.

37. Chen, H.; Sholl, D. S., Rapid diffusion of CH4/H2 mixtures in single-walled carbon nanotubes. *JACS* **2004,** 126, 7778.

38. Chen, H.; Johnson, J. K.; Sholl, D. S., Transport diffusion of gases is rapid in flexible carbon nanotubes. *J. Phys.Chem. B* **2006,** 110, 1971.

39. Skoulidas, A. I.; Sholl, D. S.; Johnson, J. K., Adsorption and diffusion of carbon dioxide and nitrogen through single-walled carbon nanotube membrane. *J. Chem. Phys.* **2006,** 124, 054708.

40. Jakobtorweihen, S.; Lowe, C. P.; Keil, F. J.; Smit, B., A novel algorithm to model the influence of host lattice flexibility in molecular dnamics simulations:Loading dependence of self-difffusion in carbon nanotubes. *J.chem.Phys.* **2006,** 124, 154706.

41. Düren, T.; Keil, F. J.; Seaton, N. A., Composition dependent transport diffusion coefficients of CH4/CF4 mixtures in carbon nanotubes by non-equilibrium molecular dynamics simulations. *Chemical Engineering Science* **2002,** 57, 1343.

42. Vieira-Linhares, A. M.; Seaton, N. A., Non-equilibrium molecular dynamics simulation of gas separation in a microporous carbon membrane. *Chemical Engineering Science* **2003,** 58, 4129.

43. Cao, D.; Zhang, X.; Chen, J.; Yun, J., Local diffusion coefficient of supercritical methane in activated carbon by molecular simulation. *Carbon* **2003,** 41, 2686.

44. Zhou, J.; Wang, W., Adsorption and diffusion of supercritical carbon dioxide in slit pores. *Langmuir* **2000,** 16, 8063.

45. Klochko, A. V.; Brodskaya, E. N.; Piotrovskaya, E. M., Computer simulations of dependence of adsorption characteristics of ethane on the size of graphite micropores. *Langmuir* **1999,** 15, 545.

46. Skoulidas, A. I.; Sholl, D. S., Self-diffusion and transport diffusion of light gases in metal-organic framework materials assessed using molecular dynamics simulations. *j. Phys.Chem. B* **2005,** 109, 15760.

47. Biggs, M. J.; Buts, A., Virtual porous carbons: what they are and what they can be used for. *Molecular Simulation* **2006,** 32, 579.

48. Feng, C.; Stewart, W. E., Practical models for isothermal diffusion and flow of gases in porous solids. *Ind. Eng. Chem. Fundam.* **1973,** 12, 143.

49. Seaton, N. A.; Walton, J. P. R. B.; Quirke, N., A new analysis method for the determination of porous carbons from nitrogen adsorption measurements. *Carbon* **1989,** 27, 853.

50. Lastoskie, C.; Gubbins, K. E.; Quirke, N., Pore size dstribution analysis of microporous carbons-A density functional theory approach. *J. Phys. Chem.* **1993,** 97, 4786.

51. Gusev, V. Y.; O'Brien, J. A.; Seaton, N. A., A self-consistent method for characterization of activated carbons using supercritical adsorption and grand canonical Monte Carlo simulations. *Langmuir* **1997,** 13, 2815.

52. Seaton, N. A., Determination of the connectivity of porous solids from nitrogen sorption measurements. *Chemical Engineering Science* **1991,** 46, 1895.

53. Liu, H.; Zhang, L.; Seaton, N. A., Determination of the connectivity of porous solids from nitrogen sorption measurements — II. Generalisation. *Chemical Engineering Science* **1992,** 47, 4393.

54. López-Ramón, M. V.; Jagiełło, J.; Bandosz, T. J.; Seaton, N. A., Determination of the pore size distribution and network connectivity in

microporous solids by adsorption measurements and Monte Carlo simulation. *Langmuir* **1997,** 13, 4435.

55. Hollewand, M. P.; Gladden, L. F., Modelling of diffusion and reaction in porous catalysts using a random three-dimensional network model. *Chemical Engineering Science* **1992,** 47, 1761.
56. Coppens, M.-O., The effect of fractal surface roughness on diffusion and reaction in porous catalysts – from fundamentals to practical applications. *Catalysis Today* **1999,** 53, 225.
57. Emmett, P. H., Adsorption and pore-size measurements on charcoals and whetlerites. *Chem. Rev.* **1948,** 43, 69.
58. Nicholson, D., Using computer simulation to study the properties of molecules in micropores. *J. Chem. Soc. Faraday Trans.* **1996,** 92, 1.
59. Sweatman, M. B.; Quirke, N., Modelling gas mixture adsorption in active carbons. *Molecular Simulation* **2005,** 31, 667.
60. Marsh, H.; Crawford, D.; O'Grady, T. M.; Wennerberg, A., Carbons of high surface area: A study by adsorption and high resolution electron microscopy. *Carbon* **1982,** 20, 419.
61. Bhatia, S. K., Density functional theory analysis of the influence of pore wall heterogeneity on adsorption in carbons. *Langmuir* **2002,** 18, 6845.
62. Chen, X. S.; McEnaney, B.; Mays, T. J.; Alcaniz-Monge, J.; Cazorla-Amoros, D.; Linares-Solano, A., Theoretical and experimental studies of methane adsorption on microporous carbons. *Carbon* **1997,** 35, 1251.
63. Kaneko, K.; Ishii, C.; Ruike, M.; Kuwabara, H., Origin of superhigh surface area and microcrystalline graphitic structures of activated carbons. *Carbon* **1992,** 30, 1075.
64. Kaneko, K.; Ishii, C.; Kanoh, H.; Hanzawa, Y.; Setoyama, N.; Suzuki, T., Characterization of porous carbons with high resolution as-analysis and low temperature magnetic susceptibility. *Adv. Colloid Interf. Sci.* **1998,** 76-77, 295.
65. Floess, J. K.; VanLishout, Y., Calculation of adsorption energies in carbon micropores. *Carbon* **1992,** 30, 967.

66. Ford, D. M.; Glandt, E. D., Molecular simulation study of the surface barrier effect: Dilute gas limit. *J. Phys. Chem.* **1995,** 99, 11543.

67. Sahimi, M.; Gavalas, G. G.; Tsotsis, T. T., Statistical and continuum models of fluid solid reactions in porous-media. *Chemical Engineering Science* **1990,** 45, 1443.

68. Lastoskie, C.; Gubbins, K. E.; Quirke, N., *Pore size distribution analysis and networking: Studies of microporous sorbents*. Elsevier: Amsterdam, 1994; Vol. 87, p 51-60.

69. Rodriguez, J.; Ruette, F.; Laine, J., Molecular modeling of micropores in activated carbon. *Carbon* **1994,** 32, 1536.

70. Shevade, A. V.; Jiang, S.; Gubbins, K. E., Molecular simulation study of watermethanol mixtures in activated carbon pores. *J. Chem. Phys.* **2000,** 113, 6933.

71. Jin, W.; Wang, W., Computer simulation of adsorption of a Stockmayer molecule chlorodifluoromethane in activated carbon slit pores. *J. Chem. Phys.* **2001,** 114, 10163.

72. Jorge, M.; Schumacher, C.; Seaton, N. A., Simulation study of the effect of the chemical heterogeneity of activated carbon on water adsorption. *Langmuir* **2002,** 18, 9296.

73. Harris, P. J. F.; Burian, A.; Duber, S., High-resolution electron microscopy of microporous carbon. *Philoscophical Magazine Letters* **2000,** 80, 381.

74. Bojan, M. J.; Steele, W. A., Computer simulation in pores with rectangular cross-sections. *Carbon* **1998,** 36, 1417.

75. Davies, G. M.; Seaton, N. A., The effect of the choice of pore model on the characterization of the internal structure of microporous carbons using pore size ditributions. *Carbon* **1998,** 36, 1473.

76. Seaton, N. A.; Friedman, S. P.; MacElroy, J. M. D.; Murphy, B. J., The molecular sieving mechanism in carbon molecular sievies: A molecular dynamics and critical path analysis. *Langmuir* **1997,** 13, 1199.

77. Turner, A. R.; Quirke, N., A grand canonical Monte Carlo study of adsorption on graphitic surfaces with defects. *Carbon* **1998,** 36, 1439.

78. Lin, C.; Cohen, M. H., Quantitative methods for geometric modeling. *Journal of Applied Physics* **1982,** 53, 4152.

79. Jerauld, G. R.; Scriven, L. E.; Davis, H. T., percolation and conductance on the 3D Voronoi and regular networks: a second case study in topological disorder. *J. Phys. C* **1984,** 17, 3429.

80. Sahimi, M., Diffusion-controlled reactions in disorderd porous media-I. Uniform distribution of reactants. *Chemical Engineering Science* **1988,** 43, 2981.

81. Arbabi, S.; Sahimi, M., Computer simulations of catalyst deactivation - I. Model formulation and validation. *Chemical Engineering Science* **1991,** 46, 1739.

82. Biggs, M.; Agarwal, P., Mass diffusion of atomic fluids in random micropore spaces using equilibrium molecular dynamics. *Phys. Rev. A* **1992,** 46, 3312.

83. Oberlin, A., High resolution TEM studies of carbonization and graphitization. *Chem. Phys. Carbon* **1989,** 22, 1.

84. Segarra, E. I.; Glandt, E. D., Model microporous carbons: microstructure, surface polarity and gas adsorption. *Chemical Engineering Science* **1994,** 49, 2953.

85. Acharya, M.; Trand, M. S.; Mathews, J. P.; Billinge, S. J. L.; Petkov, V.; Subramoney, S.; Foley, H. C., Simulation of nanoporous carbons: A chemically constrained structure. *Philoscophical Magazine B* **1999,** 79, 1499.

86. Thomson, K. T.; Gubbins, K. E., Modeling structural morphology of microporous carbons by reverse monte carlo. *Langmuir* **2000,** 16, 5761.

87. Brennan, J. K.; Thomson, K. T.; Gubbins, K. E., Adsorption of water in activated carbons: Effects of pore blocking and connectivity. *Langmuir* **2002,** 18, 5438.

88. Pikunic, J.; Clinard, C.; Cohaut, N.; Gubbins, K. E.; J.-M.Guet; Pellenq, R. J.-M.; Rannou, I.; Rouzaud, J.-N., Structural modeling of porous carbons: Constrained reverse Monte Carlo method. *Langmuir* **2003,** 19, 8565.

89. Zetterström, P.; Urbonaite, S.; Lindberg, F.; delaplane, R. G.; Leis, J.; Svensson, G., Reverse Monte Carlo studies of nanoporous carbon from TiC. *Journal of Physics: Condensed Matter* **2005,** 17, 3509.

90. Biggs, M. J.; Buts, A.; Williamson, D., Molecular simulation evidence for solidlike adsorbate in complex carbonaceous micropore structures. *Langmuir* **2004,** 20, 5786.

91. Biggs, M. J.; Buts, A.; Williamson, D., Absolute assessment of adsorption-based porous solid characterization methods: comparison methods. *Langmuir* **2004,** 20, 7123.

92. Gregg, S. J.; Sing, K. S. W., *Adsorption, surface area and porosity.* 2nd ed.; Academic Press: London, 1982.

93. Rodríguez-Reinoso, F.; Linares-Solano, A., *Micro- porous structure of activated carbons as revealed by adsorption methods.* Marcel Dekker: New York, 1988.

94. Stoeckli, H. F., A generalization of the Dubinin—Radushkevich equation for the filling of heterogeneous micropore systems. *J. Colloid Interface Science* **1977,** 59, 184.

95. Dubinin, M. M., *Progress in surface and membrane science.* Academic Press: New York, 1975; p 1-70.

96. Horváth, G.; Kawazoe, K., Method for the calculation of effective pore-size distribution in molecular-sieve carbon. *J. Chem. Eng. Japan* **1983,** 16, 470.

97. Russell, B. P.; LeVan, M. D., Pore size distribution of BPL activated carbon determined by different methods. *Carbon* **1994,** 32, 845.

98. Rychlicki, G.; Terzyk, A. P.; Lukaszewicz, J. P., Determination of carbon porosity from low-temperature nitrogen adsorption data: A comparison of the most frequently used methods. *Colloids and Surfaces A: Physicochemical and Engineering Aspects* **1995,** 96, 105.

99. Valladares, D. L.; Reinoso, F. R.; Zgrablich, G., Characterization of active carbons: the influence of the method in the determination of the pore size distribution. *Carbon* **1998,** 36, 1491.

100. Aukett, P. N.; Quirke, N.; Riddiford, S.; Tennison, S. R., Methane adsorption on microporous carbons-a comparison of experiment, theory, and simulation. *Carbon* **1992,** 30, 913.

101. Quirke, N.; Tennison, S. R. R., The interaction of pore size distributions of microporous carbons. *Carbon* **1996,** 34, 1281.

102. Gusev, V. I.; O'Brien, J. A., Can molecular simulation be used to predict adsorption on activated carbon? *Langmuir* **1997,** 13, 2822.

103. Davies, G. M.; Seaton, N. A., Development and validation of pore structure models for adsorption in activated carbons. *Langmuir* **1999,** 15, 6263.

104. Davies, G. M.; Seaton, N. A., Predicting adsorption equilibrium using molecular simulation. *AIChE Journal* **2000,** 46, 1753.

105. Ravikovitch, P. I.; Vishnyakov, A.; Russo, R.; Neimark, A. V., Unified approach to pore size characterization of microporous carbonaceous materials from N_2, Ar, and CO_2 adsorption isotherms. *Langmuir* **2000,** 16, 2311.

106. Sweatman, M. B.; Quirke, N., Characterization of porous materials by gas adsorption: comparison of nitrogen at 77 K and carbon dioxide at 298 K for activated carbon. *Langmuir* **2001,** 17, 5011.

107. Sweatman, M. B.; Quirke, N., Characterization of porous materials by gas adsorption at ambient temperatures and high pressure. *J. Phys. Chem.* **2001,** 105, 1403.

108. Jorge, M.; Seaton, N. A., Predicting adsorption of water/organic mixtures using molecular simulation. *AIChE Journal* **2003,** 49, 2059.

109. Pantatosaki, E.; Psomadopoulos, D.; Steriotis, T.; Stubos, A. K.; Papaionnou, A.; Papadopoulos, G. K., Micropore size distributions from CO2 using grand canonical Monte Carlo at ambient temperatures:cylindrical versus slit pore geometries. *Colloids and Surfaces A: Physicochemical and Engineering Aspects* **2004,** 241, 127.

110. Sweatman, M. B.; Quirke, N.; Zhu, W.; Kapteijn, F., Analysis of gas adsorption in Kureha active carbon based on the slit–pore model and Monte-Carlo simulations. *Molecular Simulation* **2006,** 32, 513.

111. Stoeckli, F.; Guillot, A.; Slasli, A. M.; Hugi-Cleary, D., The comparison of experimental and calculated pore size distributions of activated carbons. *Carbon* **2002,** 40, 383.

112. Samios, S.; Stubos, A. K.; Papadopoulos, G. K.; Kanellopoulos, N. K.; Rigas, F., The structure of adsorbed CO2 in slit like micropores at low and high temperature and the resulting micropore size distribution based on GCMC simulations. *Journal of Colloid and Interface Science* **2000,** 224, 272.

113. Ohba, T.; Omori, T.; Kanoh, H.; Kaneko, K., Cluster structures of supercritical CH4 confined in carbon nanospaces with in situ high-pressure small-angle X-ray scattering and grand canonical Monte Carlo simulation. *J. Phys. Chem. B.* **2004,** 108, 27.

114. Do, D. D.; Do, H. D., Refined method of potential enhancement in the equilibria characterization of activated carbon: Comparison with GCMC and DFT. *Langmuir* **2003,** 19, 8302.

115. López-Ramón, M. V. J. o., J.; Bandosz, T. J.; Seaton, N. A., Determination of the pore size distribution and network connectivity in microporous solids by adsorption measurements and Monte Carlo simulation. *Langmuir* **1997,** 13, 4435.

116. Lozano-Castello, D.; Cazorla-Amoros, D.; Linares-Solano, A.; Oshida, K.; Miyazaki, T.; Kim, Y. J.; Hayashi, T.; Endo, M., Comparative characterization study of microporous carbons by HRTEM image analysis and gas adsorption. *J. Phys. Chem. B* **2005,** 109, 15032.

117. Scaife, S.; Kluson, P.; Quirke, N., Characterization of porous materials by gas adsorption: do different molecular probes give different pore structures? *J. Phys. Chem. B* **2000,** 104, 313.

118. Rutherford, S. W.; Nguyen, C.; Coons, J. E.; Do, D. D., Characterization of carbon molecular sieves using methane and carbon dioxide as adsorptive probes. *Langmuir* **2003,** 19, 8335.

119. Lozano-Castelló, D.; Cazorla-Amorós, D.; Linares-Solano, A., Usefulness of CO2 adsorption at 273 K for the characterization of porous carbons. *Carbon* **2004,** 42, 1233.

120. Ismadji, S.; Bhatia, S. K., Investigation of network connectivity in activated carbons by liquid phase adsorption. *Langmuir* **2000,** 16, 9303.

121. Navarro, M. V.; Seaton, N. A.; Mastral, A. M.; Murillo, R., Analysis of the evolution of the pore size distribution and the pore network connectivity of a porous carbon during activation. *Carbon* **2006,** 44, 2281.

122. Diestler, D. J.; Schoesn, M.; Hertzner, A. W.; Cushman, J. H., Fluids in Micropores. III. Self-diffusion in a slit-pore with rough hard walls. *J.Chem.Phys.* **1991,** 95, 5432.

123. Cracknell, R. F.; Nicholson, D.; Gubbins, K. E., Molecular dynamics study of the self-diffusion of supercritical methane in slit-shaped graphitic micropores. *J.Chem.Soc.Faraday Trans.* **1995,** 91, 1377.

124. Magda, J. J.; Tirrell, M.; Davis, H. T., Molecular dynamics of narrow, liquid-filled pores. *J.Chem.Phys* **1985,** 83, 1888.

125. Schoen, M.; Cushman, J. H.; Diestler, D. J.; C. L. Rhykerd, J., Fluid in micropores. II.self-diffusion in a simple classical fluid in a slit pore. *J.Chem.Phys.* **1988,** 88, 1394.

126. Somers, S. A.; Davis, H. T., Microscopic dynamics of fluids confined between smooth and atomically structured solid surfaces. *J.Chem.Phys.* **1992,** 96, 5389.

127. Bitsanis, I.; Somers, S. A.; Davis, H. T.; Tirrell, M., Microscopic dynamics of flow in molecularly narrow pores. *J.Chem.Phys.* **1990,** 93, 3427.

128. Klochko, A. V.; Piotrovskaya, E. M.; Brodskaya, E. N., Computer simulation of the structural and kinetic characteristic of binary argon-krypton solution in graphitic pores. *Langmuir* **1996,** 12, 1578.

129. Jakobtorweihen, S.; Verbeek, M. G.; Lowe, C. P.; Keil, F. J.; Smit, B., Understanding the loading dependence of self-diffusion in carbon nanotubes. *Physical Review Letters* **2005,** 95, 044501.

130. Cracknell, R. F.; Nicholson, D.; Quirke, N., Direct molecular dynamics simulation of flow down a chemical potential gradient in a slit-shaped micropore. *Physical Review Letters* **1995,** 74, 2463.

131. Xu, L.; Tsotsis, T. T.; Sahimi, M., Nonequilibrium molecular dynamics simulation of transport and separation of gases in carbon nanopores. I.Basic results. *J.Chem.Phys.* **1999,** 111, 3252.

132. Furukawa, S.; Nitta, T., Non-equilibrium molecular dynamics simulation studies on gas permeation across carbon memebranes with different pore shape composed of micro-graphite crystallites. *Journal of Membrane Science* **2000,** 178, 107.

133. Arya, G.; Chang, H.-C.; Maginn, E. J., Knudsen diffusivity of a hard sphere in a rough slit pore. *Physical Review Letters* **2003,** 91, 026102-1.

134. Sahimi, M.; Hughes, B. D.; Scriven, L. E.; Davis, H. T., Real-space renormalization and effective-medium approximation to the percolation conduction problem. *Physical Review B* **1983,** 28, 307.

135. Sahimi, M., Transport of macromolecules in porous media. *J. Chem. Phys.* **1992,** 96, 4718.

136. Sahimi, M.; Stauffer, D., Effective simulation of flow and transport in porous media. *Chemical Engineering Science* **1991,** 46, 2225.

137. Burganos, V. N.; Sotirchos, S. V., Diffusion in pore networks: effective medium theory and smooth field approximation. *AIChE Journal* **1987,** 33, 1679-1689.

138. Burganos, V. N.; Sotirchos, S. V., Effective diffusivities in cylindrical capplilary-sphereical-cavity pore structures. *Chemical Engineering Science* **1989,** 44, 2629.

139. Zhang, L.; Seaton, N. A., Prediction of the effective diffusivity in pore networks close to a percolation threshold. *AIChE Journal* **1992,** 38, 1816.

140. Zhang, L.; Seaton, N. A., The application of continuum equations to diffusion and reaction in pore networks. *Chemical Engineering Science* **1994,** 49, 41.

141. MacElroy, J. M. D.; Friedman, S. P.; Seaton, N. A., On the origin of transport resistance within carbon molecular sievies. *Chemical Engineering Science* **1999,** 54, 1015.

142. Vieira-Linhares, A. M.; Seaton, N. A., Pore network connectivity effects on gas separation in a microporous carbon membrane. *Chemical Engineering Science* **2003,** 58, 5251.

143. Kirkpatrick, S., Percolation and conduction. *Reviews of Modern Physics* **1973,** 45, 574.

144. Stauffer, D.; Zabolitzky, J. G., Re-examination of 3D percolation threshold estimates. *J. Phys. A: Mathematical and General* **1986,** 19, 3705.

145. Ambegaokar, V.; Halperin, B. I.; Langer, J. S., Hopping conductivity in disordered systems. *Phys. Rev. B* **1971,** 4, 2612.

146. McQuarrie, D. A., *Statistical mechanics*. Harper and Row: New York, 1976.

147. Hill, T. L., *Statistical mechanics: principles and selected applications*. Dover Publications: New York, 1987.

148. Metropolis, N.; Rosenbluth, A. W.; Rosenbluth, M. N.; Teller, A. H.; Teller, E., Equations of state calculations by fast computing machines. *Journal of Chemical Physics* **1953,** 21, 1087.

149. Frenkel, D.; Smit, B., *Understanding molecular simulation: from algorithm to applications*. Academic Press: London, 1996.

150. Nicholson, D.; Parsonage, N. G., *Computer simulation and the statistical mechanics of adsorption*. Academic Press: London, 1982.

151. Allen, M. P.; Tildesley, D. J., *Computer simulation of liquids*. Oxford Science Publications: Oxford, 1987.

152. Sandler, S. I., *Chemical and engineering thermodynamics*. John Wiley & Sons: New York, 1999.

153. Jagiełło, J.; Bandosz, T. J.; Putyera, K.; Schwarz, J. A., Adsorption near ambient temperatures of methane, carbon tetrafluoride, and sulfur hexafluoride on commercial activated carbons. *J. Chem. Eng. Data* **1995,** 40, 1288.

154. Steele, W. A., *The interaction of gases with solid surfaces*. Pergamon: Oxford, 1974.

155. Jorge, M. A. S. Molecular simulation of the adsorption of water/organic mixtures on activated carbon. University of Edinburgh, Edinburgh, 2003.

156. Bandosz, T. J.; Biggs, M. J.; Gubbins, K. E.; Hattori, Y.; Iiyama, T.; Kaneko, K.; Pikunic, J.; Thomson, K. T., Models of porous carbons. *Chemistry and Physics of Carbon* **2003,** 28, 41.

157. Personal communication with Dr. Alex Buts. In Edinburgh.

158. Thovert, J. F.; Salles, J.; Adler, P. M., Computerized characterization of the geometry of real porous media - their discritization, analysis and interpretation. *Journal of Microscopy-Oxford* **1993,** 170, 65.

159. Hoshen, J.; Kopelman, R., Percolation and cluster distribution.1. Cluster multiple labeling technique and critical concentration algorithm. *Physical Review B* **1976,** 14, 3438.

160. Stauffer, D., *Introduction to percolation theory*. Taylor & Francis Ltd: London, 1985.

161. Sahimi, M., *Applications of percolation theory*. Taylor & Francis Ltd: London, 1994.

162. Zhang, L. S., N. A., Simulation of catalyst fouling at the particle and reactor levels. *Chemical Engineering Science* **1996,** 51, 3257.

163. Celzard, A.; Fierro, V., Preparing a suitable material designed for methane storage: A comprehensive report. *Energy & Fuels* **2005,** 19, 573.

164. Haile, J. M., *Molecular dynamics simulation: elementary methods*. John Wiley & Sons: USA, 1992.

165. Swope, W. C.; Anderson, H. C.; Berens, P. H.; Wilson, K. R., A computer simulation method for the calculation of equilibrium constants for the formation of physical clusters of molecules: application to small water clusters. *J. Chem. Phys.* **1982,** 76, 637.

166. Nosé, S., Constant temperature molecular dynamics methods. *Progress of Theoretical Physics Supplement* **1991,** 103, 1.

167. Evans, D. J.; Hoover, W. G.; Failor, B. H.; Moran, B.; Ladd, A. J. C., Nonequilibrium molecular dynamics via Gauss's principle of least constraint. *Phys. Rev. A* **1983,** 28, 1016.

168. Brown, D.; Clarke, J., A comparison of constant energy, constant temperature and constant pressure ensembles in molecular dynamics simulations of atomic liquids. *Molecular Physics* **1984,** 51, 1243.

169. Heffelfinger, G. S.; Swol, F. V., Diffusion in Lennard-Jones fluids using dual control volume grand canonical molecular dynamics simulation (DCV-GCMD). *J.Chem.Phys.* **1994,** 100, 7548.

170. Travis, K. P.; Gubbins, K. E., Transport diffusion of oxygen-nitrogen mixtures in graphite pores: A Nonequilibrium molecular dynamics(NEMD) study. *Langmuir* **1999,** 15, 6050.

171. Papadopoulos, G. K.; Jobic, H.; Theodorou, D. N., Transport diffusivity of N2 and CO2 in silicalite: Coherent quasielastic neutron scattering measurements and molecular dynamics simulations. *J.Phys.Chem.B* **2004,** 108, 12748.

172. Arya, G.; Chang, H.; Maginn, E. J., A critical comparison of equilibrium, non-equilibrium and boundary-driven molecular dynamics for studying

transport in microporous materials. *Journal of Chemical Physics* **2001,** 115, 8113.

173. Wheeler, D. R.; Newman, J., Molecular dynamics simulations of multicomponent diffusion. 2. Nonequilibrium method. *J. Phys.Chem. B* **2004,** 108, 18362.

174. Tang, Y. W.; Chan, K. Y.; Szalai, I., Structural and transport prooperties of an SPC/E electrolyte in a nanopore. *J. Phys.Chem. B* **2004,** 108, 18204.

175. Sanborn, M. J.; Snurr, R. Q., Diffusion of binary mixture of CF_4 and n-alkanes in faujasite. *Separation and Purification Technology* **2000,** 20, 1.

176. Rapaport, D. C., *The art of molecular dynamics simulation*. Cambridge University Press: Cambridge, 1995.

177. Reynolds, P. J.; Klein, W.; Stanley, H. E., A real space renormalization group for site and bond percolation. *J. Phys. C: Solid State Physics* **1977,** 10, L167.

178. Shah, N.; Ottino, J. M., Effective transport properties of disordered, multiphase composites: Application of real-space renormalization group theory. *Chemical Engineering Science* **1986,** 41, 283.

179. Bernasconi, J., Real-space renormalization of bond-disordered conductance lattice. *Physical Review B* **1978,** 18, 2185.

Appendix I. Calculation of the renormalized conductance

The 12 conductances in the equivalent circuit of an octahedral network, i.e. the renormalization cell, are labelled g1, g2...g12, as shown in Fig.1. The conductance of the circuit is calculated by imposing a unit potential difference across the cell between nodes A and B and writing current balance equations for the four internal nodes C, D, E and F.

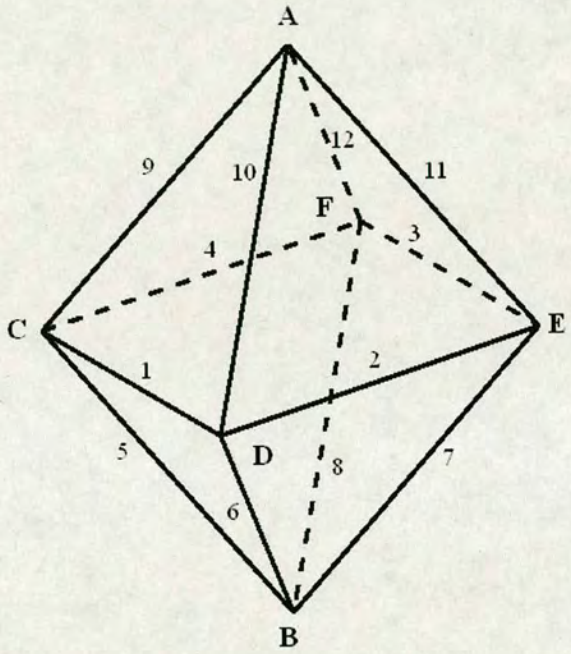

Figure 1 Labelling of bonds in the equivalent circuit of an octahedral network.

The four equations are solved for V_C, V_D, V_E and V_F giving:

$$V_c = \frac{1}{G}\{g_9\{(g_2+g_1+g_6+g_{10})[(g_3+g_2+g_7+g_{11})(g_4+g_3+g_8+g_{12})-g_3^2]$$
$$-g_2^2(g_4+g_3+g_8+g_{12})\}+g_{10}\{g_2g_3g_4+g_1(g_3+g_2+g_7+g_{11})(g_4+g_3+g_8+g_{12})$$
$$-g_1g_3^2\}+g_3g_4(g_2+g_1+g_6+g_{10})\}+g_{12}\{g_1g_2g_3$$
$$+g_4[(g_2+g_1+g_6+g_{10})(g_3+g_2+g_7+g_{11})-g_2^2]\}\}$$

$$V_D = \frac{1}{G}\{g_9\{g_2g_3g_4 + g_1[(g_3 + g_2 + g_7 + g_{11})(g_4 + g_3 + g_8 + g_{12}) - g_3^2]\}$$
$$+ g_{10}\{(g_3 + g_2 + g_7 + g_{11})[(g_1 + g_4 + g_5 + g_9)(g_4 + g_3 + g_8 + g_{12}) - g_4^2]$$
$$- g_3^2(g_1 + g_4 + g_5 + g_9)\} + g_{11}\{g_1g_3g_4 + g_2[(g_1 + g_4 + g_5 + g_9)(g_4 + g_3 + g_8 + g_{12})$$
$$- g_4^2]\} + g_{12}\{g_2g_3(g_1 + g_4 + g_5 + g_9) + g_1g_4(g_3 + g_2 + g_7 + g_{11})\}\}$$

$$V_E = \frac{1}{G}\{g_9\{g_1g_2(g_4 + g_3 + g_8 + g_{12}) + g_3g_4(g_2 + g_1 + g_6 + g_{10})\} + g_{10}\{g_1g_3g_4$$
$$+ g_2[(g_1 + g_4 + g_5 + g_9)(g_4 + g_3 + g_8 + g_{12}) - g_4^2]\} + g_{11}\{(g_4 + g_3 + g_8 + g_{12})[(g_2$$
$$+ g_1 + g_6 + g_{10})(g_1 + g_4 + g_5 + g_9) - g_1^2] - g_4^2(g_2 + g_1 + g_6 + g_{10})\} + g_{12}\{g_1g_2g_4$$
$$+ g_3[(g_2 + g_1 + g_6 + g_{10})(g_1 + g_4 + g_5 + g_9) - g_1^2]\}\}$$

and

$$V_F = \frac{1}{G}\{g_9\{g_1g_2g_3 + g_4[(g_2 + g_1 + g_6 + g_{10})(g_3 + g_2 + g_7 + g_{11}) - g_2^2]\}$$
$$+ g_{10}\{g_2g_3(g_1 + g_4 + g_5 + g_9) + g_1g_4(g_3 + g_2 + g_7 + g_{11})\} + g_{11}\{g_1g_2g_4$$
$$+ g_3[(g_2 + g_1 + g_6 + g_{10})(g_1 + g_4 + g_5 + g_9) - g_1^2]\} + g_{12}\{(g_1 + g_4 + g_5 + g_9)[(g_3$$
$$+ g_2 + g_7 + g_{11})(g_2 + g_1 + g_6 + g_{10}) - g_2^2] - g_1^2(g_3 + g_2 + g_7 + g_{11})\}\}$$

where

$$G = -2g_1g_2g_3g_4 + g_1^2[g_3^2 - (g_3 + g_2 + g_7 + g_{11})(g_4 + g_3 + g_8 + g_{12})] - (g_1 + g_4 + g_5$$
$$+ g_9)[g_3^2(g_2 + g_1 + g_6 + g_{10}) + g_2^2(g_4 + g_3 + g_8 + g_{12})] + g_4^2[g_2^2 - (g_2 + g_1 + g_6$$
$$+ g_{10})(g_3 + g_2 + g_7 + g_{11})] + (g_1 + g_4 + g_5 + g_9)(g_2 + g_1 + g_6 + g_{10})(g_3 + g_2 + g_7$$
$$+ g_{11})(g_4 + g_3 + g_8 + g_{12})$$

The conductance g' of the renormalization cell is given by:

$$g' = g_5V_C + g_6V_D + g_7V_E + g_8V_F$$

Appendix II. Nomenclature

a ..... Acceleration.

A ..... Accessibility.

b ..... Pore breadth.

c ..... Concentration.

d ..... Dimensionality of the system.

D_s ..... Self-diffusion coefficient.

D_t ..... Transport diffusion coefficient.

D_c ..... Corrected diffusivity.

D_e ..... Effective diffusivity.

E ..... Total energy.

f ..... Fugacity.

f^0 ..... Fugacity at the standard state.

$f(w)$ ..... Pore size distribution in terms of pore volume.

F ..... Force.

F_{ex} ..... External force.

g ..... Pore conductance.

$\bar{g}$ ..... Number-average pore conductance.

g_e ..... Effective conductance of a network.

g' ..... Renormalized pore conductance.

g_e' ..... Renormalized effective conductance.

$g(w)$ ..... Conductance as a function of pore width.

$h(w)$ ..... Conductance distribution function.

H ..... Henry's constant.

J ..... Diffusive flux.

K ..... Number of pores per volume.

k_B ..... Boltzmann constant.

l_i ..... Length of pore i.

l_u ..... Uniform length of pores.

L ..... Phenomenological coefficients.

m ..... Molecular weight.

N ..... Number of molecules.

N_A ..... Avogadro number.

$n(w)$ ..... Pore size distribution in terms of number of pores.

$n_n(w)$ ..... Pore size distribution in terms of probability density of number of pores.

p ..... Bond occupation probability.

P ..... Bulk pressure.

p_c ..... Percolation threshold.

s ..... Standard deviation.

r ..... Position.

R ..... Ideal gas constant.

t ..... Time.

T ..... Temperature.

U ..... Potential energy.

v ..... Velocity.

V ..... Volume.

w ..... Pore width.

w_a ..... Accessible pore width.

w^* ..... Smallest pore in which adsorption takes place.

x, y, z ..... Cartesian co-ordinates.

Z ..... Coordination number.

$\overline{Z}$ ..... Mean coordination number.

Greek letters

β ..... Reciprocal of the absolute temperature.

ε ..... Potential well-depth in the Lennard-Jones Interaction potential.

ε_p ..... Porosity of the porous solid.

σ ..... Diameter of the interaction site in the Lennard-Jones interaction potential.

Δ ..... Spacing of the sheets of graphite used in the Steele potential.

Δt ..... Time step used in molecular dynamics simulation.

Γ ..... Darken thermodynamic factor.

ρ ..... Adsorbed density.

ρ_s ..... Surface density of carbon atoms used in the Steele potential.

μ ..... Chemical potential.

μ^0 ..... Chemical potential at the standard state.

ξ ..... Mechanical constraint applied in the Gaussian thermostat.

τ ..... Time span during a molecular dynamics simulation.